SANDIA REPORT

SAND2012-7988
Unlimited Release
Printed September 2012

Developing a Multiscale Test Approach for Characterizing Polymer Composites

Timothy M. Briggs

Prepared by
Sandia National Laboratories
Albuquerque, New Mexico 87185 and Livermore, California 94550

Sandia National Laboratories is a multi-program laboratory managed and operated by Sandia Corporation, a wholly owned subsidiary of Lockheed Martin Corporation, for the U.S. Department of Energy's National Nuclear Security Administration under contract DE-AC04-94AL85000.

Approved for public release; further dissemination unlimited.

Sandia National Laboratories

Issued by Sandia National Laboratories, operated for the United States Department of Energy by Sandia Corporation.

NOTICE: This report was prepared as an account of work sponsored by an agency of the United States Government. Neither the United States Government, nor any agency thereof, nor any of their employees, nor any of their contractors, subcontractors, or their employees, make any warranty, express or implied, or assume any legal liability or responsibility for the accuracy, completeness, or usefulness of any information, apparatus, product, or process disclosed, or represent that its use would not infringe privately owned rights. Reference herein to any specific commercial product, process, or service by trade name, trademark, manufacturer, or otherwise, does not necessarily constitute or imply its endorsement, recommendation, or favoring by the United States Government, any agency thereof, or any of their contractors or subcontractors. The views and opinions expressed herein do not necessarily state or reflect those of the United States Government, any agency thereof, or any of their contractors.

Printed in the United States of America. This report has been reproduced directly from the best available copy.

Available to DOE and DOE contractors from
U.S. Department of Energy
Office of Scientific and Technical Information
P.O. Box 62
Oak Ridge, TN 37831

Telephone: (865) 576-8401
Facsimile: (865) 576-5728
E-Mail: reports@adonis.osti.gov
Online ordering: http://www.osti.gov/bridge

Available to the public from
U.S. Department of Commerce
National Technical Information Service
5285 Port Royal Rd.
Springfield, VA 22161

Telephone: (800) 553-6847
Facsimile: (703) 605-6900
E-Mail: orders@ntis.fedworld.gov
Online order: http://www.ntis.gov/help/ordermethods.asp?loc=7-4-0#online

SAND2012-7988
Unlimited Release
Printed September 2012

Developing a Multiscale Test Approach for Characterizing Polymer Composites

Timothy M. Briggs
Sandia National Laboratories
P. O. Box 969
Livermore, California 94550-MS9106

Abstract

A systematic series of experimental characterization efforts have been applied to a novel advanced fiber reinforced nanocomposite material composed of carbon fiber doped with carbon nanotubes in a thermoplastic polymer. A novel depositional process has been developed and refined in order to obtain homogeneous and isotropic dispersion of the CNTs onto the interfacial surface of interest. Fracture mechanics characterization efforts under Mode I and Mode II loading have been investigated to quantify critical strain energy release rate values and study the complex fracture processes. Finite element simulations have complimented the fracture analysis in order to elucidate mechanisms at work during the precipitation and propagation. Thermal analytical responses have been measured using differential scanning calorimetry and thermal gravimetric analysis, while temperature dependent viscoelastic properties have been characterized through variable amplitude dynamic mechanical analysis. Significant increases in the energy absorption characteristics during deformation and fracture behavior have been directly measured for this CNT enhanced material system. This CNT modified CFRP material shows extreme promise for improving interply adhesion and inhibiting delamination.

TABLE OF CONTENTS

1 Introduction 17
2 Objectives 21
3 Electrospinning Deposition 23
3.1 Introduction 23
3.2 Experimental Methods 24
3.2.1 Materials 24
3.2.2 Specimen Preparation 26
3.3 Results and Discussion 30
3.4 Conclusions 39
4 Thermal Analytic Response 41
4.1 Introduction 41
4.2 Experimental Methods 43
4.2.1 Materials 43
4.2.2 Specimen Preparation 43
4.2.3 Testing Procedure 43
4.3 Results and Discussion 45
4.3.1 Differential Scanning Calorimetry 45
4.3.2 Thermal Gravimetric Analysis 48
4.4 Conclusions 50
5 Dynamic Mechanical Analysis 53
5.1 Introduction 53
5.2 Experimental Methods 57
5.2.1 Materials 57

5.2.2 Specimen Preparation 57

5.2.3 Testing Procedure 57

5.3 Results and Discussion 59

5.4 Conclusions 63

6 Mode I Fracture Characterization 65

6.1 Introduction 65

6.2 Analytical Methods 66

6.2.1 Area Method 66

6.2.2 Compliance Method 67

6.2.3 Load Method 68

6.2.4 Displacement Method 70

6.2.5 Beam Theory Method 70

6.3 Experimental Methods 72

6.3.1 Materials 72

6.3.2 Specimen Preparation 72

6.3.3 Testing Procedure 79

6.4 Results and Discussion 81

6.4.1 Load and Displacement versus Time Response 81

6.4.2 Load versus Displacement Response 83

6.4.3 Crack Growth Behavior 85

6.4.4 Energy Absorption 88

6.4.5 Critical Mode I Strain Energy Release Rate 89

6.4.6 Fractography 95

6.5 Conclusions 97

7 Finite Element Simulations of Mode I Fracture 99

7.1 Introduction 99

7.2 Model Setup 99

7.3 Results 102

7.3.1 Stress Based Analysis 102

7.3.2 Single Plane Fracture Based Analysis 103

7.3.3 Dual Plane Fracture Based Analysis 107

7.4 Conclusions 114

8 Mode II Fracture Characterization 117

8.1 Introduction 117

8.2 Analytical Methods 118

8.3 Experimental Methods 124

8.3.1 Materials 124

8.3.2 Specimen Preparation 124

8.3.3 Testing Procedure 125

8.4 Results and Discussion 129

8.4.1 Load versus Deflection Response 129

8.4.2 Crack Growth Behavior 132

8.4.3 Energy Absorption 138

8.4.4 Critical Mode II Strain Energy Release Rate 141

8.5 Conclusions 144

9 Summary, Conclusions and Recommendations 147

9.1 Summary and Conclusions 147

9.2 Future Recommendations 148

10 References 149

11 Distribution 155

LIST OF FIGURES

Figure **Page**

Figure 1 Schematic of plain weave (left) versus 8-harness satin weave (right). 25

Figure 2 Preparation of MWCNT polymer for electrospinning. 27

Figure 3 CNC controlled composite cutting table preparing CFRP materials..... 28

Figure 4 Drum inside electrospinning chamber with prepreg carbon fiber on surface. 28

Figure 5 Schematic of electrospinning depositional set-up. 29

Figure 6 Electric potential variation with resulting fiber morphology. 31

Figure 7 Depositional area and fiber diameter as a function of capillary needle voltage for a 12 kV potential..... 33

Figure 8 Progressive zooming in on isolated electrospun fiber on CFRP substrate. 34

Figure 9 Electrospinning fibers trapping surface contaminates..... 35

Figure 10 SEM images showing the as-received CFRP composite before (top) and after (bottom) electrospinning for the +6 kV and -6 kV case. 36

Figure 11 Topological profile based on vertical scanning interferometry..... 37

Figure 12 TEM images of single PVDF fibers showing the CNTs within. 38

Figure 13 Additional TEM images showing CNTs within electrospun fibers (a) and b) aligned, (c) agglomeration, and (d) electrospun fiber coalescing. 39

Figure 14 Typical DSC result showing the heat flux versus temperature. 42

Figure 15 DSC with sample preparation and turret mounting. 44

Figure 16 Baseline CFRP differential scanning calorimetry exotherm response showing integration area and limits..... 45

Figure 17 CNT enhanced CFRP differential scanning calorimetry exotherm response showing integration area and limits. 46

Figure 18 Sensitivity analysis on the integrated enthalpy of reaction and peak exotherm temperature for the baseline CFRP material compared with the CNT enhanced. 47

Figure 19 Baseline CFRP thermal gravimetric analysis response. 49

Figure 20 CNT enhanced CFRP thermal gravimetric analysis response. 49

Figure 21 Mass loss resulting from TGA between 25 – 600 °C. 50

Figure 22 Schematic of the three-point flexure experiment. 54

Figure 23 Typical DMA plot Showing the Storage Modulus, Loss Modulus, and tan δ. 56

Figure 24 Three-point flexure experimental setup for DMA. 59

Figure 25 CFRP baseline DMA results for -50 to 250 °C. 59

Figure 26 Nano enhanced CFRP DMA results for -50 to 250 °C. 60

Figure 27 Nano enhanced CFRP versus baseline material comparing the measured storage elastic modulus from dynamic mechanical analysis from -50 to 250 °C. 61

Figure 28 Nano enhanced CFRP versus baseline material comparing the measured storage elastic modulus from dynamic mechanical analysis from -50 to 250 °C. 62

Figure 29 Nano enhanced CFRP versus baseline material comparing the measured *Tan (δ)* from dynamic mechanical analysis from -50 to 250 °C. 62

Figure 30 Typical load-displacement response for a DCB experiment. 67

Figure 31 Schematic of the DCB experiment. 68

Figure 32 Asymmetric double cantilever beam (ADCB) schematic. 69

Figure 33 CNC cutting CFRP plies for composite panel lay-up and autoclave curing. 72

Figure 34 Schematic of electrospinning onto a CFRP ply. 73

Figure 35 Schematic of the laminate layed up for DCB specimen consolidation. 73

Figure 36 A thin Teflon insert applied to the end of the electrospun lamina. 74

Figure 37 Layed up composite panel under vacuum bag debulking before cure. 75

Figure 38 Autoclave with CFRP panel to cure on caul plate inside vacuum bag. 75

Figure 39 Autoclave cure schedule depicting time, temperature, and pressure relationships for complete consolidation. 76

Figure 40 Rheology curve for the 3362 resin system utilized with the carbon fiber. 77

Figure 41 Wet diamond saw cutting specimens from consolidated panels. 78

Figure 42 Bonding hinges to specimens and aligning loading fixture for attaching the hinged specimen to the load frame 79

Figure 43 DCB specimen fixturing, aligning, and testing. 80

Figure 44 Test setup for double cantilever beam Mode I fracture experiments. 80

Figure 45 Travelling microscope for in-situ crack growth determination. 81

Figure 46 Load and displacement versus time response for the baseline CFRP. 82

Figure 47 Load and displacement versus time response for the CNT enhanced CFRP. 82

Figure 48 Baseline CFRP load versus crack tip opening displacement. 83

Figure 49 CNT enhanced CFRP load versus crack tip opening displacement. 84

Figure 50 Comparison of load versus crack tip opening displacement response between baseline CFRP and CNT modified CFRP. 85

Figure 51 Mode I fracture behavior for baseline CFRP. 86

Figure 52 Mode I fracture behavior for CNT enhanced CFRP. 87

Figure 53 Illustration of total energy absorbed during fracture process. 88

Figure 54 Cumulative energy absorption for the baseline and CNT enhanced CFRP. 89

Figure 55 Typical compliance response with polynomial approximation curve fit. 90

Figure 56 Resulting critical strain energy release rate versus the crack length using all of the various methodologies developed. 91

Figure 57 Resulting critical strain energy release rate versus the COTD using all of the various methodologies developed. 91

Figure 58 Relationship between the crack length and the associated COTD. 92

Figure 59 Elasticity theory approach to determining the critical strain energy release rate for the baseline CFRP material system with logarithmic approximation. 93

Figure 60 Elasticity theory approach to determining the critical strain energy release rate for the CNT enhanced CFRP material system with logarithmic approximation. 93

Figure 61 Resulting critical strain energy release rates for both the baseline CFRP and CNT enhanced CFRP material systems as a function of the COTD. 94

Figure 62 SEM fractography images showing the variation in crack behavior for CNT enhanced CFRP (above) and baseline CFRP specimens (below) under Mode I fracture. 95

Figure 63 Baseline CFRP fracture surface showing corrugated topology with resin hackle formation between fiber locations. 96

Figure 64 CNT modified CFRP fracture surface. 97

Figure 65 CNTs visible emerging from the fracture surface (image size is approximately 7 μm wide by 4 μm tall). 97

Figure 66 Unit cell for an 8-harness satin weave textile composite fabric. 101

Figure 67 Experimental procedure showing the stack sequence for the DCB. 102

Figure 68 Three-dimensional stress state for a DCB specimen with a wedge..... 103

Figure 69 Resulting stress magnitudes for a variation in G_{Ic}..... 104

Figure 70 Resulting load versus COTD responses for a variation in G_{Ic}. 105

Figure 71 Cohesive surface element fracture simulation with experimental observations during testing. 106

Figure 72 Resulting simulation plots superposed onto experimental data. 107

Figure 73 Dual crack planes visible during Mode I testing of CNT modified CFRP. 108

Figure 74 Load versus COTD response for a separation to failure variation in G_{Ic} for both the baseline CFRP and the CNT enhanced CFRP interfaces..... 109

Figure 75 Mechanisms for dual-crack formation in CNT modified CFRP (main crack along CNT modified interface, secondary crack along baseline CFRP interface). 111

Figure 76 Load versus COTD response for a separation to failure variation in G_{Ic} for only the baseline CFRP material system interface..... 112

Figure 77 Load versus COTD response for a G_{Ic} variation for only the CNT enhanced CFRP interface..... 113

Figure 78 Experimental load versus COTD response along with the FEA simulation. 114

Figure 79 ENF schematic showing relation between geometry and crack length. 118

Figure 80 Schematic of approximate ENF specimen geometry. 125

Figure 81 Schematic of 3-point end notched flexure experiment and specimen details. 126

Figure 82 Three-point end notched flexure experiment in-progress. 127

Figure 83 Experimental setup for three-point end notched flexure experiments..... 128

Figure 84 Ultrasonic immersion tank for detecting subsurface fracture growth. 129

Figure 85 Applied flexural load versus central span deflection for the baseline CFRP and CNT enhanced CFRP for ENF experiments before elastic unloading. 130

Figure 86 Resulting stiffness versus central span deflection for the baseline CFRP and CNT enhanced CFRP for ENF experiments up through peak load. 131

Figure 87 Comparison of analytic prediction with experimental data. 132

Figure 88 End notched flexure experiments in-progress showing relative sliding along beam‘s neutral axis. 133

Figure 89 Teflon starter crack (left) shown for select specimens along with crack front growth and arrest behavior (right) for 2.7 mm thick specimen. 134

Figure 90 Micrograph showing details of crack growth behavior and arrest location for 2.7 mm thick specimen. 135

Figure 91 Resulting C-scan images based on gate location using first echo response from 10 MHz fixed focus transducer. 136

Figure 92 C-scan image of all ENF specimens after testing showing the extent and shape of fractured surface. 137

Figure 93 Three-dimensional image showing the amplitude of 10 MHz fixed focus transducer response gated on the mid-thickness interface. 137

Figure 94 Comparison between visual edge measured crack lengths and ultrasonic C-scan measured crack lengths. 138

Figure 95 Applied flexural load versus central span deflection for the baseline CFRP and CNT enhanced CFRP for ENF experiments including the elastic unloading. 139

Figure 96 Integrated area representing energy absorbed to create new fracture surface for baseline CFRP (above) and CNT enhanced CFRP specimen (below). 140

Figure 97 Cumulative energy absorbed versus central span deflection for the baseline CFRP and CNT enhanced CFRP for ENF experiments including the elastic unloading. 141

Figure 98 Resulting Mode II strain energy release rates as a function of crack length measuring method. 142

Figure 99 Mode II strain energy release rate experimental values for baseline CFRP material compared with analytic predictions using Equation (67). 143

Figure 100 Mode II strain energy release rate experimental values for CNT enhanced CFRP material compared with analytic predictions using Equation (67). 144

LIST OF TABLES

Table **Page**

Table 1 Carbon fiber reinforced polymer (CFRP) material systems used. 26

Table 2 DSC results comparing CNT modified CFRP with baseline material formulations for 2.78 °C/min heating rate. 48

Table 3 DMA experimental specifications for CFRP material. 57

Table 4 DMA testing specifications for baseline CFRP and CNT enhanced CFRP. 58

Table 5 DMA specimen specifications for CFRP and CNT enhanced CFRP. 58

Table 6 Mode I DCB specimen configuration. 74

Table 7 Input properties for separation to failure sensitivity analysis in Figure 74 110

Table 8 Input properties for separation to failure sensitivity analysis in Figure 76. 112

Table 9 Input properties for GIc sensitivity analysis in Figure 77. 113

Table 10 End notched flexure specimen geometry and stack sequence. 125

This page left intentionally blank.

1 INTRODUCTION

Advanced fiber reinforced nanocomposites (FRNs) are being considered for Sandia applications due to their potential to enhance mechanical performance and reliability. However, as a result of the multiple constituents comprising FRNs, load distribution, deformation and subsequent failure mechanisms are unknown. The alignment, adhesion, functionalization, spatial distribution and aspect ratio of the nano reinforcement fibers are all coupled in an unknown, multifaceted manner, yet are vital for structural composite applications [1]. These material aspects all affect the material‘s ability to carry external loads and dissipate energy through deformation and fracture processes, and introduce a new set of scientific challenges to understand FRN behavior. In order to confidently employ FRN‘s, the strong dependency of material behavior with the complex collection of material parameters must be rigorously investigated.

The mechanical efficiency and reliability of advanced FRNs lies in their ability to effectively transfer load from the binding matrix to the load bearing fibers, and then through each respective lamina in the laminate stack sequence. Resistance to fracture is governed by the fracture toughness of the resin and the interfacial properties between the fiber and matrix material [2]. The formation of interlaminar delamination from Mode I and Mode II fracture can severely degrade the stiffness and strength of an advanced composite material system [3], especially when subsequently under compressive loading. Disbonding and delamination can result in unsatisfactory performance or catastrophic failure of critical components if left undetected. Through-the-thickness interlacing with nano reinforcements can complicate the stress field and make it difficult to design composites with confidence [3]. As a result, the need for material characterization and understanding is paramount in these emerging processing methods and for developing material model inputs for advanced finite element simulations. While the detection of subsurface damage is virtually impossible for in-service components without extensive non destructive inspection (NDI), the critical interfaces of the composite laminate must be confidently designed to resist and tolerate conditions that are likely to induce delamination.

Electrospinning processes are currently under investigation at Sandia as a more efficient and large scale depositional method for exploiting the inherent electrical conductivity of carbon

nano tubes. The electrospinning process induces extremely high longitudinal strain rates from the jet, which can cause alignment of the nano fibers [4]. Utilizing this method of deposition is practical for understanding the mechanical implications on new, cutting-edge material systems due to the simplicity, versatility, and mass scale nature of the process [5] to produce uniform diameter fibers in a random configuration. Electrospun fibers have a random orientation when using an automated motion platform onto the composite interface surfaces of interest with a rotating drum. This can help to circumvent the issues shown to be associated with non-homogeneous nano reinforcement distribution [6]. Agglomeration significantly decreases the reinforcement‘s ability to bond with the matrix due to less contact area and effectively reduces the aspect ratio of the reinforcement [4]. In-situ observations from mechanical loading have shown that cracks in the binding matrix tend to nucleate at regions of low reinforcement density and then propagate along weak interfaces or relatively low reinforcement density regions [6]. Scanning electron microscopy (SEM) has been successfully used to establish the interaction between the propagating interlaminar crack and the nano-scale reinforcement that it encounters [7].

It is likely that there is an optimal level of nanofiber doping that must be achieved in order to maximize the mechanical benefits from a FRN material. If the system is not doped enough, it is thought that discernable signs of improved performance will not be observed, and they may actually be worse. Too low of reinforcement amounts at the interface do not provide proper mechanical interaction, yet can serve as localized stress raisers as a result of the geometric discontinuity they present [8]. If the system is doped too much, it will likely show reduced signs of performance due to the retarding effect in chemical cross linking [2], resin starvation [5] at the interfaces acting as microcracks [3], and the probabilistic nature of fracture from an increased number of defects due to the larger amount of material. A compressive, radial pre-stress is developed between the nano reinforcement and the surrounding matrix as a result of the mismatch in the coefficient of thermal expansion [7]. This gives rise to a frictional shear stress as relative deformation between the two constituents occurs. In addition, there is an increase in the micromechanical interlocking and non-bond interactions as a result of the closer contact [8]. An optimal amount of nano reinforcement could increase the fracture toughness [9] of a composite joint interface significantly, especially in Mode II, including a physical change in the deformation [10] and

fracture mechanisms [8]. Leveraging this characterization knowledge is necessary for intelligent material design and strengthening at locations and interfaces of interest, and is also needed to provide the validating data needed for advanced finite element simulations of complex geometry with FRNs.

This page left intentionally blank.

2 OBJECTIVES

To address these issues, an experimental program has been completed to obtain a fundamental understanding of advanced FRN‘s, which were expected to demonstrate new response behavior for design. Mechanistic understanding was needed to enable engineering and design of nanocomposites that are more failure resistant and predictable. The characterization techniques employed on the nanocomposite will help to understand and define how the nano reinforcement can best be utilized at the critical interfaces in the composite laminate to provide the desired mechanical response and reliability. To accomplish this, a three-phase approach was employed.

Phase I focuses on the investigation of the electrospinning deposition methodology. This effort studies the governing material and process parameters involved to effectively electrospin onto the CFRP surface of interest. The depositional morphology and topology is evaluated and correlated with the manufacturing process. This allows for the optimization of the method in order to get a homogeneous and isotropic deposition.

Phase II involves the material characterization of the FRNs, with baseline materials tested in parallel as a control case. The characterization effort focuses on the material‘s ability to deform and fracture under Mode I and Mode II loading conditions. The prime focus is on the material‘s ability to dissipate mechanical energy through complex processes of damage. A thermal analytic and dynamic mechanical analysis is also performed.

Phase III investigates the fracture morphology and mechanical performance for each material system. The resulting performance is then correlated with the observed fracture surfaces and mechanisms of energy absorption. This phase also explores finite element simulations of the Mode I fracture process involving cohesive zone modeling in order to understand the inputs necessary to predict the new response mechanisms observed.

The results of this investigation will establish the critical relationships that allow enhancement of preimpregnated polymer composites with nano reinforcement that currently do not exist. This insight and methodology can then be leveraged for this material system and others into the future. The design of structural composite materials, or multifunctional

materials in general, requires the optimized use of the constituents to obtain the desired response behavior. This behavior should be both tailorable and predictable as we increase our understanding of these nanocomposite materials through experimental characterization and numerical simulations. This effort will lead to improvements in existing composite structures and the creation of new materials for a variety of applications in the national interest.

3 ELECTROSPINNING DEPOSITION

3.1 Introduction

The electrospinning process has been well known and utilized for a number of years with a variety of applications [11]-[13]. It is a relatively straightforward process and can be tailored to produce both fibers and droplets depending on the process parameters and needs of the end use application. The attractiveness of long, thin fibers with random or controlled distribution has promise for applications such as filter development [14]-[17] and biomedical scaffolds to promote tissue growth [18]-[19]. Incorporating CNTs into a material adds an additional realm of possibilities from a structural perspective, including the enhancement of stiffness and strength of fiber reinforced composite materials [20]-[25].

For many applications, it may be desirable to have aligned nanotubes that are grown on a surface, possibly using thermal chemical vapor deposition [26]-[27], or electric field alignment [28]-[30] to induce anisotropy with preference in one direction. These instances may not require a polymer and solvent mixture as a transport medium but still require special fixturing and methodic application to obtain the desired deposition. For many applications, however, quasi-isotropy in the depositional plane may offer increased benefit for generalized applications of structural health monitoring, electromagnetic shielding, thermal transport, and interfacial toughening.

Li et al [31] successfully electrospun polysulfone nanofibers onto a carbon fiber prepreg to increase fracture toughness. Their approach utilized a flattened prepreg ply with a 24 kV potential applied between the syringe and target. Garcia et al [32] grew CNT forests upon silicon substrates using thermal chemical vapor deposition. They then transplanted the vertically aligned CNTs onto a prepreg composite material via a rolled cylinder technique. Remarkably, the transplanted CNT forest was thought to maintain the vertical orientation after an autoclave cure cycle. Deitzel et al [33] successfully electrospun poly(ethelyne oxide) in a controlled fashion by completely dampening out the bending instability with the use of an electrostatic lens element and a biased, flat collector target. This method was useful to understand and control depositional coverage area. Seol et al [34] conducted an investigation

into the structure and properties of an electrospun poly(vinylidene fluoride) (PVDF) solution with variations in the amount of single walled nanotubes, and they were successful in spinning out fibers as small as 70 nm in thickness and were able to correlate the viscosity and resulting conductivity of the solution with the mass fraction of PVDF to CNT dispersant. Controlling the deposition region, the fiber diameter and morphology, and obtaining a truly homogeneous distribution is a difficult task but would have many benefits.

This present study investigates the ability to randomly distribute MWCNTs onto the surface of a structural prepreg composite material using an electrospun polymer jet as the transport medium. The composite is rotated on an electrically charged drum while the material is electrostatically poled and drawn to the drum during a rastering traverse of a charged capillary needle. The process parameters and their effect on the fiber morphology and size, orientation, and depositional coverage area will be observed and correlated.

3.2 Experimental Methods

3.2.1 Materials

The MWCNT-PVDF formulation consists of a fluorinated PVDF thermoplastic copolymer with fully suspended and dispersed MWCNTs. The poly(vinylidene fluoride-co-hexafluoropropylene) (PVDF-HFP) pellets (Density 1.78 g/mL, Melt index = 4-10, T_m = 140 °C, T_g = 35 °C, Viscosity 20,000 – 25,000 poise) is mixed at 19 % wt. with acetone and dimethylformamide (DMF) in a mass ratio of 7:3, respectively, along with 3 wt. % MWCNTs. The MWCNTs are in dry powder form with a density of 0.22 g cm^{-3} and a carbon concentration ≥ 98 %. The MWCNTs used in this study had averaged diameters[1] of 6.6 nm with a length to diameter aspect ratio of approximately 1000. Each MWCNT has approximately 3 to 6 walls comprising it. DMF is used to disperse the MWCNTs and to aid in the dissolution of the polymer. Acetone is to reduce the melt temperature and increase the evaporation of the solution.

[1] Distribution of the tube diameter is lognormal with 75 % of the tubes < 9nm and 90 % of the tubes < 12.2 nm.

The preimpregnated composite material is composed of an 8 harness satin weave carbon fiber fabric, as depicted in Figure 1. The 8-harness satin weave is a ply architecture that possesses low crimp and high drapability. This makes it useful in applications where there are geometry changes of small radius of curvatures on surfaces to be conformed to. However, the asymmetric nature of the satin weave, as opposed to the symmetric plain weave, results in bending-twisting coupling behavior when axial loads are applied. In addition, the thermal residual stresses present after the cure, resulting from mismatches in the coefficient of thermal expansions for the fibers and the resin, will result in warping of a panel if it is not carefully layed up to be symmetric overall.

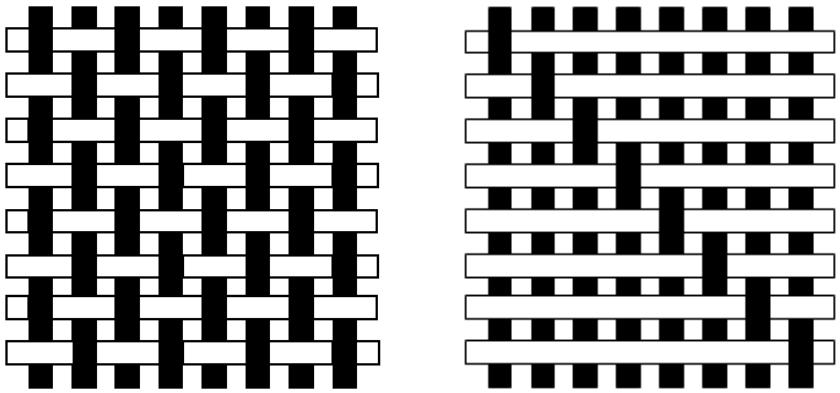

Figure 1 Schematic of plain weave (left) versus 8-harness satin weave (right).

The resin used to impregnate the carbon fiber is UF3362 (Density 1.21 g/cm^3, Tg = 161 °C, Tensile Modulus 3.17 GPa, Tensile Strength 68.95 MPa). The carbon fiber fabric is composed of HexTow AS4 C GP 3K fibers (Density 1.78 g/cm^3, Diameter 6.9 μm, Tensile Modulus 231 GPa, Tensile Strength 4385 MPa). The resin mass content for the fabric is approximately 33.6 %. Additional details of the composite material system can be seen in Table 1.

Table 1 Carbon fiber reinforced polymer (CFRP) material systems used.

Fabric Number	*SC561-8HS-3K*
Fabric Name	*TBD*
Fabric Weave Style	*8 Harness Satin*
Fabric Weight, Dry	*364g/m^2*
Fabric Thickness	*25 mil*
Consolidated Ply Thickness	*560 µm*
Fabric Weaver	*Sigmatex*
Fiber Type Warp	*HexTow AS4 C GP 3K*
Fiber Type Fill	*HexTow AS4 C GP 3K*
Warp Tow Count	*23.0 /in.*
Fill Tow Count	*23.0 /in.*
Fiber Density	*1.78 g/cm^3*
Fiber Diameter	*6.9 µm*
Fiber Tow Size	*3K*
Fiber Twist	*None*
Fiber Tow Density	*0.200 g/m*
Fiber Tow Area	*0.11 mm^2*
Fiber Tensile Strength	*4385 MPa*
Fiber Tensile Modulus	*231 GPa*
Fiber Elongation at Failure	*1.8%*
Resin Type	*UF 3362-100*
Resin Density	*1.211 g/cm^3*
Resin Shelf Life Below 75ºF	*6 Months*
Resin T_g	*161°C (322°F)*
Resin Tensile Strength	*68.95 MPa*
Resin Tensile Modulus	*3.17 GPa*
Resin Elongation at Failure	*3.5%*
Resin Moisture Absorption	*3.3%*
Resin Content (Wt. %)	*33.6*
Date of Manufacture	*18May2011*
Item I.D.	*13182*
Prepreg Lot #	*F11105-18, Roll 1*

3.2.2 Specimen Preparation

The polymer-solvent solution was mechanically mixed after pre weighing each of the constituents and adding them together. The mixing was performed using a hot plate at 60 °C using a magnetic stirrer until all of the PVDF had completely dissolved. The MWCNTs were then weighed with a precision balance and added to the premixed polymer solution. The solution was then chilled in an ice bath and tip sonicated for 10 minutes using a ¼ inch micro-tip at a power level of 14 W. The sonication step is carefully controlled to ensure that

the CNTs are not fractured during the process. The application of the ice bath facilitates the thermal management, keeping the relative temperature cool during the frictional process which occurs during sonication. This solution was then ready for electrospinning and stored in a 10 mL syringe, which threads into the electrospinner flow lines. Figure 2 depicts the main steps described in this process.

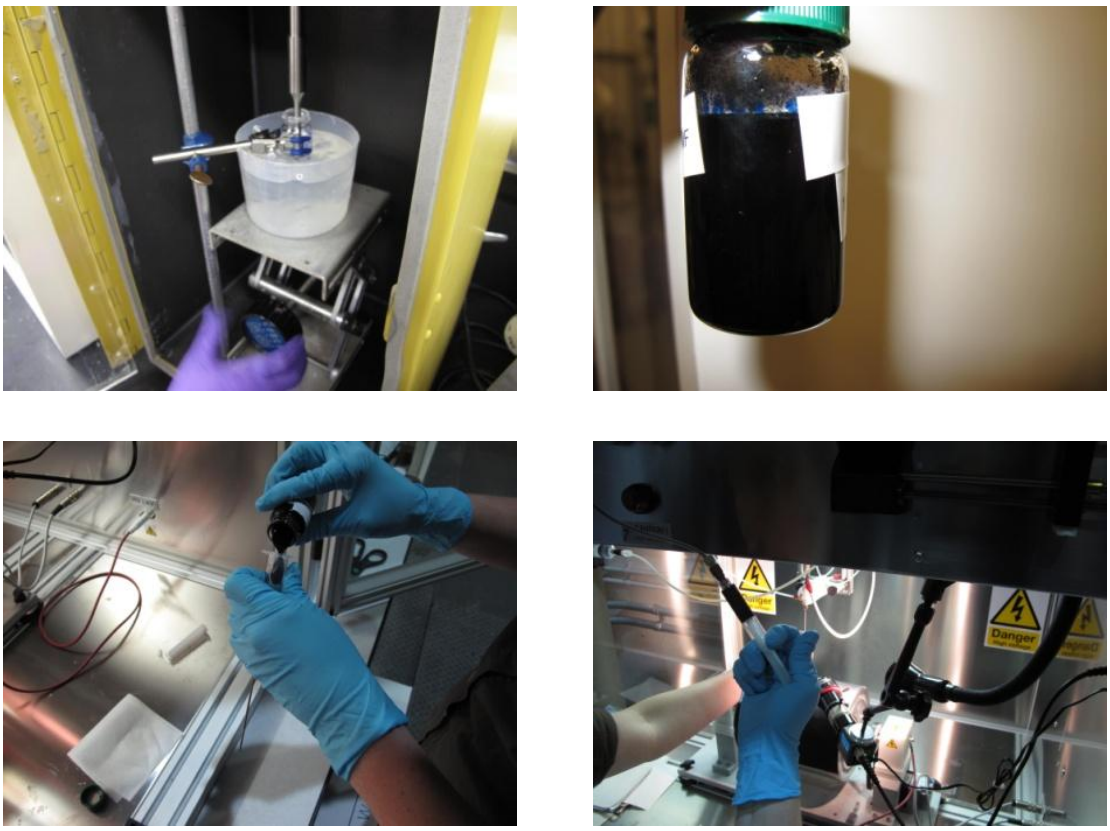

Figure 2 Preparation of MWCNT polymer for electrospinning.

The carbon fiber prepreg material was delivered in large rolls, and plies were then cut for electrospinning on to. The sections were cut using a 4-axis CNC controlled cutting table, as shown in Figure 3, equipped with a vacuum hold down table and conveyor system. The plies were cut to fit around the rotating drum in the electrospinner. This resulted in plies of 178 mm width and 622 mm long, with the width and lengths colinear with the weft and warp directions, respectively. A depiction of this is shown in Figure 4 for smaller sections of unidirectional composite material used to initially calibrate the machine. The prepreg materials are adhered to the rotating drum with double-faced tape from the back side. The

resin and fibers are facing outward for electrospinning fiber deposition directly onto that face.

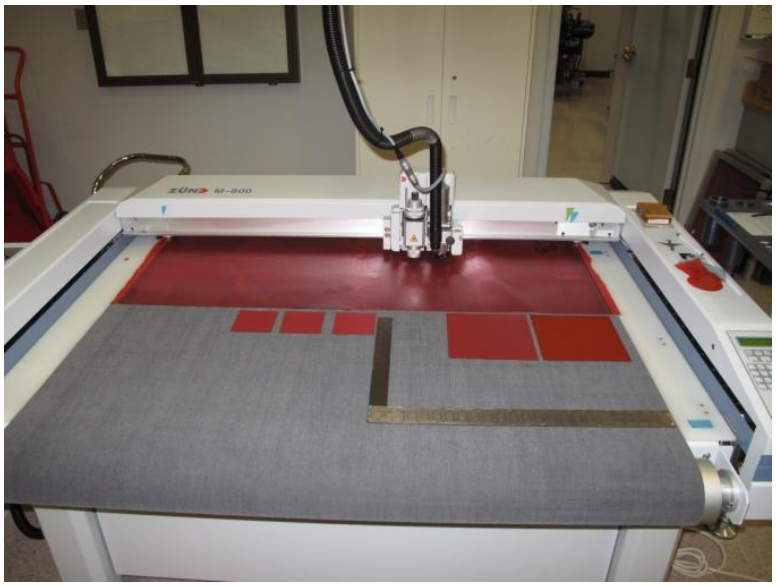

Figure 3 CNC controlled composite cutting table preparing CFRP materials.

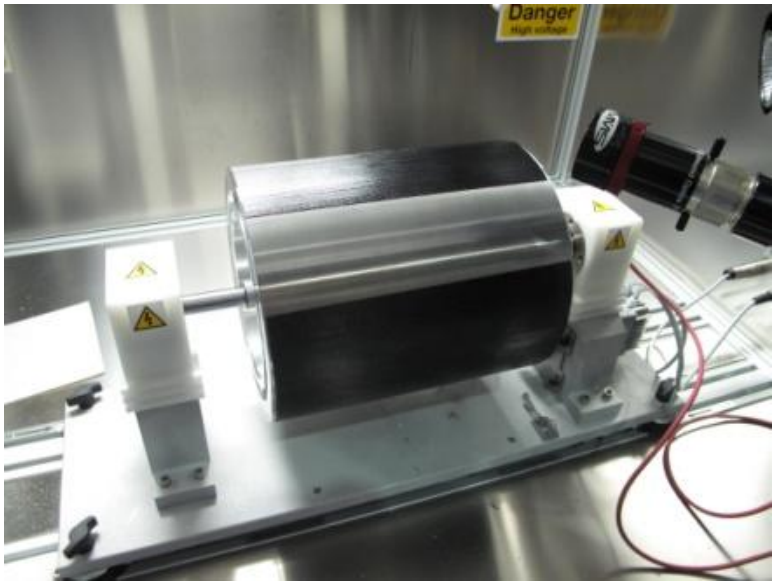

Figure 4 Drum inside electrospinning chamber with prepreg carbon fiber on surface.

The polymer solution is initially primed into the system through the syringe, as shown in Figure 2, and then the depressing of the syringe is motor controlled through the electrospinner capillary needle at a prescribed volumetric flow rate, which was held constant

at 5 mL/hr. A 100 mm standoff distance was maintained between the capillary needle and the surface of the prepreg with the capillary needle centered along the longitudinal central axis of the drum. The capillary needle was stepper motor controlled to traverse back and forth along the drums axis at a constant rate of 40 mm/s with the end limits being approximately 50 mm beyond the drum sides. This ensured complete coverage and enough length for the traverse to attain the constant velocity upon directional changes. The drum was controlled to spin at a constant rotational rate of 100 RPM. An electric potential of 12 kV was maintained between the capillary needle tip and the drum. This was found to provide sufficient Coulombic force needed to overcome the surface tension of the solution and draw the fiber out from the capillary needle without sputter or droplet formation, and is consistent with the typical condition estimate calculated by Yeo et al [35] for the balance of the capillary and Maxwell's stresses. A schematic of the experimental set-up can be seen in Figure 5.

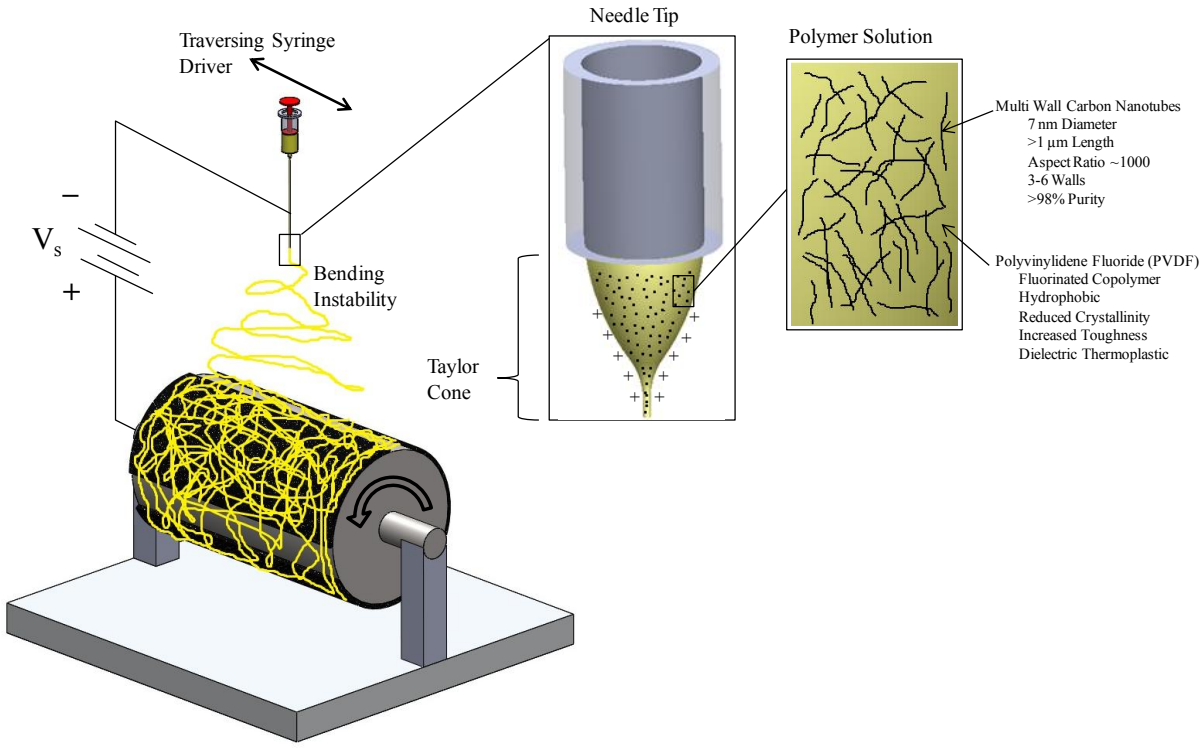

Figure 5 Schematic of electrospinning depositional set-up.

3.3 Results and Discussion

Prior to electrospinning onto the prepreg composite material, a sensitivity analysis was first performed on the voltage level held at the capillary needle and drum. This was performed to ensure that continuous fibers were spun onto the composite surface and that the fiber morphology was indicative of both random orientation without directional bias and thorough evaporation of the solvent. Also, the depositional coverage area and fiber diameter were investigated to determine if they were dependent on the respective voltages held at each location, even when the relative potential was held constant. A variation in the fiber morphology and depositional area can be seen in the scanning electron microscope (SEM) images of Figure 6 along with the respective voltage values used at the capillary needle and drum.

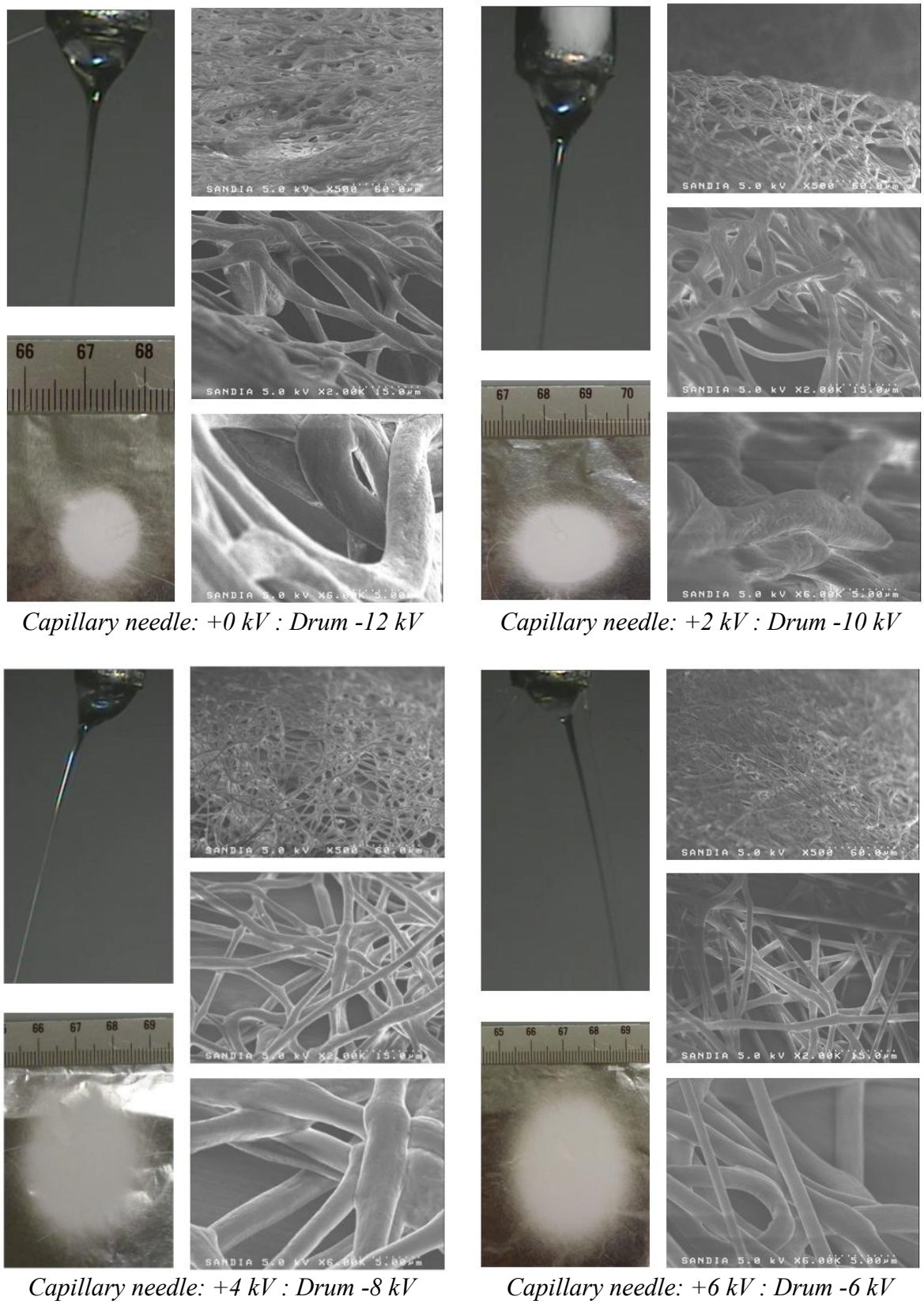

Capillary needle: +0 kV : Drum -12 kV

Capillary needle: +2 kV : Drum -10 kV

Capillary needle: +4 kV : Drum -8 kV

Capillary needle: +6 kV : Drum -6 kV

Figure 6 Electric potential variation with resulting fiber morphology.

For the initial case when the capillary needle is grounded at +0 kV and -12 kV is applied to the drum, the fiber can be seen to draw out of the capillary needle in a vertical direction, parallel to the capillary needle, and deposit over a concentrated, circular region. The fibers are very rough on the surface and have large diameters for this case. The initially vertical path for fiber deposition onto the composite substrate is a result of the electric potential at the capillary needle being in the grounded state. This implies there is no relative potential between the capillary needle and the surrounding encasement for the electrospinner. With this condition, the fiber is drawn straight down to the charged drum before it undergoes bending instability, which is likely less pronounced due to the grounded state of the capillary needle. As a result, the depositional region is compacted and tight, and the time of flight for the fibers is a shorter duration relative to the other conditions. With a short time of flight and a more direct vertical path to the charged drum, the fibers may still have solvent on them when they are deposited onto the target substrate. It is thought that the solvent eventually evaporates but leaves the fibers with a roughened surface as a result, which can be seen in both the +0 kV / -12 kV and +2 kV / -10 kV conditions shown in Figure 6. Deitzel et al. [33] explains that a reduction in fiber depositional coverage area is caused by the dampening of the bending instability. With the standoff distance held constant and the viscosity of the solution not changing, this is consistent with what was observed.

To contrast the initial cases, a condition with equal magnitude electric potentials of +6 kV and -6 kV has been applied to the capillary needle and drum, respectively. For this case, a difference in results has been attained with respect to fiber diameter, depositional area, and fiber roughness. As a result of the electric potential difference between the capillary needle and the surrounding enclosure, the fiber is drawn out of the capillary needle with an electrostatic influence from the enclosure. The initial fiber angle, shown from the onset of the Taylor Cone in Figure 6, is approximately 30 degrees from the vertical axis of the capillary needle. The fiber then undergoes a bending instability as it is drawn out and deposits onto the substrate with an area that is approximately 7 times larger than the initial case with a grounded capillary needle. It is thought that the fibers have undergone a longer time of flight given this larger depositional region, as well as the fact that the fiber diameters are reduced by an average of 63%. A plot showing the measured values of depositional region and average fiber diameter for each case can be seen in Figure 7. The reduction in fiber diameter

is likely due to the more pronounced bending instability and longer time of flight the fibers experience. A more extensive bending instability will induce higher magnitude thinning and longitudinal straining, causing the fiber to have smaller diameter. The surface roughness of the fibers can be seen to be very smooth for this +6 kV and -6 kV case since there was adequate time for evaporation of the solvent. Inspection of the various cases investigated in Figure 6 shows the smoothening of the fibers as depositional area increases and fiber diameter decreases.

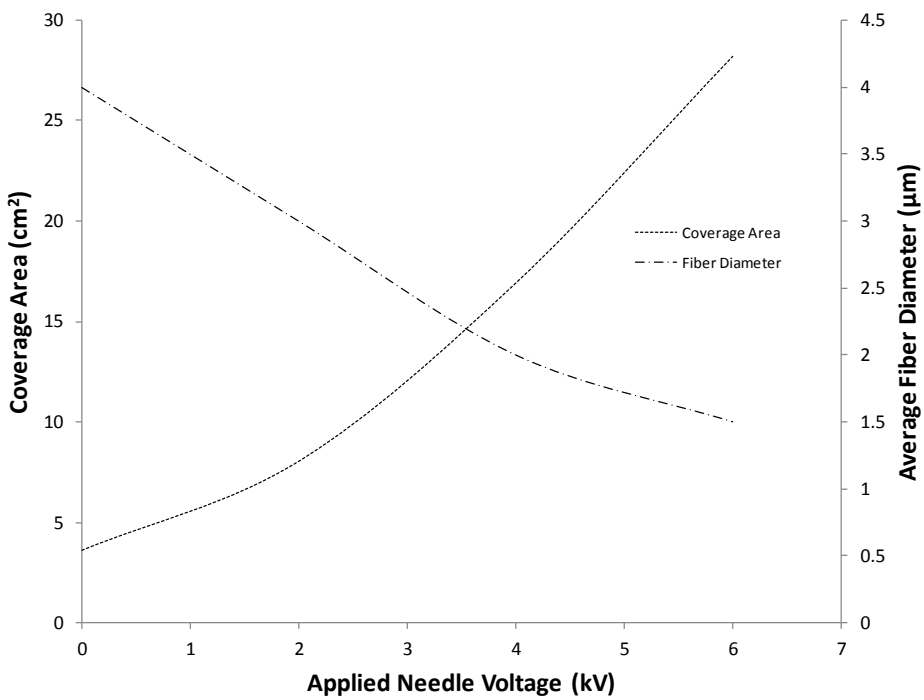

Figure 7 Depositional area and fiber diameter as a function of capillary needle voltage for a 12 kV potential.

Additional details of the fiber morphology can be seen in the SEMs of Figure 8. As a region of interest is continually zoomed in, the variation in fiber diameters amongst different fibers and smoothness of the fiber surfaces can easily be seen. In addition, the truly random fiber direction angle is also highlighted with most fibers double-backing on themselves and, in some instance, coalescing with adjoining fibers.

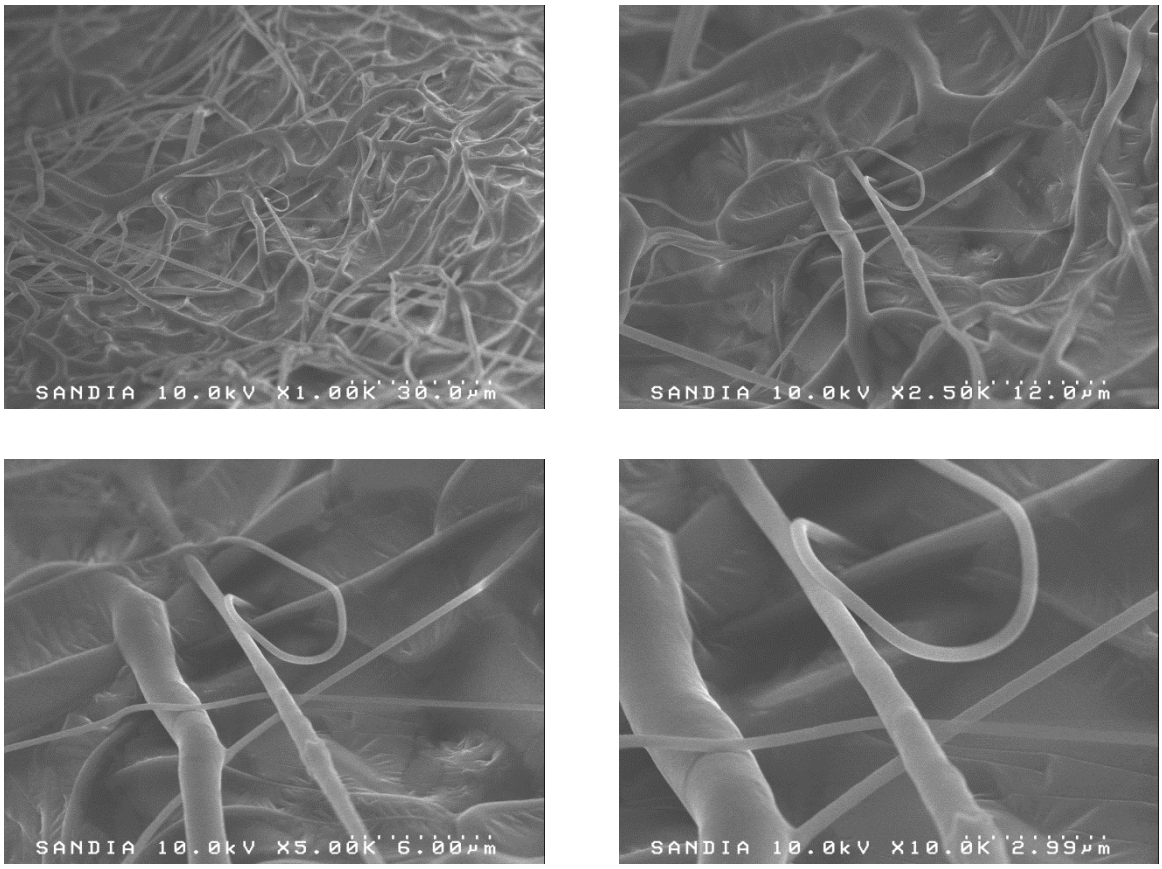

Figure 8 Progressive zooming in on isolated electrospun fiber on CFRP substrate.

It is important to ensure the surface of the material to be electrospun onto is free from contaminants. As can be seen in Figure 9, small particles of dust or powders may have been present on the surface and then trapped onto it by the electrospinning process. However, this electrospinning process could also be thought of as a method of particle entrapment for some functional application like desiccant embedding or the like.

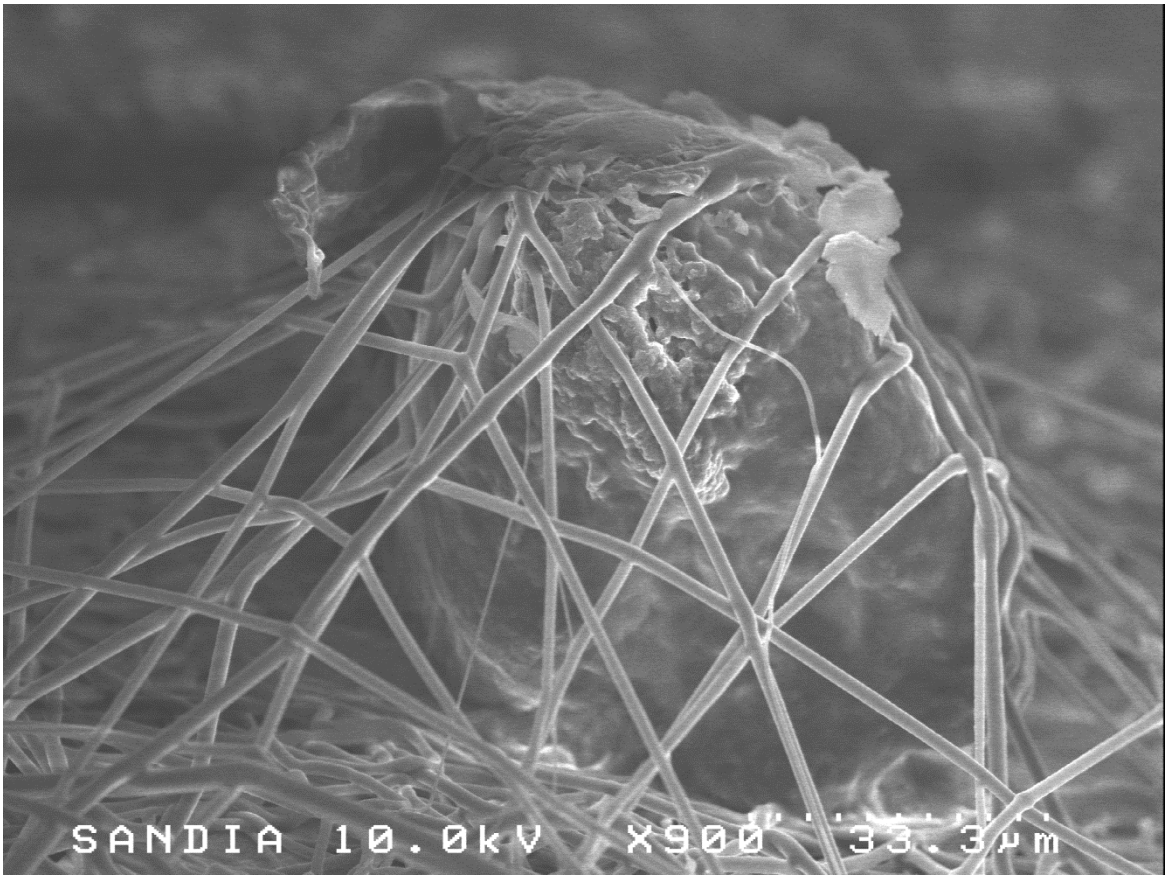

Figure 9 Electrospinning fibers trapping surface contaminates.

The as-received composite material has carbon fibers with diameters on the order of 5 μm, while the electrospun PVDF fibers have been observed on the surface to have diameters in the range of 300 nm up to 4 μm for the given parameters utilized in this study. This variation in electrospun PVDF fiber diameter spans an order of magnitude and was observed for each of the electrical potential cases considered. Representative SEM images with gold sputter coating can be seen in Figure 10 for the before and after electrospinning conditions with the +6 kV and -6 kV case. The homogeneity of the PVDF electrospun fibers and directional independence of their distribution can clearly be seen. There does not appear to be any directional dependence, particularly with consideration to the drum rotation. The bending instability coupled with the capillary needle traversing and the relatively slow drum rotation all work together to accomplish this uniform distribution. The fiber diameter and thickness of the fiber mat can be tailored through the variation of the electric field strength, polymer solution concentration, and duration of electrospinning [36]. For this study, the field strength

and polymer composition was held constant after multiple iterations to get adequate values established.

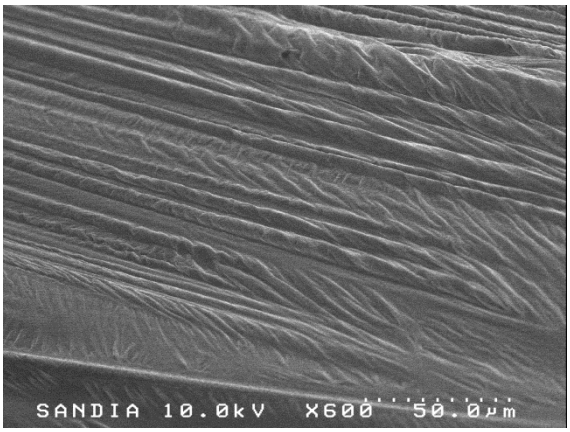

CFRP Composite Substrate Top

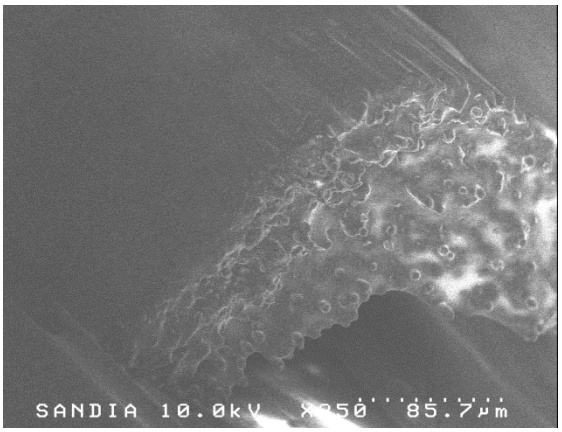

CFRP Composite Substrate Edge

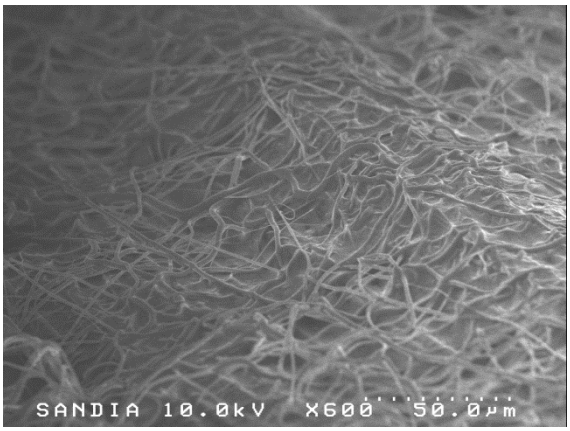

Nano-Composite Electrospun Surface Top

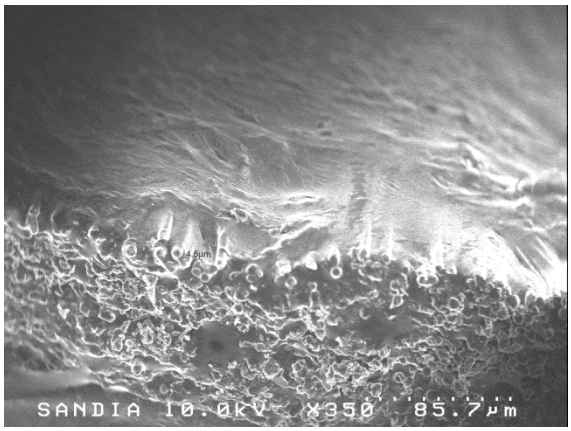

Nano-Composite Electrospun Surface Edge

Figure 10 SEM images showing the as-received CFRP composite before (top) and after (bottom) electrospinning for the +6 kV and -6 kV case.

To visualize the surface topology resulting from the electrospinning, vertical scanning interferometry measurements were conducted on the baseline, as-received CFRP composite material as well as the electrospun, nano-enhanced system. The analysis plots accompanying the scan images in Figure 11 are restricted to the vertical direction, which is colinear with the underlying carbon fibers for that region. Each separate curve on the profile height, z, represents a different analysis trace spanning the entire length of the consideration region, L, which was 450 µm. The interferometry analysis shows that the addition of the electrospun fibers increases both the average surface roughness, R_a, and root mean squared roughness, R_q, by approximately 6 times in all directions, with both roughness parameters defined in

Equation 1 and Equation 2. From the edge on image shown in Figure 10 as well as the trace analysis using the optical profilometer, the depositional layer thickness is estimated to be approximately 20 μm.

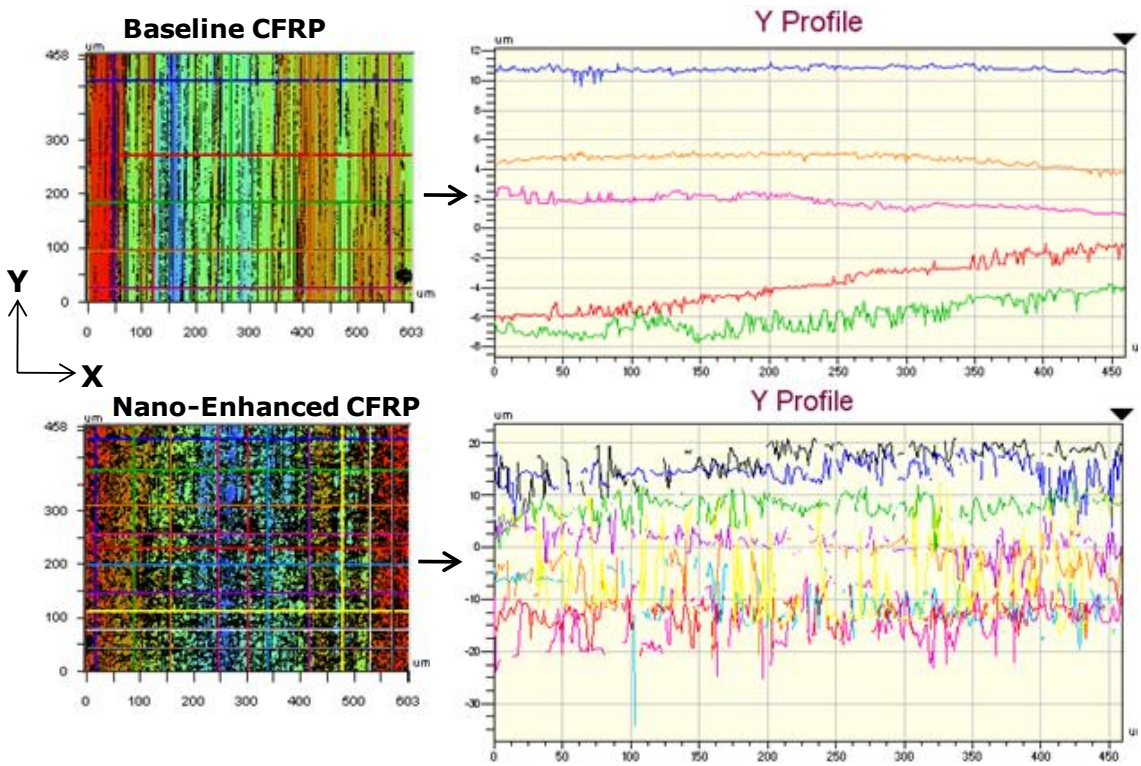

Figure 11 Topological profile based on vertical scanning interferometry.

$$R_a = \frac{1}{L}\int_0^L |z| dx \tag{1}$$

$$R_q = \sqrt{\frac{1}{L}\int_0^L z^2 dx} \tag{2}$$

Considering the electrostatic pole which draws the PVDF fibers from the capillary needle coupled with the bending instability experienced during the deposition, the PVDF fibers undergo significant thinning and straining during their flight to the target substrate. The MWCNTs within the solution are likely to be influenced and aligned within the PVDF fibers as a result. A series of TEM images have been obtained, as shown in Figure 12, to observe the distribution of MWCNTs within the PVDF fibers. There is evidence from these images

that the MWCNTs have a strong bias with elongation along the length of the PVDF fibers. There are, however, numerous instances of entanglements and nanotubes that are double backed along their own length. Kim et al [22] observed alignment of MWCNTs in polycarbonate due to the high longitudinal strain rate of the jet, similar to this present study, but they did not notice any sign of agglomeration. With the PVDF fibers being on the order of several hundred nanometers up to microns in diameter and the MWCNTs being on the order of microns in length and nanometers in diameter, this observation is not surprising even if the straightening during electrospinning is a more pronounced phenomenon. Depending on the application, the alignment is a factor that may be desirable.

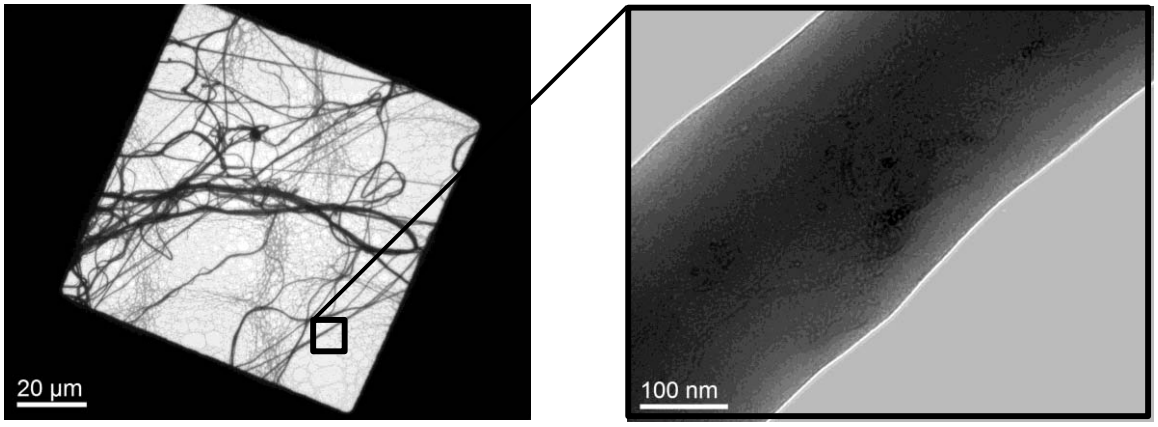

Figure 12 TEM images of single PVDF fibers showing the CNTs within.

As can be seen in Figure 13a and Figure 13b, many of the CNTs are elongated along the length of the electrospun fibers. This alignment is likely a result of the electrostatic poling process coupled with the mechanical straining during fiber formation. This would be useful in applications where CNT alignment is necessary, since it is possible to control the electrospun fiber direction and placement with a variation in the applied electric potential on the target. In this application, however, a random depositional mat with aligned CNTs will still result in a random CNT distribution network. Figure 13c and Figure 13d illustrate the CNT agglomeration and PVDF fiber coalescing. With aspect ratios on the order of 1000, the CNTs are highly likely to become entangled, even after sonication steps, leading to isolated regions of knotted CNTs. In addition, depending on the amount f time the solution sits after mixing and sonication before electrospinning, the affinity between CNTs in solution is strong enough to cause agglomeration in a well dispersed formulation over time. When the solution

is not well mixed with dispersed CNTs, the electrospinning process is not well controlled and the exiting solution tends to sputter out of the capillary needle as agglomerates are passed. This leads to issues with solidification of the PVDF solution and disruptions in the electrospinning process as the capillary needle and the associated plumbing must then be solvent cleaned and flushed.

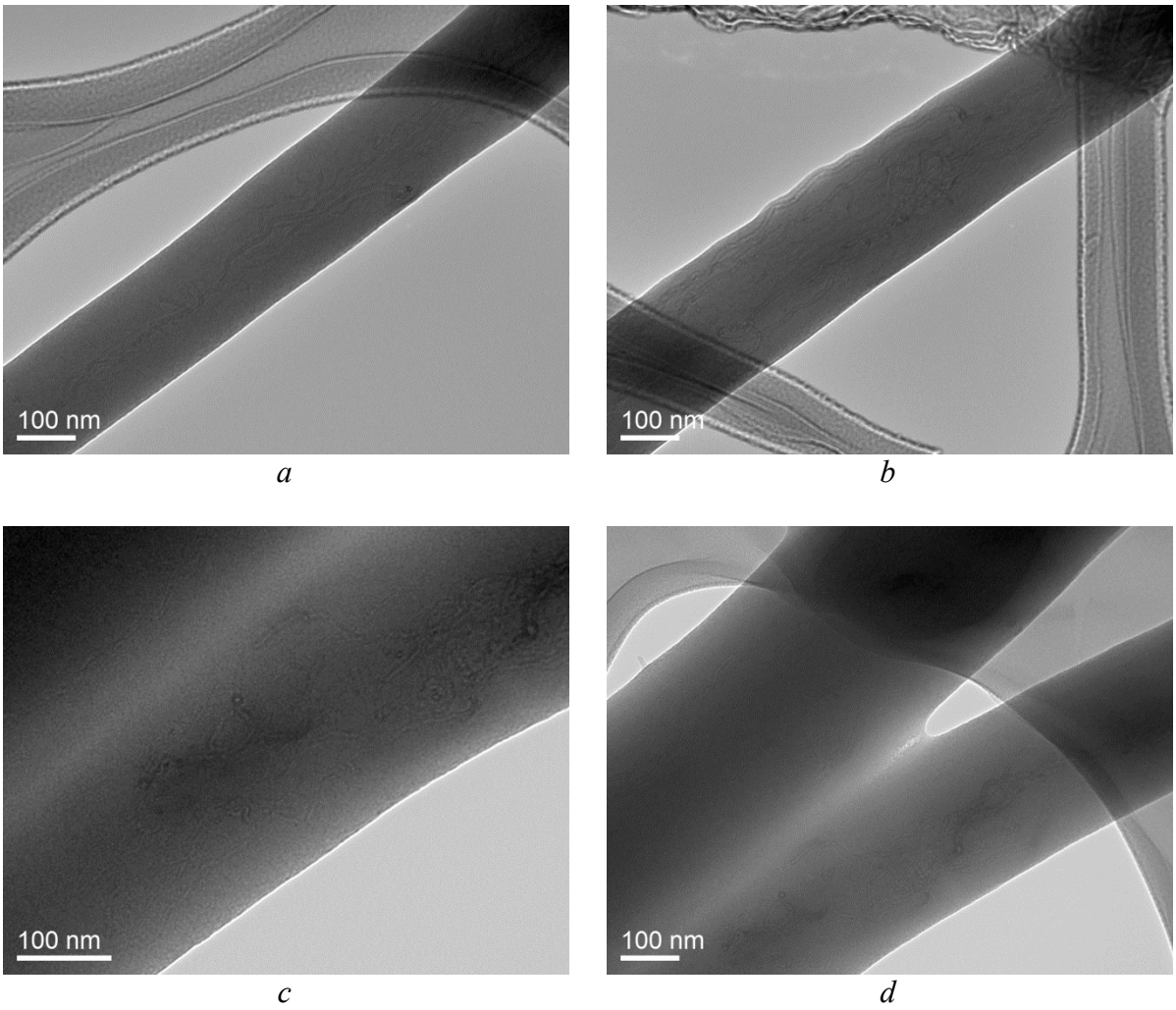

a *b* *c* *d*

Figure 13 Additional TEM images showing CNTs within electrospun fibers (a) and b) aligned, (c) agglomeration, and (d) electrospun fiber coalescing.

3.4 Conclusions

MWCNT‘s were mixed in a PVDF polymer solution for an electrospinning deposition process onto a carbon fiber reinforced polymer prepreg material in the uncured state. A sensitivity analysis was performed in order to optimize the depositional area, fiber diameter

and morphology of the electrospun PVDF fibers. It was found that there is a strong correlation with these parameters and the electric potential applied to the respective capillary needle and target, even when the relative potential is maintained constant between the two. The case when the potentials were equal in magnitude resulted in the largest depositional area with the smallest diameter and smoothest fibers. When the capillary needle was grounded and the voltage was applied only to the target, the fibers were much rougher and deposited over a drastically reduced region. These effects are thought to be attributed to the time of flight, evaporation of solvent, and the resulting instability due to bending during the drawing process. The drum rotation and capillary needle traversing during the electrospinning resulted in a homogeneous deposition with no directional dependence to PVDF fiber orientation, and increased surface roughness parameters. The MWCNTs were found to be primarily aligned within the PVDF fibers, likely due to the drawing and straining process when in flight. With homogeneity and isotropy associated with the PVDF fiber network, the same can be said about the MWCNTs within the fiber distribution plane.

4 THERMAL ANALYTIC RESPONSE

4.1 Introduction

The determination of the degree of a reaction and the kinetics of the polymerization utilizing Differential Scanning Calorimetry (DSC) is an important parameter to evaluate for the quality of a polymer based composites [37]. With an additive, such as PVDF-HFP doped with CNTs onto an epoxy based composite material, as described in the previous chapter, there may be a discernable effect in terms of the resulting exotherm and epoxy crosslinking in the composite system. Others have had success with detecting the influence of fillers on their polymer system in order to elucidate some fundamental issues and mechanisms resulting from their addition [38]. Direct correlations have been observed in terms of the DSC response for conducting fillers in PVDF polymer [39]. The PVDF polymer used in this present study is semi-crystalline and generally exists in one of two phases – the non-polar α-phase and the piezoelectric β-phase [40]. The β-phase is applicable to the electrospinning deposition process employed in this investigation as a result of the electrostatic field generated and the induced pole. The β-phase of PVDF has been investigated for the variation in the melt endotherm detected from DSC for the poled versus non-poled form [41]. The polymorphic phase transformations that are likely to occur from the depositional process, through the curing process, and then during testing are of concern. It has been shown that during fracture behavior there are micromechanisms of cavitation, spherulite breakdown, fiber bundle structure formation and a transition from the α to β-phase [42]. The implications to the mechanical response may be discernable during testing due to more or less brittle or ductile behavior as a result of the polymer structure and resulting degree of cure in the epoxy.

The thermal analytical analysis includes using DSC to evaluate the enthalpy of transition, ΔH, as the exothermic reaction of the chemical cross-linking event within the thermosetting polymer takes place, indicating a correlation with the extent of monomer conversion. A typical result illustrating the heat flux resulting from an exothermic reaction versus temperature can be seen in Figure 14. The integration required to obtain the enthalpy of transition or _heat of reaction,‘ ΔH, for the exothermic reaction is given as:

$$\Delta H = \int_{T_i}^{T_f} C_P dt = \int_{T_i}^{T_f} \left(\frac{K\Delta T}{q} \right) dT \tag{3}$$

where, C_p is the heat capacity, K is the thermal conductivity of the material, q is the heating rate, and the limits of integration are the initial and final temperature, T_i and T_f, respectively.

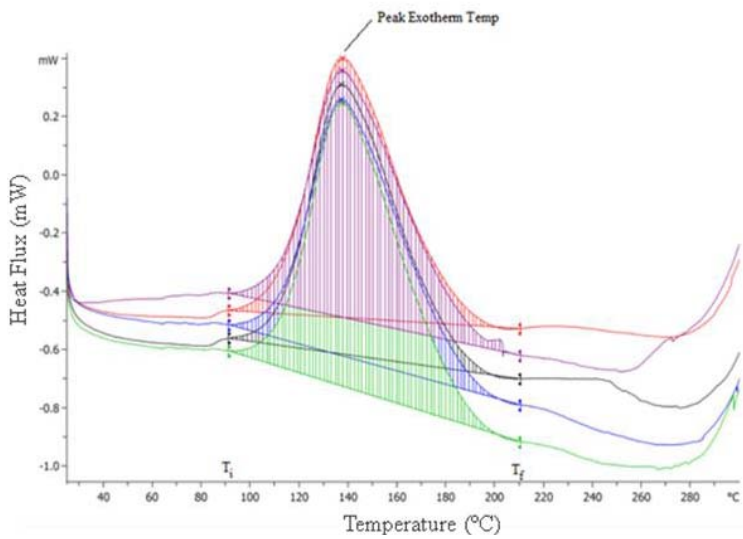

Figure 14 Typical DSC result showing the heat flux versus temperature.

In addition to the integration utilizing Equation (3), the peak temperature of the exotherm is also obtained. This is described as the temperature at which the heat flux, ϕ, meets the criteria:

$$\frac{d\phi}{dT} = 0 \tag{4}$$

These parameters have been directly measured for both the baseline CFRP material system and the CNT enhanced CFRP. The identification of any changes between the two systems will likely be correlated to variations in the binding thermoset epoxy as a result of the exposure to the solvent-based PVDF formulation. A sensitivity analysis was performed on fiber diameter and morphology as a function of applied electric potential, as described in Section 3.3. The smoothness of fibers obtained was correlated with sufficient evaporation of the solvents but was not investigated to determine trace solvent presence. The problem with

measuring trace solvents is that they will likely evaporate before they can be detected. If, however, the solvent did contact the surface of the epoxy based composite material without fully evaporating during the flight phase of the fiber formation, including the bending instability, there may be implications to the heat generated during the exothermic cure.

In addition to measuring the enthalpy of transition, the change in mass of the sample during a heating cycle was determined using thermal gravimetric analysis. This allows for the direct measurement of the mass loss associated with material degradation as critical temperatures are experienced. For this measurement, a baseline sample mass is tracked in-situ as the sample is heated to temperatures well beyond the cure temperature.

4.2 Experimental Methods

4.2.1 Materials

The CFRP material as well as the Polymer-based CNT formulation to enhance the baseline CFRP are the same as those listed in Section 3.2.1. This information is not repeated here for succinctness.

4.2.2 Specimen Preparation

Samples for differential scanning calorimetry are cut from the uncured CFRP material, both the baseline and CNT enhanced. Samples are cut using a rotary cutter with a razor wheel to approximately 5 mm squares. These squares are close in size to one another, however the results are all normalized with respect to mass to account for slight variations.

4.2.3 Testing Procedure

A Mettler Toledo DSC823E differential scanning calorimeter was used to measure the difference in heat flows between samples of interest – baseline CFRP and CNT enhanced CFRP – and a reference sample with air. The Metler Toledo software suite was utilized with this instrument to analyze and plot out all data results. Samples are encased within a 40 µl hermetically sealed aluminum (99.99 % pure) crucible. The hermetic seal suppresses any endothermic evaporation, vaporization or sublimation of volatile substances in the DSC.

Before mounting in the DSC turret, individual masses for each crucible are obtained before adding the sample. The samples are then sealed into the crucible using a sealing press to plastically deform the lid. Figure 15 illustrates the process and shows the DSC testing machine. The samples were then exposed to a heating ramp from room temperature at 25 °C up to 600 °C at 2.78 °C/min. Argon purge gas was used at a flow rate of 40 ml/min.

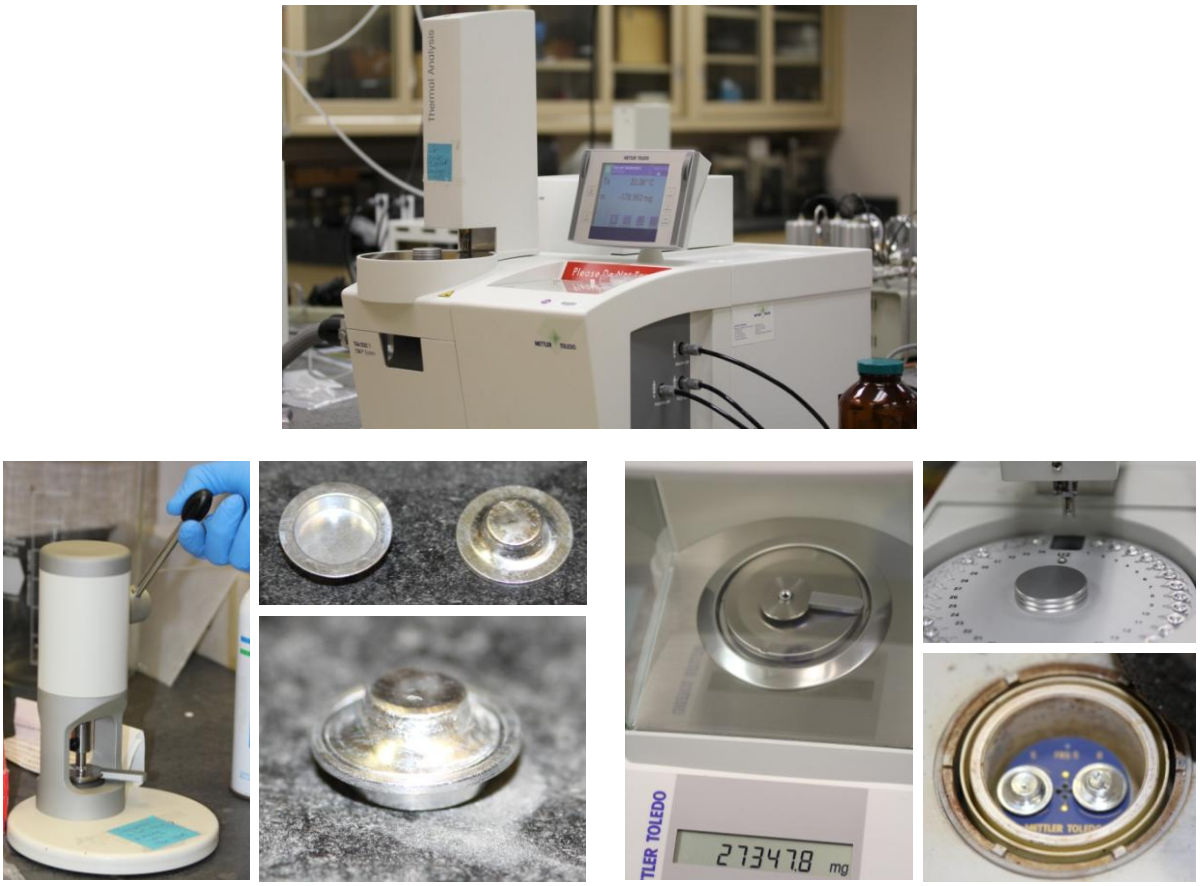

Figure 15 DSC with sample preparation and turret mounting.

For the thermal gravimetric analysis (TGA), a Metler Toledo TGA/DSC 1 model tester was utilized to measure the change in weight of the sample as it was heated. Similar to the DSC experiments, the samples were exposed to a heating ramp from room temperature at 25 °C up to 600 °C at 10 °C/min. Argon purge gas was used at a flow rate of 40 ml/min. In addition, the same crucibles were used to house samples of interest for analysis.

4.3 Results and Discussion

4.3.1 Differential Scanning Calorimetry

The resulting heat flow measurements, as described by the integration of Equation (3), can be visualized as the shaded regions in the plots of Figure 16 and Figure 17 for the baseline CFRP material and the CNT enhanced CFRP material, respectively. The integrations of interest is the initial exotherm, the exotherm associated with the polymeric crosslinking during the chemical curing process, which is shown in each respective plot as the first shaded region between approximately 100 °C and 250 °C. This is of interest to determine if the electrospinning of the PVDF-CNT formulation onto the CFRP prepreg material inhibits chemical crosslinking in any discernable way.

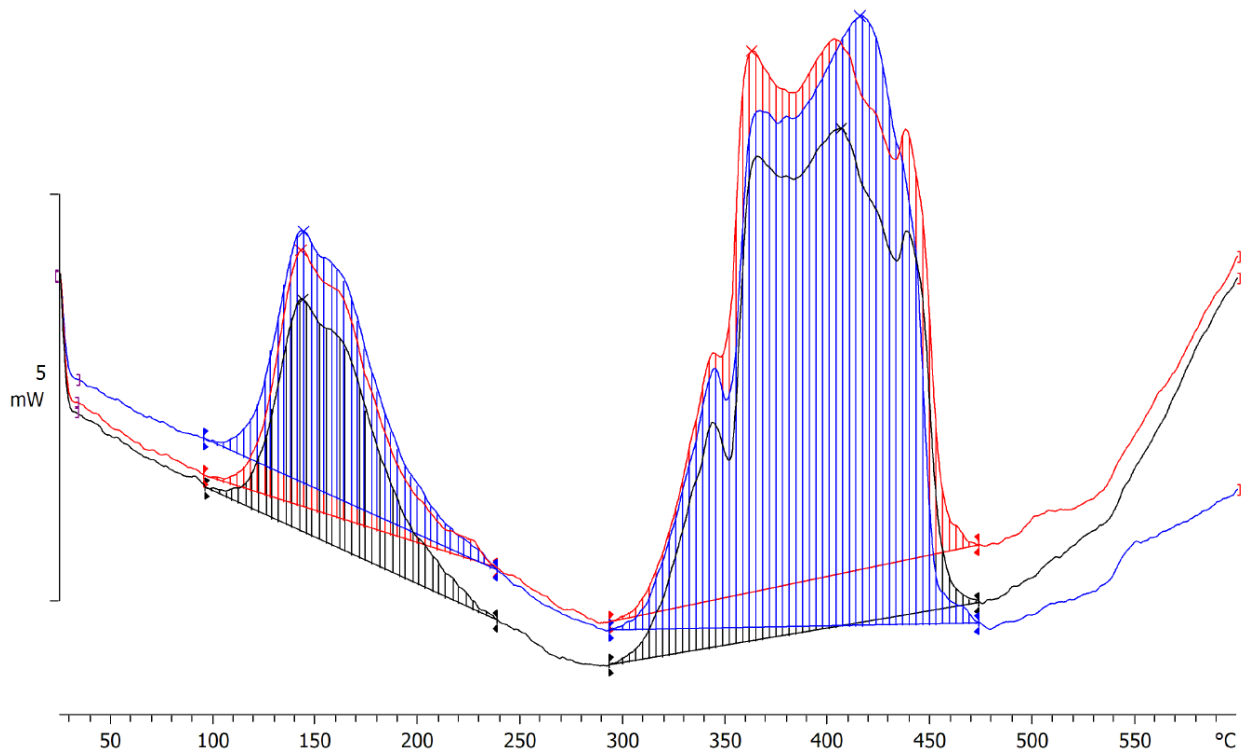

Figure 16 Baseline CFRP differential scanning calorimetry exotherm response showing integration area and limits.

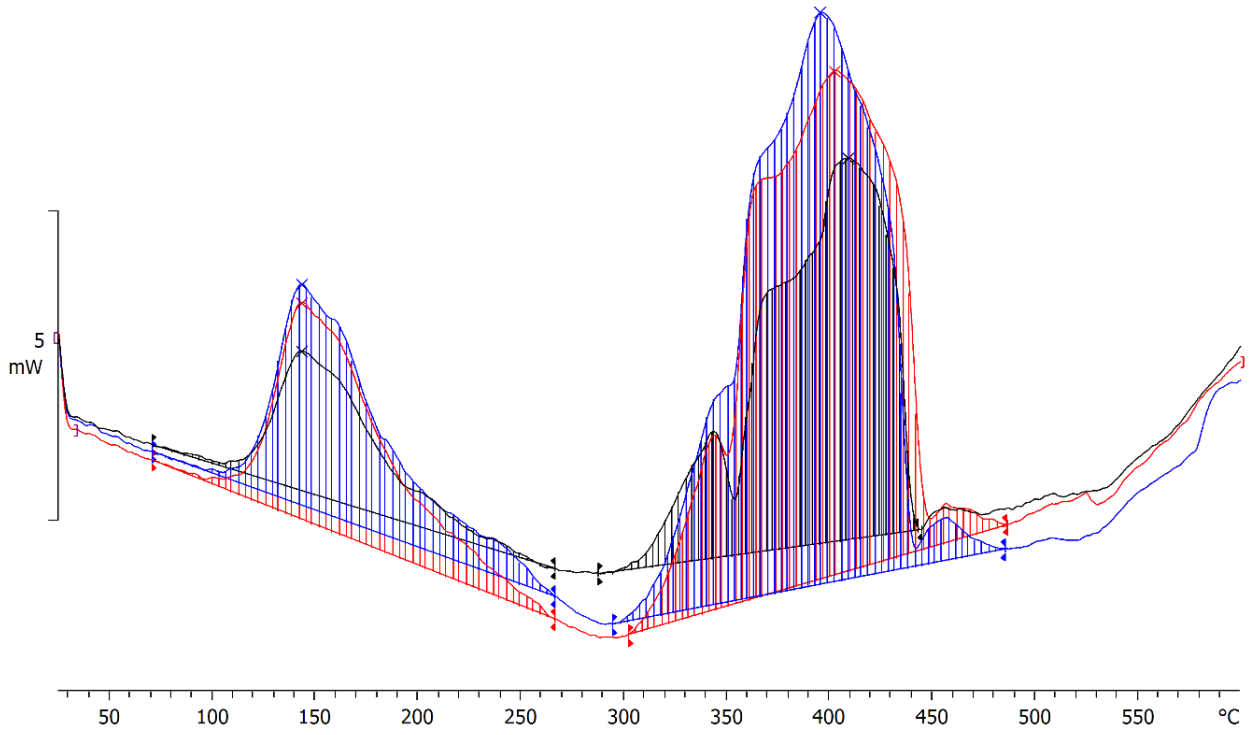

Figure 17 CNT enhanced CFRP differential scanning calorimetry exotherm response showing integration area and limits.

Evaluating the first integration region in each of the plots of Figure 16 and Figure 17 quantifies the energy given off from each sample. In addition, observing the peak temperature experienced during this exotherm provides another parameter to use for comparison sake. The results are plotted in Figure 18 and tabulated in Table 2 along with respective average values and standard deviations.

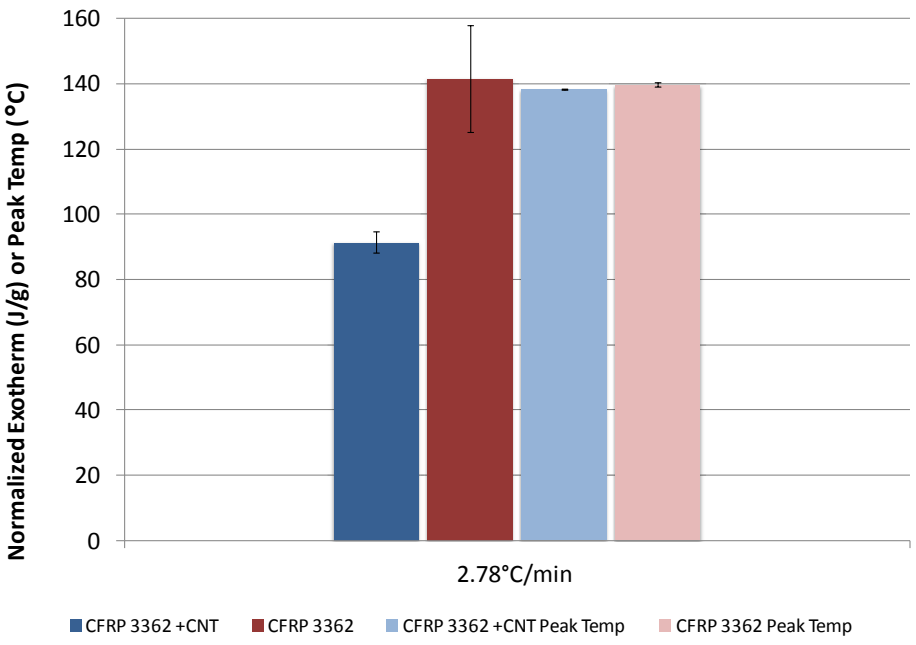

Figure 18 Sensitivity analysis on the integrated enthalpy of reaction and peak exotherm temperature for the baseline CFRP material compared with the CNT enhanced.

The initial exotherm for the baseline CFRP material averages approximately 142 J/g, which is a 55 % increase from the 91 J/g measured for the CNT enhanced CFRP. Interestingly, the standard deviation for the values obtained for the baseline CFRP is much higher than that of the CNT enhanced material, almost 5 times. It is likely that if there were still solvent present in the electrospun formulation when deposited onto the CFRP prepreg, the resulting exothermic reaction from the polymerization occurring within the DSC would have been hindered, possibly as a result of reduced number of bonds created from resulting polymer wrapping and lack of solvent evaporation. An additional explanation, possibly more likely, considers the melt temperature of the thermoplastic PVDF that is now present on the CNT enhanced CFRP. With a melt temperature being approximately 135 °C, this phase transition occurs during the exothermic reaction from the epoxy resin. Since the melting of the PVDF requires energy or heat, it is an endothermic process. This endothermic process from the melting of the PVDF is occurring during the exothermic process from the crosslinking of the epoxy. This would result in a net reduction in the overall exotherm as measured from the

DSC. There less than a 1 % change in the peak temperature experienced during the exotherm with a less than 1 °C standard deviation among all samples tested.

Table 2 DSC results comparing CNT modified CFRP with baseline material formulations for 2.78 °C/min heating rate.

	Normalized integral (J/g)		***Peak Temp (°C)***	
	CFRP62 with CNT	*CFRP62 Baseline*	*CFRP62 with CNT*	*CFRP62 Baseline*
Sample 1	*94.79*	*126.06*	*138.13*	*140.19*
Sample 2	*86.93*	*167.30*	*138.42*	*140.15*
Sample 3	*89.07*	*137.99*	*138.64*	*140.09*
Sample 4	*93.25*	*130.18*	*138.53*	*139.33*
Sample 5	*92.75*	*146.71*	*138.18*	*138.90*
Avg.	*91.36*	*141.65*	*138.38*	*139.73*
Std. Dev.	*3.25*	*16.37*	*0.22*	*0.58*

4.3.2 Thermal Gravimetric Analysis

The degradation of the samples has been directly measured using thermal gravimetric analysis (TGA). This procedure varies the temperature of the sample and allows for a mass loss during testing. The mass loss stems from the breakdown of the material and the phase change from solid or liquid to gas. This gas dissociates into the air and causes a reduction in the sample mass, which is carefully measured throughout the temperature sweep.

The baseline CFRP and CNT enhanced CFRP TGA response curves can be seen in Figure 19 and Figure 20, respectively. The samples all were slightly different initial masses, causing the curves to be shifted up or down on the plots. The onset temperatures for the transition and the overall percentage of mass loss during the transition were directly measured.

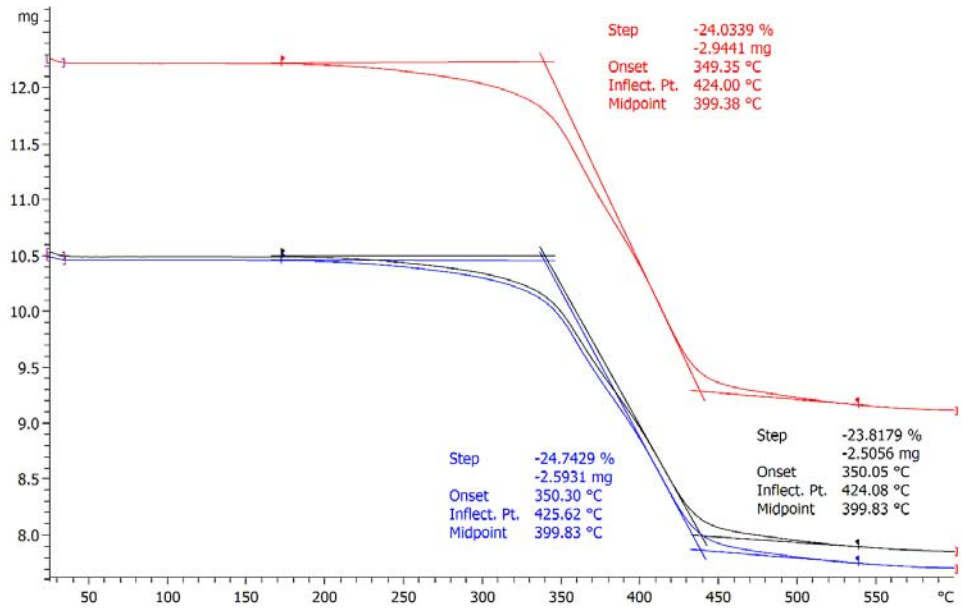

Figure 19 Baseline CFRP thermal gravimetric analysis response.

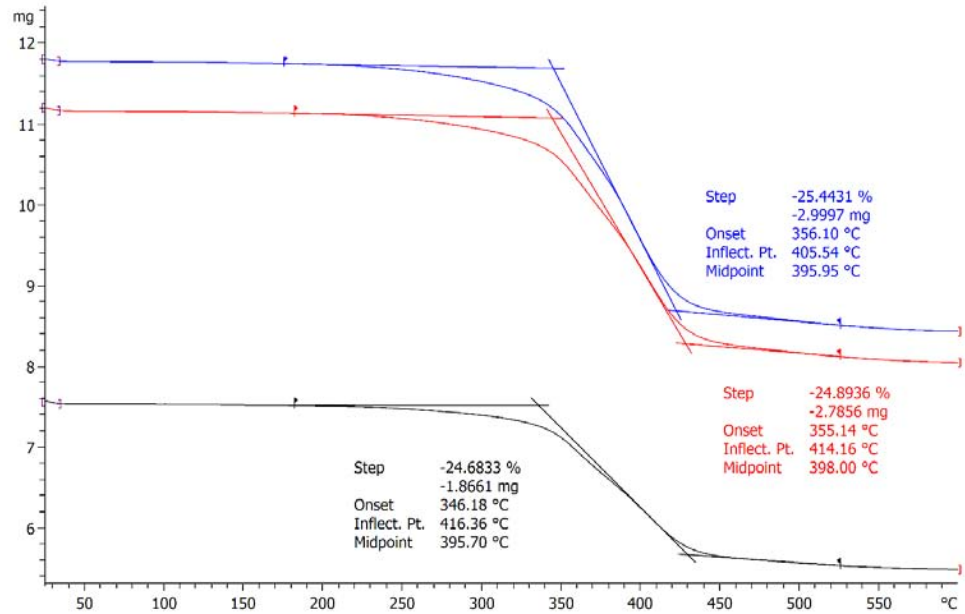

Figure 20 CNT enhanced CFRP thermal gravimetric analysis response.

At approximately 350 °C both material systems can be seen to demonstrate drastic reductions in mass loss. The overall degree of mass loss has been quantified and plotted in the graph of Figure 21. It has been shown that the mass loss for each of the systems is approximately the same within the experimental scatter. However, considering the second shaded region in the exothermic plots of Figure 16 and Figure 17 it can be seen that the qualitative behavior of the

heat transferred to each of the material types is different. This implies that even though the mass loss between the two samples was approximately the same, the manner in which the heat was utilized to accomplish this degradation was different. This is likely a result of the fundamental differences associated with the presence of the PVDF thermoplastic polymer and the lack thereof.

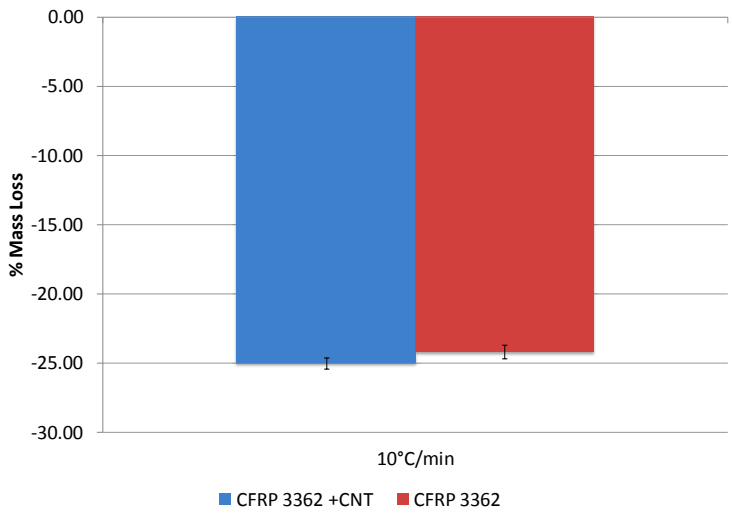

Figure 21 Mass loss resulting from TGA between 25 – 600 °C.

4.4 Conclusions

A thermal analytic study has been performed on the baseline CFRP and CNT enhanced CFRP materials. The enthalpy of reaction through differential scanning calorimetry and the mass loss degradation through thermal gravimetric analysis have been carefully measured and analyzed. It has been shown that the net exotherm given off as a result of the chemical kinetics associated with the crosslinking polymerization in the epoxy resin is countered by the endothermic melting transition in the PVDF thermoplastic. This causes a reduction in the exotherm from the baseline material by approximately 55 %. While the normalized exotherm changes drastically, the peak temperature experienced during this process does not vary by more than 1 %. Considering the second exothermic reaction, that associated with the material degradation and mass loss, the qualitative nature of the heat flow is unique to each material system, yet the extent of mass loss is not. Both materials exhibit a reduction in mass by approximately 25 % between a temperature range from 350 °C to 400 °C. This qualitative

difference in the second endothermic region is associated with the presence of the PVDF and the variation in thermal transport and storage within the material.

This page left intentionally blank.

5 DYNAMIC MECHANICAL ANALYSIS

5.1 Introduction

The thermo-mechanical analysis involves utilizing Dynamic Mechanical Analysis (DMA) to evaluate the elastic and viscous properties of the cured baseline and CNT enhanced composite material systems. DMA is used to apply a stress or a strain to a sample, often under a variation in temperature and loading amplitude. The elastic and viscous properties of the material are measured and quantify its ability to store and dissipate energy, respectively, when cycled under mechanical loading. The temperature dependent response with respect to the glass transition temperature, T_g, the storage modulus, E‘, and the loss modulus, E‘‘ are measured during the experiment. The DMA technique is very sensitive to the motions of the polymer chains and a powerful tool for measuring the transitions in polymers, estimated to be 100 times more sensitive to detecting the T_g over DSC [43]. DMA has been shown to be a useful tool for investigating the interfacial properties of fiber reinforced polymers [44]-[46]. DMA has also been used to determine the sensitivity of nanocomposite materials to doping content levels [47]. It has been shown that increasing the content of CNTs within the polymer matrix increases the storage modulus while broadening and shifting the loss modulus peak to higher temperatures, implying more thermal stability and higher Tg [48]. The CNTs are likely restricting the polymer flow resulting in a higher stiffness. The dispersion and mixing technique before consolidation has also shown to have an effect on the overall response under DMA loading [49].

In order to develop the fundamental equations to describe the DMA testing procedure in this investigation, elasticity theory is used to describe the stress and strain relations through beam theory. From the Euler-Bernoulli approach to flexure, the transverse displacement function, *v(x)*, for a simply supported beam, as shown in Figure 22, can be shown to be

$$v(x) = \frac{Px}{48EI}(3L^2 - 4x^2) \tag{5}$$

where the isotropic, elastic modulus is E and the second area moment of inertia is I, a function of the thickness, t, and width, w. When $v(x)$ is evaluated for the maximum value, which occurs when x is $L/2$, the transverse displacement is given as

$$v\left(\frac{L}{2}\right) = \frac{PL^3}{48EI} \tag{6}$$

with

$$I = \frac{wt^3}{12} \tag{7}$$

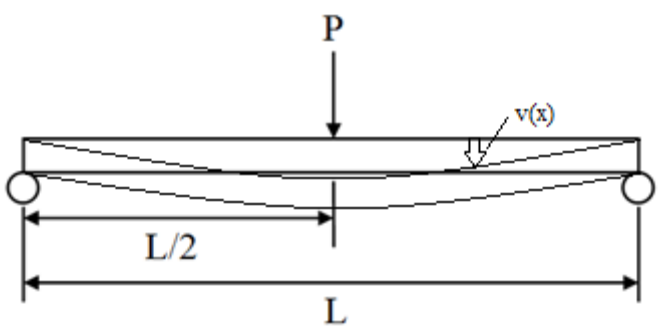

Figure 22 Schematic of the three-point flexure experiment.

By balancing moments about the neutral axis, assuming a linear distribution of strain any distance, y, from the neutral axis, as well as a linear relationship between stress, σ, and strain, ε, the flexural (or bending) stress, σ_b, can be shown to be

$$\sigma_b = \frac{M(x)y}{I} \tag{8}$$

When Equation (8) is evaluated with $M(x)$ equal to $Px/2$, along with the insertion of the equality shown in Equation (7), the flexural stress at a distance $y = t/2$ from the neutral axis is given as

$$\sigma_b = \frac{3PL}{2wt^2} \tag{9}$$

Recall from Equation (5), the transverse displacement, *v(x)*, at $x = L/2$ is given as

$$v\left(\frac{L}{2}\right) = \frac{PL^3}{48EI} = v \tag{10}$$

Then, the flexural modulus, E_{flex}, can be determined as

$$E_{flex} = \frac{L^3}{4wt^3}\left(\frac{P}{v}\right) \tag{11}$$

Using Hooke's Law for the linear relationship between stress and strain, the strain, ε, can be determined to be

$$\varepsilon = \frac{\sigma}{E_{flex}} = \frac{\frac{3PL}{2wt^2}}{\frac{L^3}{4wt^3}\left(\frac{P}{v}\right)} = \frac{6vt}{L^2} \tag{12}$$

Using the result of Equation (12), the strain magnitude can be determined for the sample geometry. The stress (or strain) is applied in a sinusoidal manner, such that

$$\sigma = \sigma_0 \sin(\omega t + \delta) \tag{13}$$

and

$$\varepsilon = \varepsilon_0 \sin(\omega t) \tag{14}$$

where, σ_0 is the stress amplitude, ε_0 is the strain amplitude, ω is the frequency, t is the time, and δ is the phase lag between stress and strain. The storage and loss modulii, E' and E'', respectively, are defined as

$$E' = \frac{\sigma_0}{\varepsilon_0}\cos(\delta) \tag{15}$$

and

$$E'' = \frac{\sigma_0}{\varepsilon_0}\sin(\delta) \tag{16}$$

So, taking the quotient of the loss modulus to the storage modulus gives

$$\frac{E''}{E'} = \frac{\frac{\sigma_0}{\varepsilon_0}\sin(\delta)}{\frac{\sigma_0}{\varepsilon_0}\cos(\delta)} = Tan(\delta) \tag{17}$$

The *Tan (δ)* is a derived quantity, as can be seen in Equation (17), and is useful for determining characteristic changes in a cured polymer, such as the T_g when *Tan (δ)* is maximum, and for an uncured polymer to determine the gelation point, when *Tan (δ)* is unity. A typical plot showing the relationship between the quantities defined in Equations (15), (16), and (17) can be seen in Figure 23.

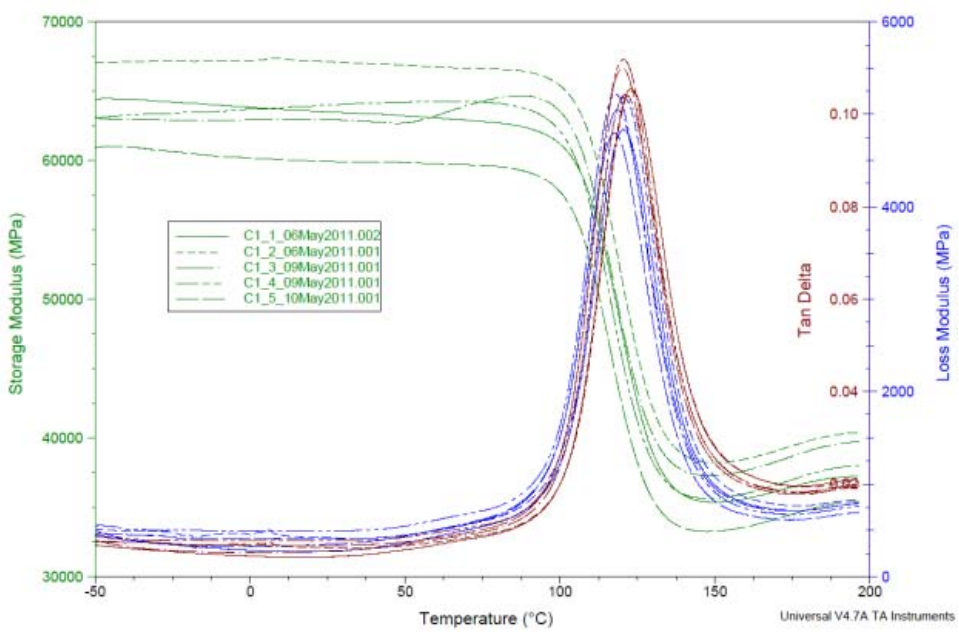

Figure 23 Typical DMA plot Showing the Storage Modulus, Loss Modulus, and tan δ.

5.2 Experimental Methods

5.2.1 Materials

The CFRP material as well as the Polymer-based CNT formulation to enhance the baseline CFRP are the same as those listed in Section 3.2.1. This information is not repeated here for succinctness.

5.2.2 Specimen Preparation

Specimens were hand-layed up to be balanced and symmetric with respect to warp and fill directions. Both the baseline CFRP laminates as well as the CNT enhanced CFRP laminates were prepared to be 2 plies in thickness with the electrospun layer located at the mid-thickness plane for the CNT enhanced specimens. The geometric parameters are listed in Table 3. Specimens have been cured using a recommended autoclave cure cycle at 350 °F, then cut to size using a wet diamond saw.

Table 3 DMA experimental specifications for CFRP material.

Material	***Baseline CFRP***	***CNT Enhanced CFRP***
Number of Plies	*2*	*2*
Stack Sequence[2]	$[0/90]_s$	$[0/90]_s$
Thickness (mm)	*0.84*	*0.84*
Width (mm)	*10*	*10*
Length (mm)	*57*	*57*

5.2.3 Testing Procedure

The experimental set-up is defined in Table 4. For each condition, at least 3 specimens were evaluated to maintain statistical significance. The amplitude level chosen was intended to maintain the material response well within the elastic regime. When considering the shear and moment diagrams for a simply supported, three-point flexure test, the shear is constant along the entire neutral axis with a change in sign at the mid-span, loading point. With the

[2] The 8 harness satin weave is defined with the warp and fill directions as the 0º and 90º orientations, respectively. Additionally, one lamina is defined as two sub-lamina for the purposes of a stack sequence, i.e. one ply with the warp up and fill down would be described as [0/90].

shear force, V, equal to $P/2$, the maximum shear stress along this mid-thickness plane can be shown to be equal to $3V/2A$ for the rectangular cross section. Since the applied load, P, is varying sinusoidally, the shear stress is as well.

Table 4 DMA testing specifications for baseline CFRP and CNT enhanced CFRP.

Loading	*3 Point Flexure*
Load Span	*50 mm*
Cylindrical Supports	*4 mm Diam.*
Amplitude	*1000 µm*
Frequency	*1 Hz*
Temperature Range	*-50 to 250ºC*
Temperature Ramp	*2.78 ºC/min*

As shown in Table 5, the strain amplitude is approximately 0.16 % for each specimen type, which is well below the strain to failure for this material, being around 1 %. The specimens have been loaded in displacement control with an amplitude of 1000 µm, as described in Table 4. This amplitude can be used, along with geometry, in Equation (12) to determine the strain amplitude as 0.115 %, as listed in Table 5. The temperature within the test chamber was then swept from -50 to 250ºC at a prescribed rate of 2.78 ºC/min.

Table 5 DMA specimen specifications for CFRP and CNT enhanced CFRP.

Material	***Baseline CFRP***	***CNT Enhanced CFRP***
Thickness (mm)	*0.84*	*0.84*
Length (mm)	*57*	*57*
Strain (%)	*0.155*	*0.155*

The specimens have been loaded with a instrumented feature known as ‗Force Track.‘ This feature ensures that, while the testing is displacement control, the loading clamp never loses contact with the specimen during compliance changes over the temperature spectrum. This is analogous to a non-zero mean stress in fatigue testing. An image of the specimen mounting fixture and loading apparatus can be seen in Figure 24.

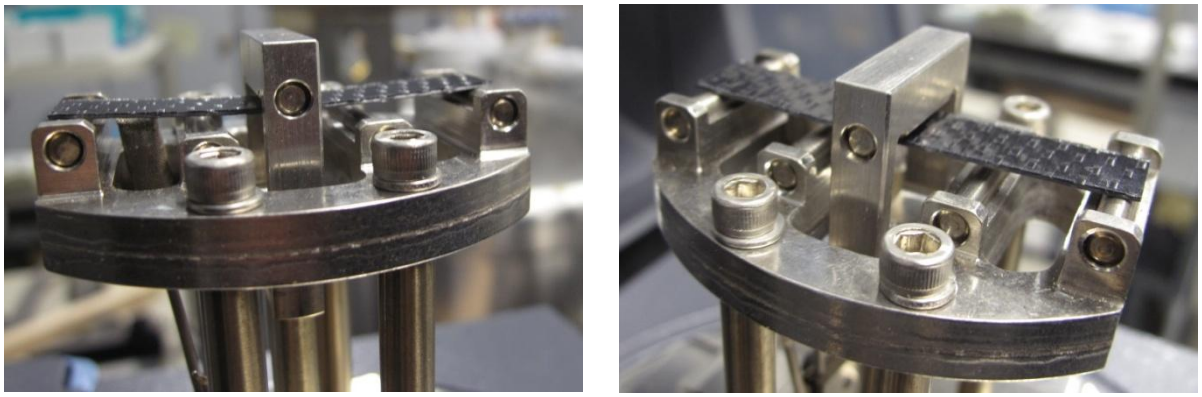

Figure 24 Three-point flexure experimental setup for DMA.

5.3 Results and Discussion

The loss modulus, storage modulus, and glass transition temperatures have been closely investigated and plotted for each respective material system. As can be seen in Figure 25 and Figure 26, the superposed loss and storage modulii, as well as the *Tan (δ)*, are plotted for the baseline CFRP and the nano-enhanced CFRP, respectively.

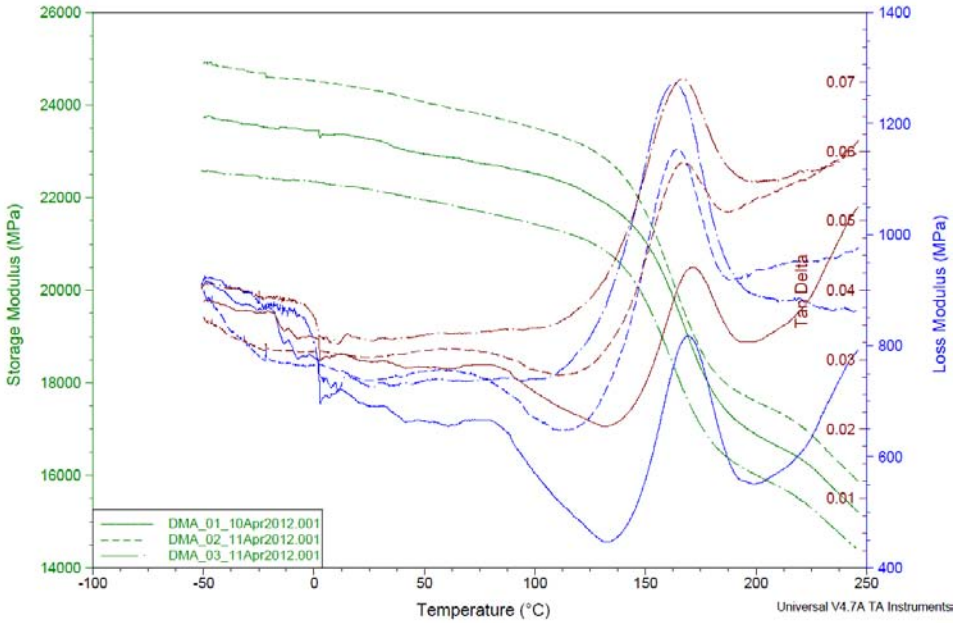

Figure 25 CFRP baseline DMA results for -50 to 250 °C.

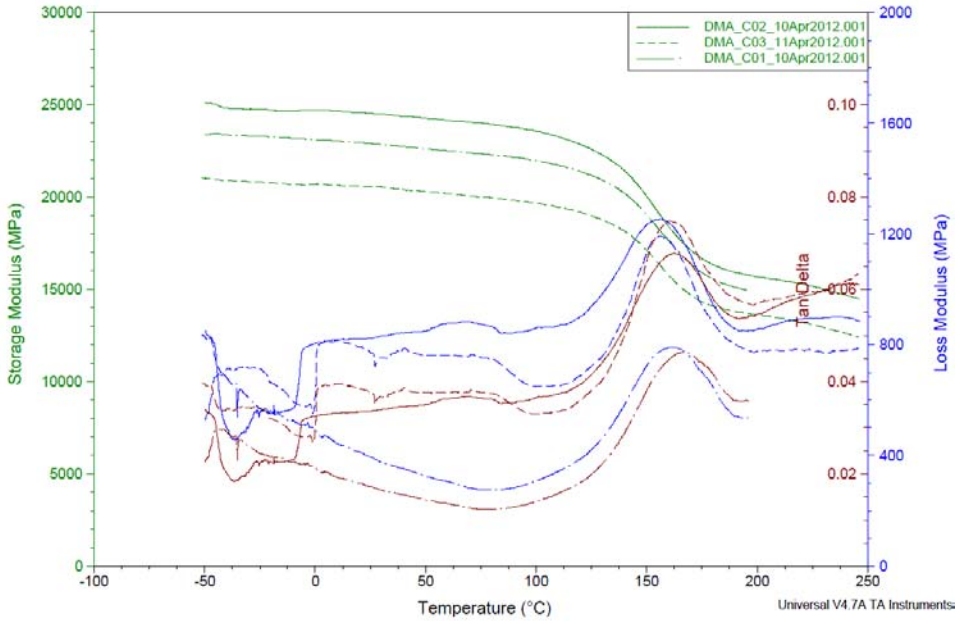

Figure 26 Nano enhanced CFRP DMA results for -50 to 250 °C.

The inflections associated with the storage modulus response curves are due to the glass transition temperature of the material. This is correlated with the rise in the loss modulus as the material becomes much more viscous with dissipating mechanisms, primarily in the form of heat generation. As the loss modulus increases and the storage modulus decreases, recall from Equation (17), the *Tan (δ)* value will increase to a local maximum as well. In the spirit of comparison, the individual response curves for the measured values have been plotted for each material system in Figure 27 through Figure 29. The systems are superposed over one another to highlight both similarities and differences.

The loss modulus can be seen in Figure 27 for each system. The response curves amongst the different systems are very similar within the experimental scatter associated with the test. The baseline system includes in the nomenclature DMA_XX, with the _XX‘ representing the specimen number. The nano-enhanced is denoted as DMA_CXX, with the _C‘ denoting carbon nanotube enhanced. Aside from the scatter associated with the low temperature measurements, the most obvious and consistent difference between the two systems is the offset of the loss modulus peak. This correlates with the shift in the storage modulus inflection and the shift in the local maximum of the *Tan (δ)*. With the nano-enhanced system having the reinforcement of CNTs within a thermoplastic polymer, the magnitude of the

dissipating ability is unaffected. Note that this enhancement is located only at the mid-plane, neutral axis of the specimen. This 3-point flexure is transmitting shear stress along this enhanced interface, but it is also strongly dependent on the fiber properties of the composite under both tension and compression, an ability that is equal for both sets of specimens as a result of the same fibers. However, though no noticeable change in the magnitude has occurred, the shift of the peak from a higher temperature to a lower temperature for the baseline to CNT enhanced, respectively, implies that the glass transition has been lowered. In fact, the Tg has reduced by approximately 15 °C due to the presence of the PVDF solution.

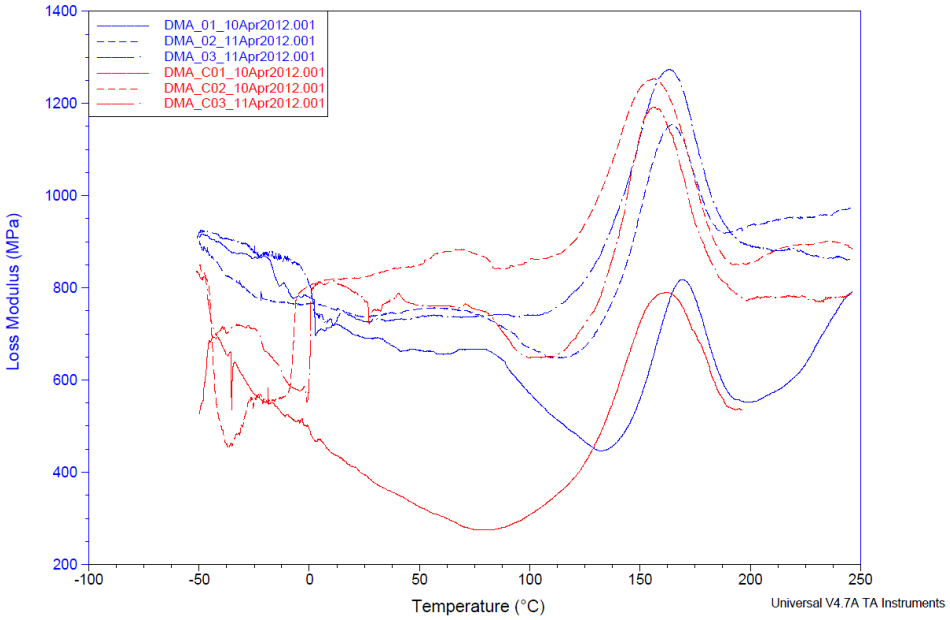

Figure 27 Nano enhanced CFRP versus baseline material comparing the measured storage elastic modulus from dynamic mechanical analysis from -50 to 250 °C.

The shift in the Tg is further highlighted from the plot of the storage modulus shown in Figure 28. The inflection point of this plot is generally taken as the demarcation for the glass transition. The transition can occur over a range from approximately 20-40 degrees, so this inflection point was consistently chosen as the T_g. With the PVDF and the CNT reinforcement, the T_g has been reduced. A likely source for this reduction is that the PVDF polymer is a much more compliant, thermoplastic material when compared with the epoxy resin. The epoxy is a crosslinked system with high stiffness. The addition of the PVDF formulation, which has a melt temperature of 135 °C, results in the softening of the material at a lower temperature. In addition, for temperatures beyond the Tg, the storage modulus is

approximately 14 % higher for the baseline material. This implies that the effect of enhancing the neutral axis with the electrospun CNT formulation not only shifts the T_g but also gives rise to a reduced compliance above T_g. In addition, the resulting *Tan (δ)* shows increased dissipating proportionality above T_g in Figure 29. These effects are in contrast to what others [49] have found, but with different polymer-based material systems.

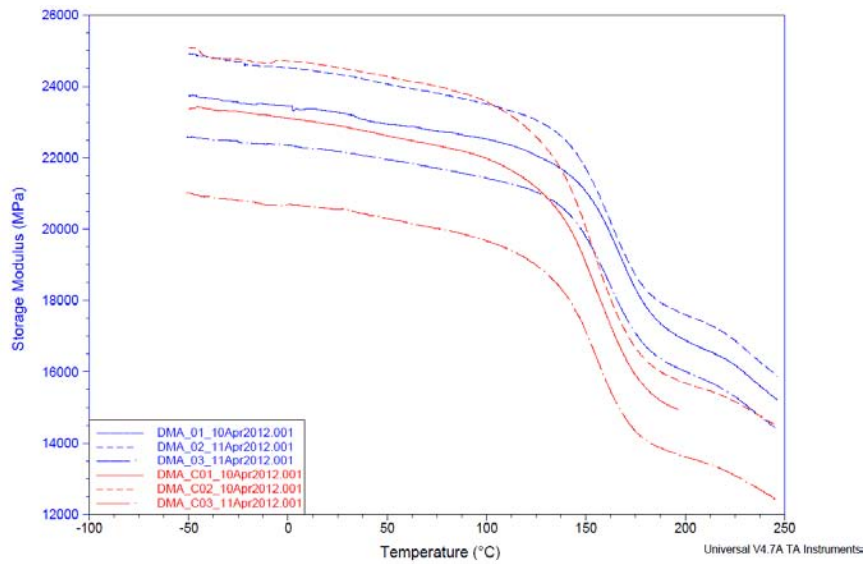

Figure 28 Nano enhanced CFRP versus baseline material comparing the measured storage elastic modulus from dynamic mechanical analysis from -50 to 250 °C.

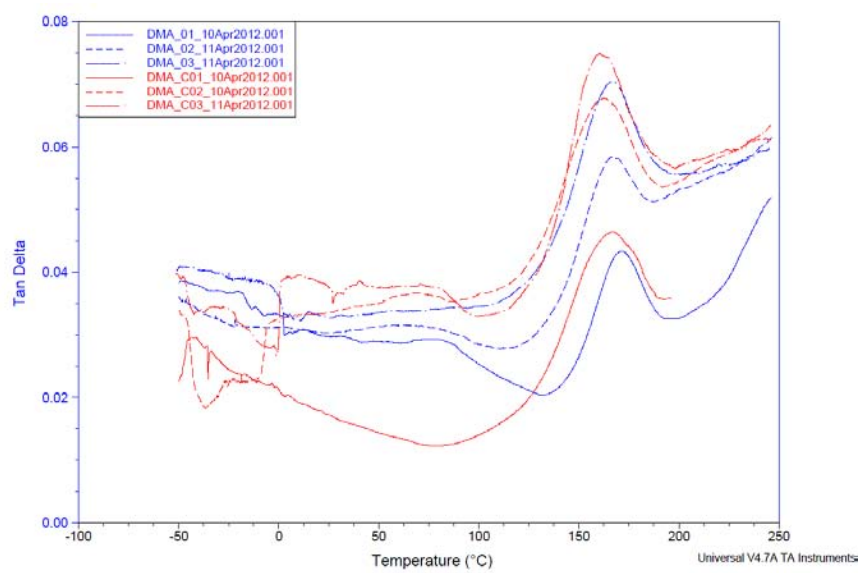

Figure 29 Nano enhanced CFRP versus baseline material comparing the measured *Tan (δ)* from dynamic mechanical analysis from -50 to 250 °C.

5.4 Conclusions

A systematic series of dynamic mechanical analysis has been performed on the baseline CFRP and nano-enhanced CFRP material systems. Loading was displacement controlled under a flexure scenario with sinusoidal variation in stress and strain. Though the interface along the neutral axis was the only difference between the baseline and CNT enhanced, the shear transfer during flexure was discernable in terms of the glass transition behavior, the storage modulus, and the *Tan (δ)*. The following conclusions have been found:

- The glass transition temperature for the CNT enhanced system has been reduced by approximately 15 °C. This is attributed to the lower melt temperature of the PVDF.
- The storage modulus has reduced by approximately 14 % at temperatures above the glass transition. This is attributed to the compliant nature of the PVDF thermoplastic polymer.
- The Tan Delta reveals that the relative proportion between the storage and loss modulus increases for the CNT enhanced system, implying more dissipating characteristics above the glass transition.

This page left intentionally blank.

6 MODE I FRACTURE CHARACTERIZATION

6.1 Introduction

In order to both qualitatively understand the mechanisms of fracture and growth behavior, as well as quantitatively determine the fracture properties of the material for advanced simulation and design, isolation of the fracture mode is necessary to eliminate extrinsic effects. With the Mode I fracture toughness being generally lower for polymers compared with the mode II value, it is often the initiating mechanism. This is coupled with the fact that when considering the rotation of the stress tensor for a condition of pure shear, as is the case for many scenarios of transverse loading on a composite stack sequence, there exists inclined normal forces at 45° that will likely cause micro void formation in brittle materials leading to coalescence and growth, making a mode II loading scenario ultimately governed by mode I micro-mechanical fracture behavior [50]. This is of concern for a variety of loading scenarios and damage mechanisms, predominantly subsurface interply delamination.

Nanotube modified polymer composites have been explored for the exceptional mechanical properties CNTs possess, with tube modulus on the order of a 1 TPa [51]. With promising properties, the implementation into structural composite materials is still undefined. Despite an increasing effort to incorporate CNTs into composites and resin formulations, especially for fracture toughness improvements [52]- [53], there is still much uncertainty in regards to the load transfer and energy absorbing mechanisms [54]. The CNT pullout mechanism is one energy absorbing process that has been shown to depend on the surface modifications [55]-[56] such as functionalization or polymer wrapping. When the interfacial shear transfer of tensile load is applied to the CNTs, the tensile stress transmitted can remove the CNT from the surrounding polymer matrix. When the interfacial transfer through tensile stress is high enough, CNT fracture may occur [57]. The loads are transmitted through the binding resin and to the CNTs. This is analogous to a traditional fiber reinforced composite material. Load redistribution occurs when one CNT fractures, resulting in the increased loading on neighboring CNTs [58]. When the external loading is compressive in nature, localized buckling of the CNTs has also been observed [59].

This chapter will explore the theoretical approaches to characterize the fracture properties of the baseline and CNT modified CFRP material. In addition, it will discuss the results from Mode I testing in terms of the measured properties to the fracture morphology. The following chapter will then complement these results with finite element simulations.

6.2 Analytical Methods

A series of analytic techniques have been explored in this study in order to understand the limitations, benefits, and implications of each for the application to experimental data. Each method is briefly discussed below.

6.2.1 Area Method

The critical strain energy release rate, G_{Ic}, is the rate of strain energy released with respect to the generation of new surface area created. It can be written in its simplest form as

$$G_{Ic} = \frac{\Delta U}{\Delta A} \tag{18}$$

Where ΔU *and* ΔA are the area under the load-deflection response curve and change in surface area, respectively, for fracture growth. For a specimen with a constant width, B, this can be rewritten as

$$G_{Ic} = \frac{\Delta U}{B\Delta a} \tag{19}$$

where Δa is the change in crack length. Using the Area Method, the change in elastic strain energy can be simply determined by numerical integration to calculate the area between curves at crack lengths a_1 and a_2 shown in Figure 30.

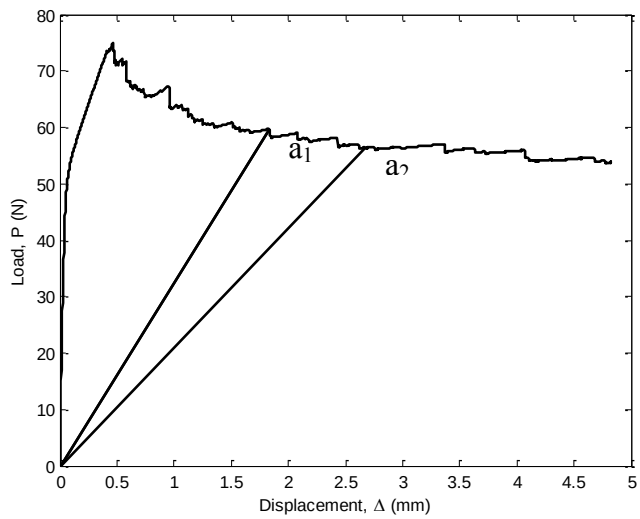

Figure 30 Typical load-displacement response for a DCB experiment.

Numerical integration can be achieved using the relationship

$$\Delta U = \int_{a_1}^{a_2} P d\Delta = \sum_{i=1}^{n} \frac{1}{2}\left[P_i \Delta_{i+1} - P_{i+1}\Delta_i\right] \tag{20}$$

where n is the number of data points collected between points 1 and 2 in Figure 30 to calculate the change in strain energy for each crack growth iteration. The external load, P, is applied to cause a displacement, Δ. The change in crack length, a, is given by

$$\Delta a = a_{i+1} - a_i \tag{21}$$

where a_{i+1} is the crack length at point $i+1$, and a_i is the crack length at point i. This can be used to calculate strain energy release rate using Equation (19).

6.2.2 Compliance Method

Using linear-elastic fracture-mechanics (LEFM), the strain energy release rate under displacement control can be shown to be

$$G_{Ic} = \frac{P^2}{2B}\frac{dC}{da} \tag{22}$$

where $\frac{dC}{da}$ is the slope of the compliance, C, versus crack length, a, relationship. Compliance is the inverse of stiffness and can be written in terms of the applied load, P, and the displacement, δ, given by

$$C = \frac{\delta}{P} \tag{23}$$

To determine $\frac{dC}{da}$ based on experimental results, a plot of compliance with respect to crack length must be constructed and an appropriate curve fit is performed to the data. The curve fit is then differentiated with respect to crack length, and used in Equation (22) to determine G_{Ic}. This calculation must be performed at each respective crack growth measurement obtained. The results are then generally plotted as a function of crack length.

6.2.3 Load Method

The load method uses Euler-Bernoulli beam theory to evaluate G_{Ic}. A schematic of the DCB used for testing can be found in Figure 31.

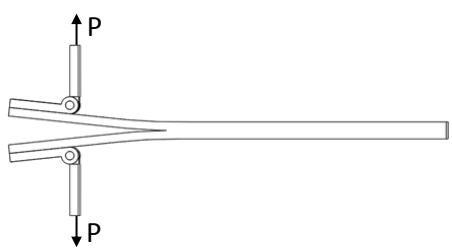

Figure 31 Schematic of the DCB experiment.

The separated region can be treated as two cantilever beams with their beam length equal to the crack length. Euler-Bernoulli beam theory can be used to calculate the vertical displacement of a cantilever beam at any point. For an end loaded cantilever beam with one end fixed, the load-displacement response can be shown to be

$$\delta = \frac{Pa^3}{3EI} \tag{24}$$

where E is the elastic modulus, and I is the second area moment of inertia. The load method uses beam theory to define the load-displacement relationship to determine $\frac{dC}{da}$ to be used in Equation (22). The displacement measured by the crosshead, Δ, is twice that given by Equation (24), with the most general form of an asymmetric double cantilever beam (ADCB) shown in Figure 32.

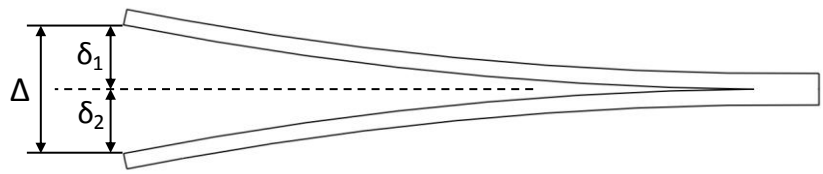

Figure 32 Asymmetric double cantilever beam (ADCB) schematic.

The crosshead displacement is the sum of the beam tip displacements of the upper and lower sections, given by

$$\Delta = \delta_1 + \delta_2 \tag{25}$$

where $\delta_1$and δ_1 are the beam tip deflections for the upper and lower segments of the ADCB, respectively. For a symmetric DCB,

$$\Delta = 2\delta \tag{26}$$

The crosshead displacement can then be used to evaluate the compliance by combing Equation (24) with Equation (25)

$$C = \frac{\Delta}{P} = \frac{2a^3}{3EI} \tag{27}$$

G_{Ic} can now be defined from Equation (22) by differentiating Equation (27) with respect to a, requiring only the respective load at each crack propagation, along with material properties and geometry. It is given as

$$G_{Ic} = \frac{P^2 a^2}{BEI} \tag{28}$$

6.2.4 Displacement Method

The displacement method simply takes the result of Equation (27) to solve for the load, P, giving

$$P = \frac{3\Delta EI}{2a^3} \tag{29}$$

Then, substitution of Equation (29) into Equation (28) allows G_{Ic} to be calculated independent of material properties as

$$G_{Ic} = \frac{\left(\frac{3\Delta EI}{2a^3}\right) Pa^2}{BEI} = \frac{3P\Delta}{2Ba} \tag{30}$$

In addition, using beam theory and the load-displacement response of the DCB, the flexural modulus can be calculated using Equation (29) and

$$I = \frac{Bh^3}{12} \tag{31}$$

where h is the thickness of the beam. The flexural modulus is then given as

$$E = \frac{8Pa^3}{Bh^3\Delta} \tag{32}$$

6.2.5 Beam Theory Method

Due to the difficulty in accurately measuring the crack length, a final method was developed to calculate G_{Ic} independent of crack length using simple beam theory. Combining Equation (24) with Equation (25) for an ADCB, the crosshead displacement can be written as

$$\Delta = \frac{4Pa^3}{B}\left(\frac{1}{E_1 h_1^3} + \frac{1}{E_2 h_2^3}\right) \tag{33}$$

Where E_1 and E_2 are the elastic modulus for the upper and lower segments, and h_1 and h_2 are the respective thicknesses of the upper and lower beams. Equation (33) can then be rearranged to solve for the crack length as

$$a = \left[\frac{B\Delta}{4P}\left(\frac{1}{E_1 h_1^3} + \frac{1}{E_2 h_2^3}\right)^{-1}\right]^{1/3} \tag{34}$$

The compliance can be found using Equation (33) and dividing out the applied load, P. The compliance can then be expressed as a function of crack length, material properties, and geometry and is given by

$$C = \frac{4a^3}{B}\left(\frac{1}{E_1 h_1^3} + \frac{1}{E_2 h_2^3}\right) \tag{35}$$

Equation (35) is differentiated with respect to the crack length, a, to yield

$$\frac{dC}{da} = \frac{12a^2}{B}\left(\frac{1}{E_1 h_1^3} + \frac{1}{E_2 h_2^3}\right) \tag{36}$$

to be used in Equation (22). Substituting Equation (34) into the result of Equation (36) removes the crack length, a, from the expression. Then, G_{Ic} can be calculated using purely the measured load-deflection response, as well as the material properties. It can be shown to be equal to

$$G_{Ic} = \left[\frac{27P^4\Delta^2}{2B^4}\left(\frac{1}{E_1 h_1^3} + \frac{1}{E_2 h_2^3}\right)\right]^{1/3} \tag{37}$$

For the simplified version of the DCB, when $E_1 = E_2 = E$ and $h_1 = h_2 = h$, Equation (27) reduces significantly and it can be shown

$$G_{Ic} = \left[\frac{27P^4\Delta^2}{Eh^3B^4} \right]^{1/3} \tag{38}$$

6.3 Experimental Methods

6.3.1 Materials

The CFRP material as well as the Polymer-based CNT formulation to enhance the baseline CFRP are the same as those listed in Section 3.2.1. This information is not repeated here for succinctness.

6.3.2 Specimen Preparation

Specimens have been prepared to be both balanced and symmetric with respect to the neutral axis. Importance was given to the residual stresses that are present and ensuring that they are balanced out in such a way as to maintain flat specimens with no warping. This is important to maintaining a pure mode I loading with no mode mixity. The specimens were hand layed up after cutting plies using a 4-axis CNC ply cutter, as shown in Figure 33.

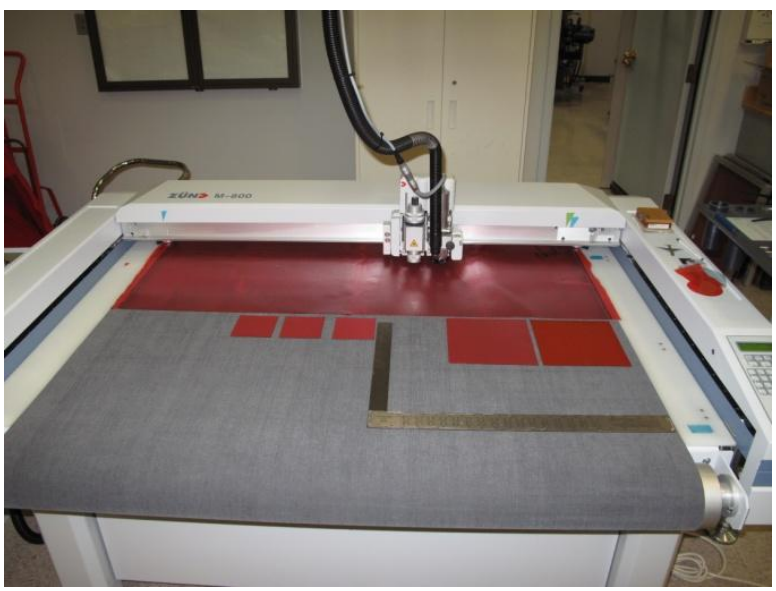

Figure 33 CNC cutting CFRP plies for composite panel lay-up and autoclave curing.

The ply to be used for the mid-thickness plane was electrospun onto with the CNT formulation, as described thoroughly in 3.2.2. The schematic of this depositional process is repeated again in Figure 34 for clarity. This ply was then used with the baseline material plies to create the stack sequence needed for curing and specimen cutting.

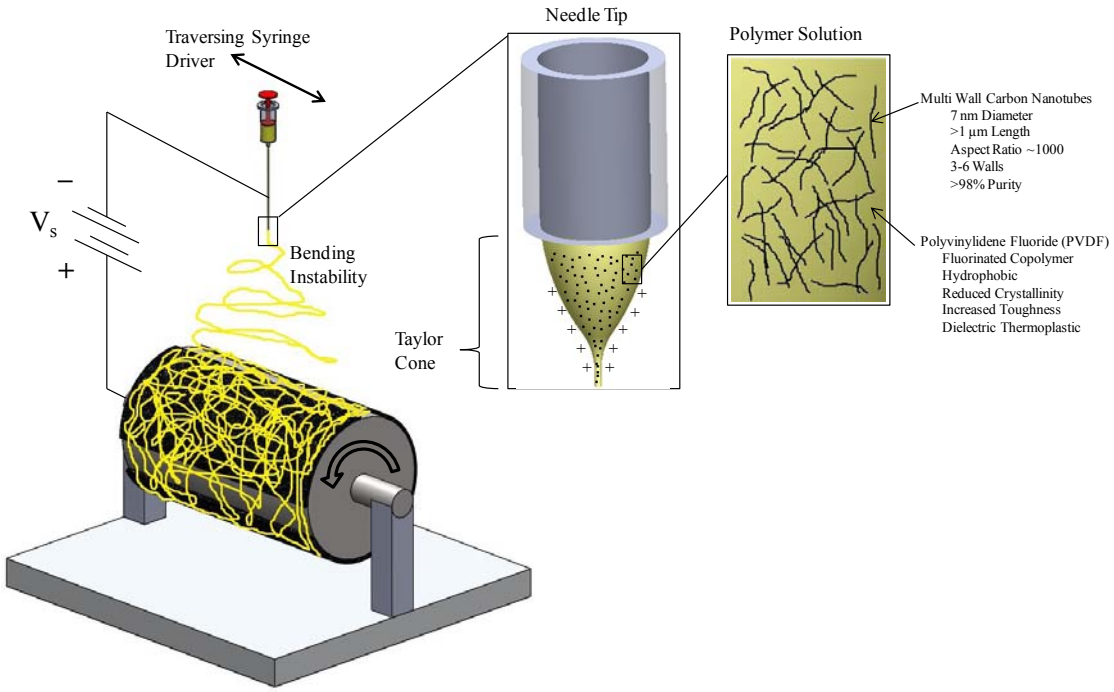

Figure 34 Schematic of electrospinning onto a CFRP ply.

The specimens were layed up to be 16 pli es in thickness with the electrospun interface located at the neutral axis, as shown in Figure 35. The electrospun surface was located on the warp face of the ply, with the intent to fracture colinear with the warp direction. The stack sequence is listed in Table 6 along with relevant geometry of the consolidated panels.

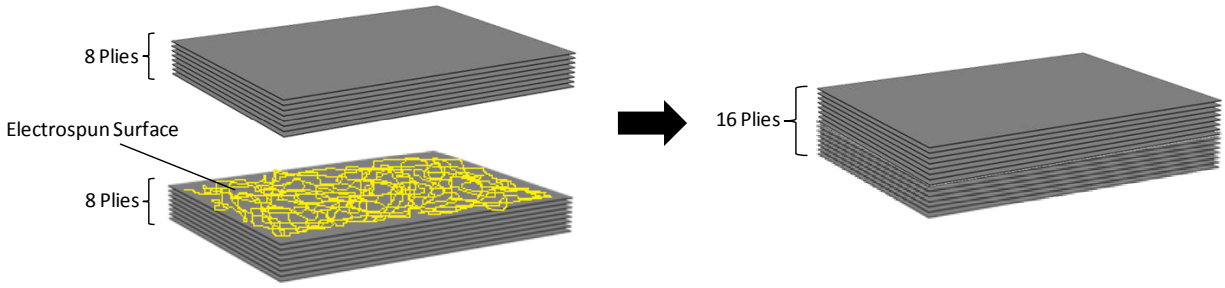

Figure 35 Schematic of the laminate layed up for DCB specimen consolidation.

Table 6 Mode I DCB specimen configuration.

Material	*Baseline CFRP*	*CNT Enhanced CFRP*
Number of Plies	*16*	*16*
Stack Sequence	$[[(0/90)_4]_s]_s$	$[[(0/90)_4]_s]_s$
Thickness (mm)	*6.0*	*6.0*
Width (mm)	*19*	*19*
Length (mm)	*145*	*145*

A 12.7 μm thick Teflon film was applied to the middle of the panels along one end before bonding, as shown in Figure 36. The Teflon was approximately 50 mm in length and spanned the entire width of the panel. This was to inhibit any bonding between the upper and lower halves of the specimen during the cure cycle, acting as a crack starter during testing. It was important to ensure the thickness was minimized as much as possibly so no residual out of plane peeling stress resulting after panel consolidation.

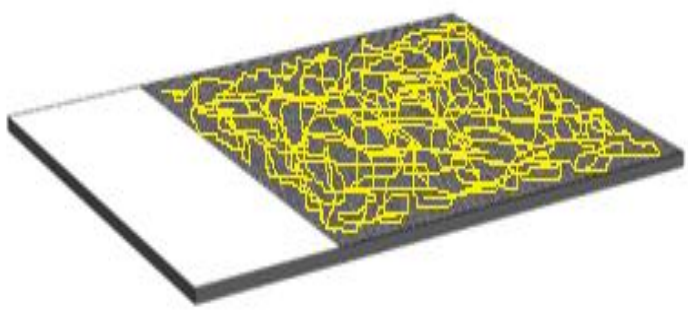

Figure 36 A thin Teflon insert applied to the end of the electrospun lamina.

Panels, after being hand layed up, were vacuum bagged and debulked overnight. Embedded thermocouples were placed in the bag with the panel in order to properly drive the cure cycle based on the actual material temperature, rather than just the air in the autoclave. Panels vacuum bagged and debulking with embedded thermocouples can be seen in Figure 37. Multiple vacuum ports are applied to the panels, one on each opposite corner, to ensure uniform resin bleed and compaction during cure. Panels are then placed in the autoclave for the programmed cure schedule, as shown in Figure 38.

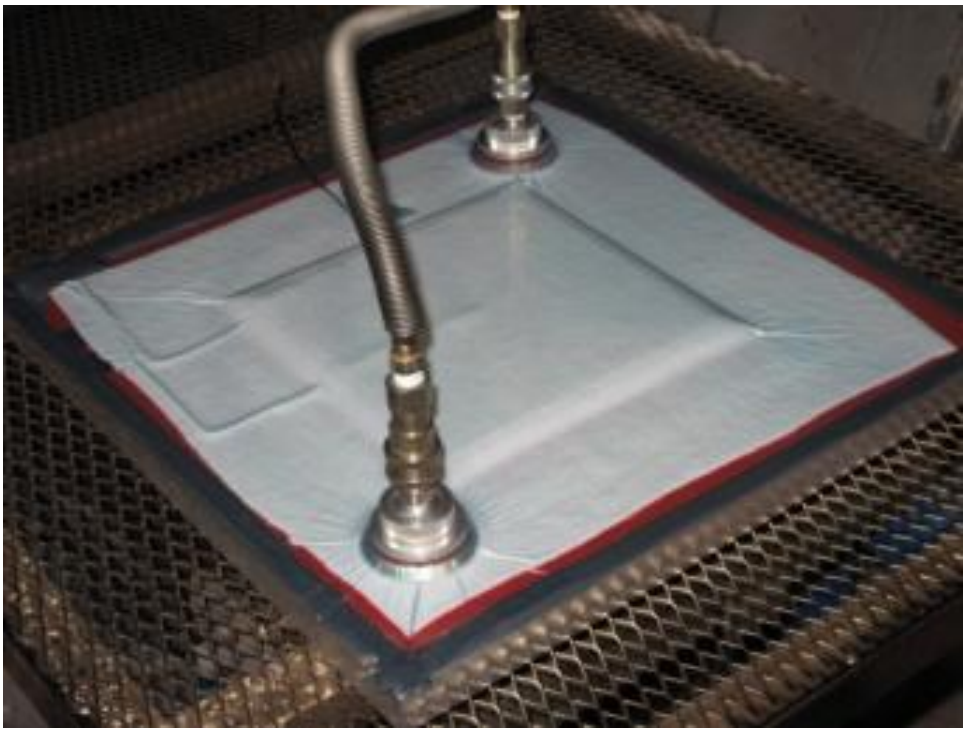

Figure 37 Layed up composite panel under vacuum bag debulking before cure.

Figure 38 Autoclave with CFRP panel to cure on caul plate inside vacuum bag.

The autoclave cure schedule is illustrated in Figure 39, showing the temperature, pressure and vacuum profiles. The debulk operation is performed for at least 30 minutes before the panel is exposed to increasing temperatures. This ensures adequate compaction of the

laminate and the reduction of air pockets induced during the lay-up procedure. The autoclave is initially ramped up in temperature at 5 °F /min while full vacuum is simultaneously applied to the panel. The temperature ramp continues up to 350 °F, with the ramp driven off of the lead thermocouple and the dwell based on the lag thermocouple. This vacuum process with increasing temperature occurs for as long as practically possible to aid in the devolatilization process. The limitation would be the viscosity of the resin system and the gelation point.

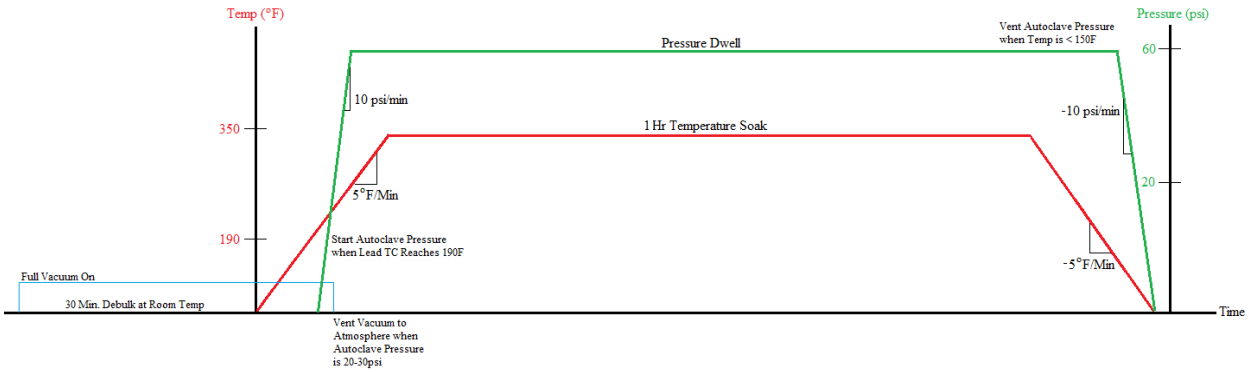

Figure 39 Autoclave cure schedule depicting time, temperature, and pressure relationships for complete consolidation.

As can be seen in Figure 40, the resin viscosity reaches a minimum before rising steeply due to the chemical crosslinking. The period of time before this is used for effective wet out, compaction and degassing. The applied vacuum, along with the increasing temperature, causes gases to expand and mobilize out of the laminate. As viscosity is dropping, this devolatilization process is aided. Once 190 °F is attained, the autoclave pressure is applied at 10 psi/min up to 60 psi. The vacuum is vented once the autoclave pressure exceeds that of atmospheric pressure, which is done at approximately 20 psi. The pressure and temperature continue to ramp up to 60 psi and 350 °F, respectively. The temperature then dwells for approximately 1 hour with full pressure applied. The cure is then complete and temperature and pressure are slowly removed at controlled rates to reduce the effects of thermal residual stress. Panels can be removed once temperature is approximately 150 °F.

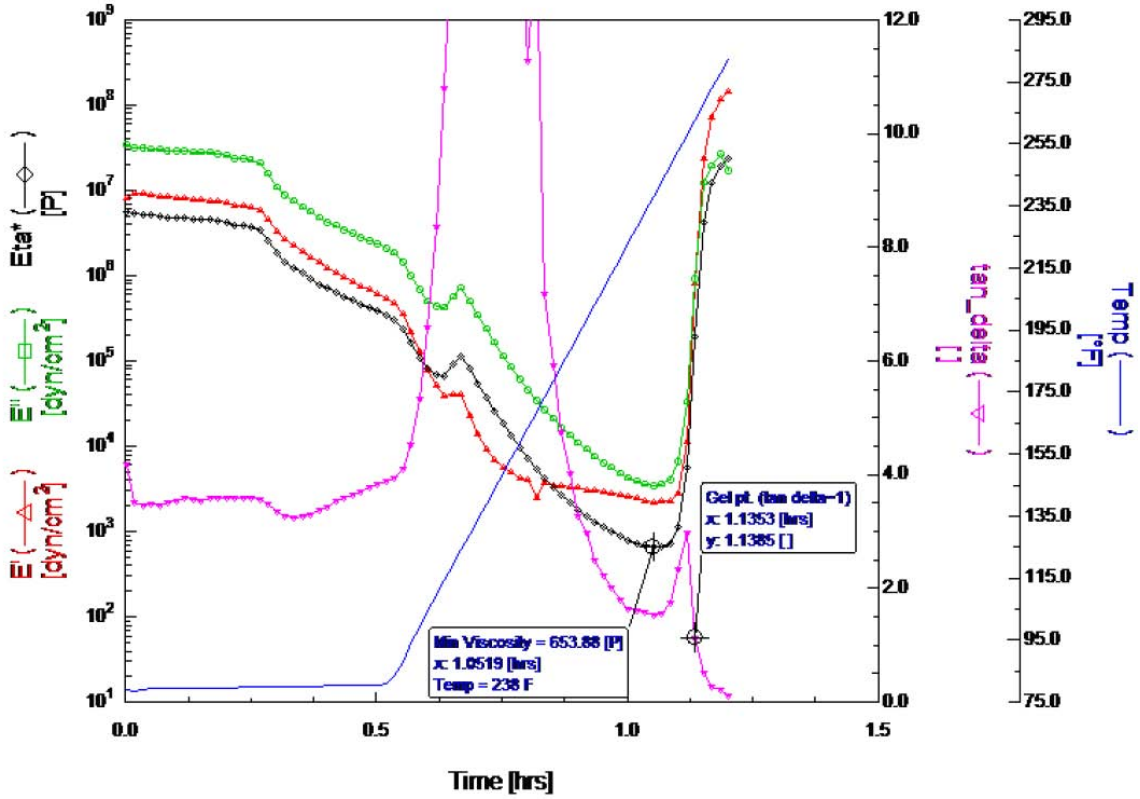

Figure 40 Rheology curve for the 3362 resin system utilized with the carbon fiber.

Cured panels were then measured and scribed for datum reference marks to aid in the cutting of specimens, as shown in Figure 41. Cutting was performed using a wet diamond saw to get to final specimen geometry, as previously listed in Table 6. Specimen edge average roughness was measured to be approximately 2-6 µm using vertical scanning interferometry.

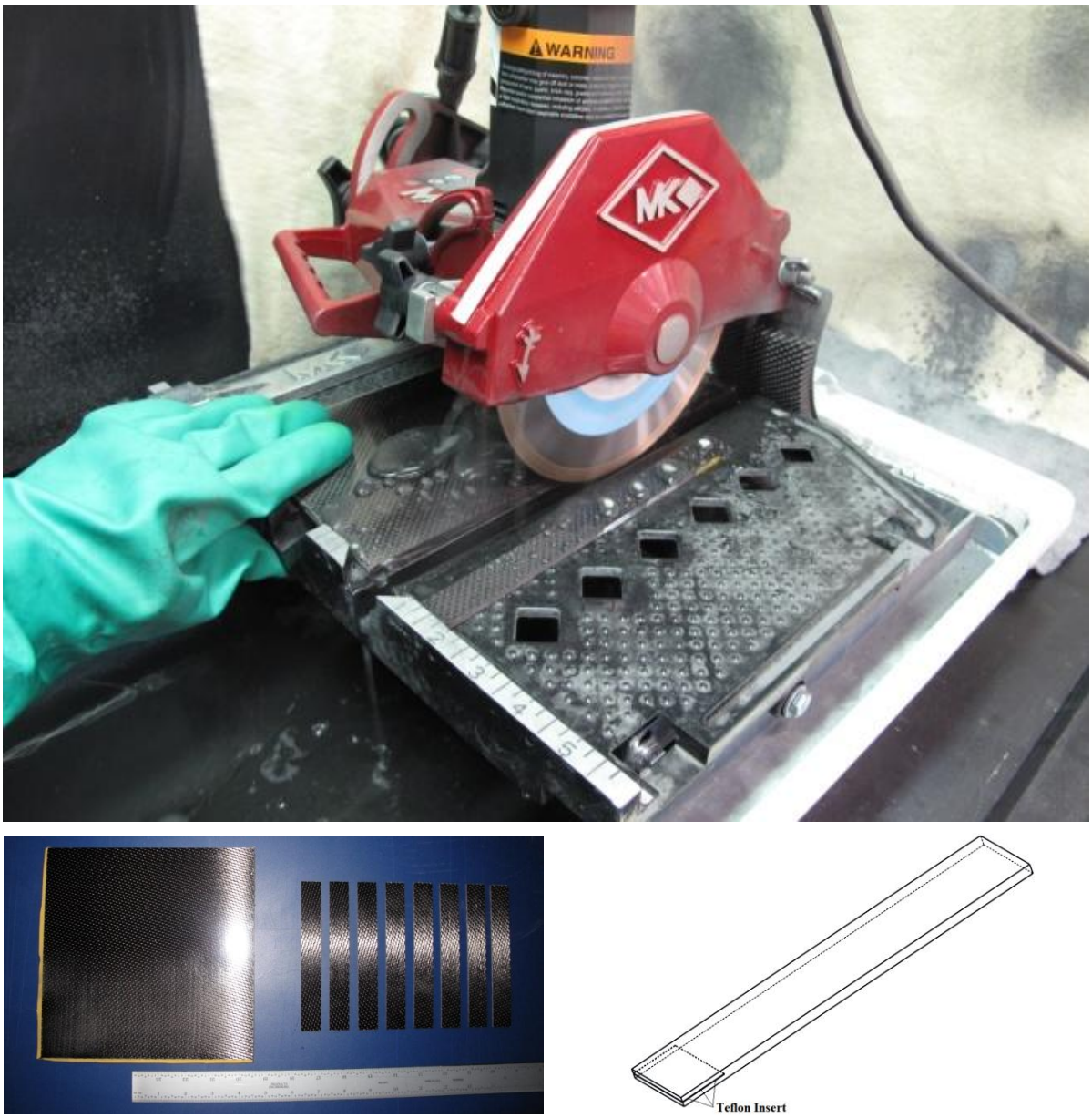

Figure 41 Wet diamond saw cutting specimens from consolidated panels.

Individual specimens were then equipped with steel hinges, as shown in Figure 42. The steel hinges were cut from larger piano hinges in order to ensure symmetry of loading based on hinge length and flap width. A quick setting, high strength epoxy was mixed and used to bond hinges to the specimen while specimens were aligned in the load frame using fixturing to keep hinges parallel. Once specimens were hinged and ready for testing, a scale was put on each specimen, starting from the tip of the Teflon insert out to 100 mm in length. This allowed each specimen to be monitored for crack growth during the experiment. The

graduations of the scale were every 1 mm for the first 10 mm, then every 5 mm thereafter out to 100 mm.

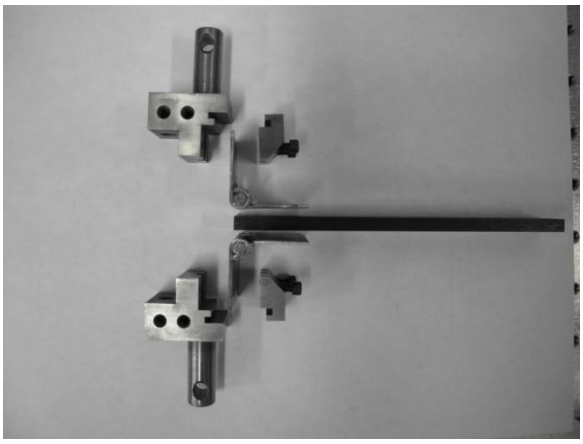

Before bonding tabs and fixturing

Alignment procedure for fixture

Figure 42 Bonding hinges to specimens and aligning loading fixture for attaching the hinged specimen to the load frame

6.3.3 Testing Procedure

Specimens were fixture using a stainless steel, double bolted adjustable clamp as shown in Figure 43. As previously mentioned, the specimens were bonded to hinges while the hinges were mounted to the fixture to ensure no torsion or bending was induced on the specimen during mounting. The double cantilever beam specimens were loaded in displacement control at 1 mm/min using the crosshead displacement. This very low rate of displacement control was employed to reduce the potential for strain rate dependency within the polymeric material. Data was recorded at 10 Hz in real time using Instron‘s BlueHill software suite. Load, displacement, and time were continually recorded for the entire event until stopped by a 100 % load drop or operator suspended test.

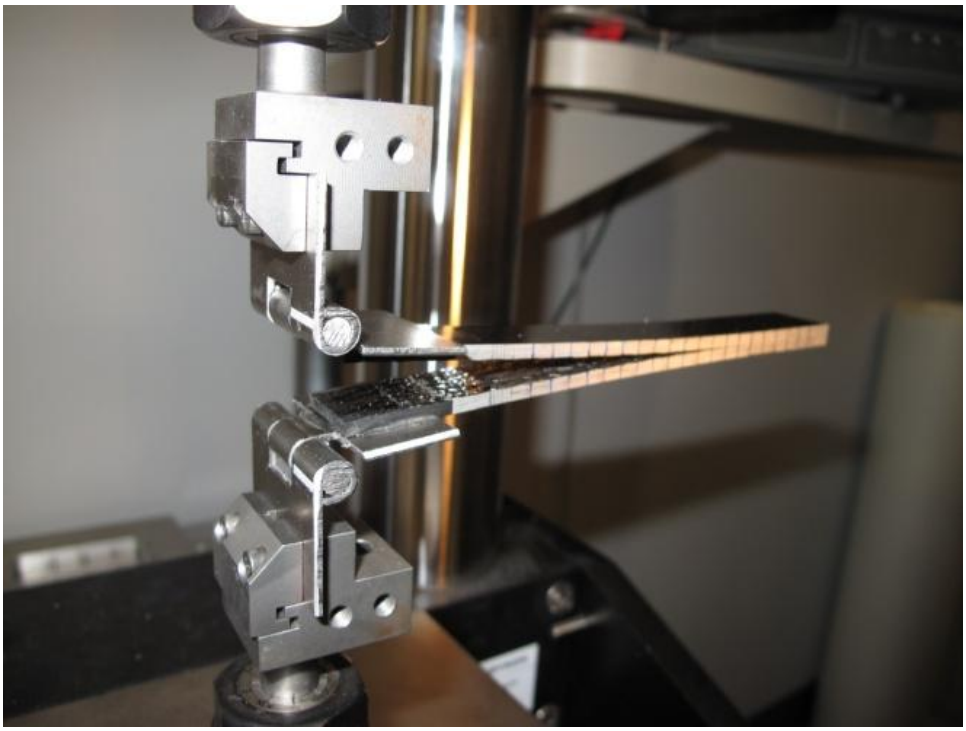

Figure 43 DCB specimen fixturing, aligning, and testing.

The test set-up consisted of 2 traveling microscopes, 3 computers, a laser extensometer, and the Instron Model 5848 micro-tester load frame equipped with a 2 kN load cell (0.0001 N resolution). The experimental stage and instrumentation can be seen in Figure 44 and Figure 45.

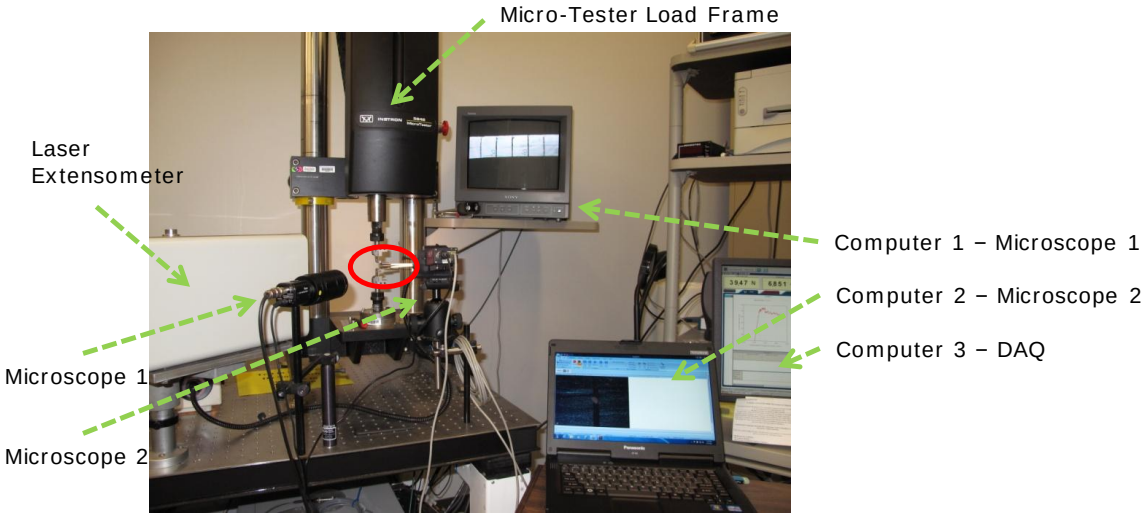

Figure 44 Test setup for double cantilever beam Mode I fracture experiments.

The crack tip opening displacement (CTOD) was directly measured with a laser extensometer and the crosshead encoder simultaneously. After preliminary experiments to verify method and fixturing, it was determined that the error between the crosshead displacement and the reading from the laser extensometer was negligible. This allowed either one to be used for post processing reduction of data.

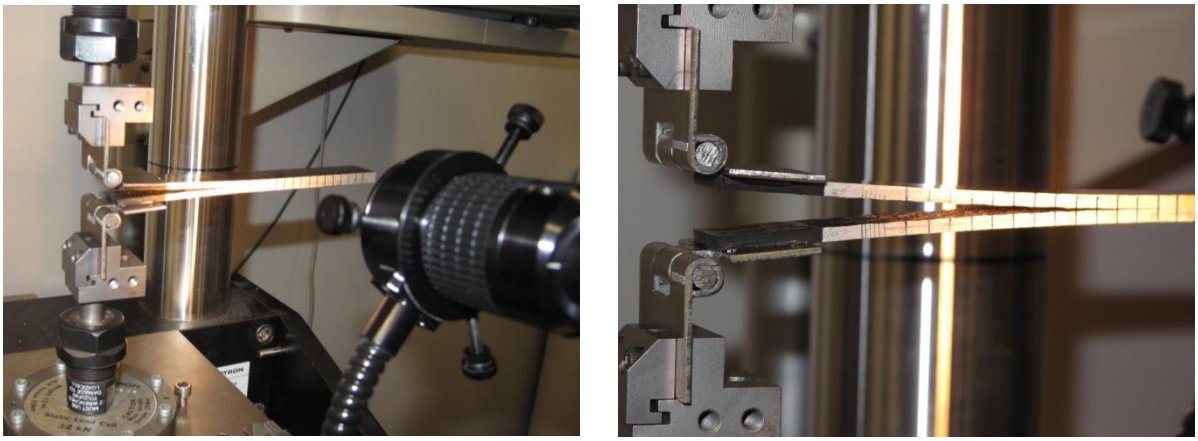

Figure 45 Travelling microscope for in-situ crack growth determination.

6.4 Results and Discussion

6.4.1 Load and Displacement versus Time Response

The loading of the DCB specimens was controlled by the crosshead displacement rate. The rate was linear at 1.0 mm/min and the specimen responded accordingly, as can be seen in Figure 46 and Figure 47 for the baseline CFRP and CNT modified CFRP, respectively. The response is governed by a linear increase of load resistance versus time up to some instability load. At this bifurcating load value, the load suddenly drops indicating the first fracture growth event stemming from the Teflon starter flaw. The fracture then continues to grow and arrest as time passes, which is observed as the load drops and rises, respectively.

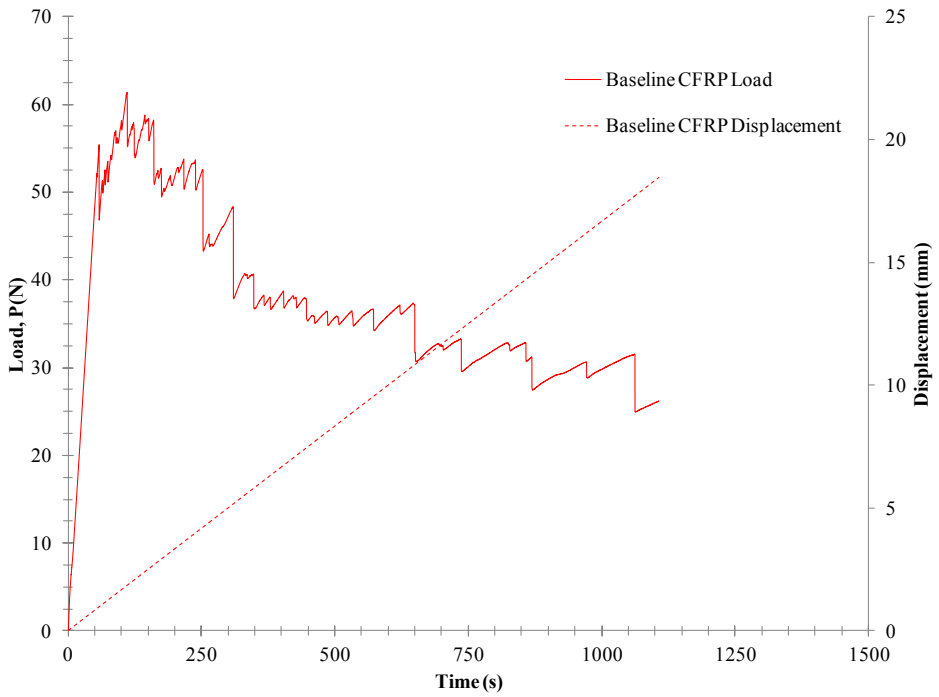

Figure 46 Load and displacement versus time response for the baseline CFRP.

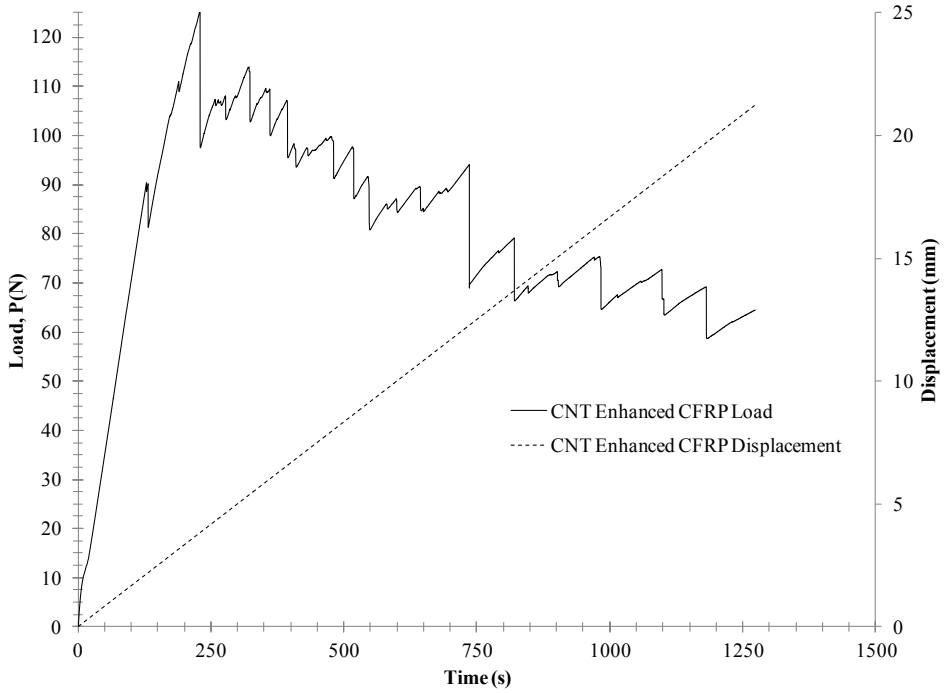

Figure 47 Load and displacement versus time response for the CNT enhanced CFRP.

6.4.2 Load versus Displacement Response

In order to visualize the data in a more useful manner, to either quantify energy or structural compliance, the load data is superposed with the deflection data, both being directly measured independently of one another. As can be seen in Figure 48 and Figure 49, the load-displacement response is qualitatively similar to the load-time responses shown previously, as expected. This is due to the fact that the displacement is linearly controlled at a constant rate.

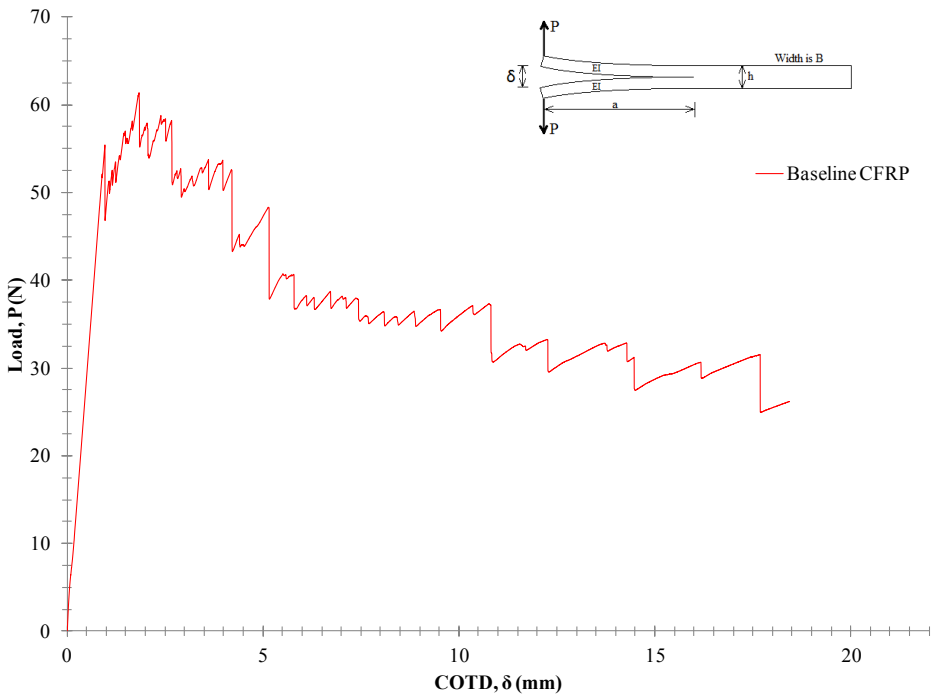

Figure 48 Baseline CFRP load versus crack tip opening displacement.

From these plots of load-displacement, the cumulative energy absorbed and compliance of the system can now be determined for each of the response curves. This will allow the determination of the critical strain energy release rate using any of the methods described in 6.2.

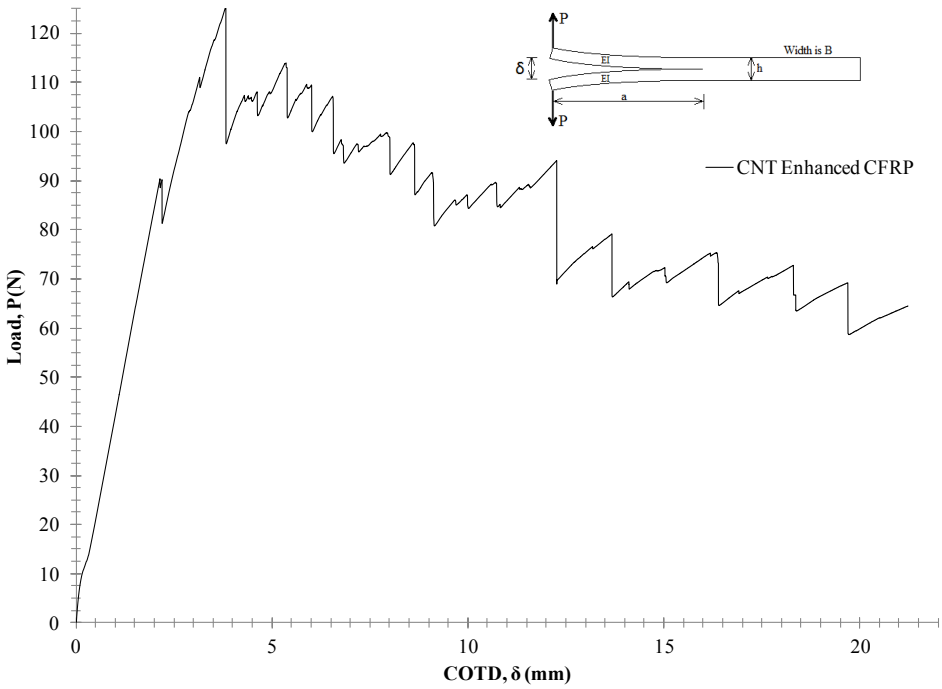

Figure 49 CNT enhanced CFRP load versus crack tip opening displacement.

To compare the response curves between the baseline CFRP and CNT modified CFRP, superposition of the data has been performed, as can be seen in Figure 50. From this plot, it is quite apparent that the CNT enhancement has a rather discernable effect. To start, it should be noted that the response curves are all representative of similar crack growth extents. This implies the cracks were all allowed to grow approximately 95 mm from the start crack.

The peak load achieved for the CNT enhanced CFRP is approximately 100 % higher than the baseline CFRP with an associated displacement at the crack tip that is approximately 2.5 times larger. The initial responses are similar in terms of mechanical stiffness, though the CNT modified specimens all experience a _pop-in‘ effect around 65 % of the peak load. This is thought to be the effect of the crack first advancing from the Teflon insert, a region that is likely resin rich due to the consolidation process. This phenomenon is absent in the baseline CFRP materials. The stepwise behavior as the specimen is loaded is indicative of crack spurting behavior with both the baseline CFRP and CNT enhanced specimens experiencing load drops on the order of 25 -30 %. This type of rapid growth process makes it difficult to accurately track the fracture growth extent and to determine in-situ measurements with the traveling microscope.

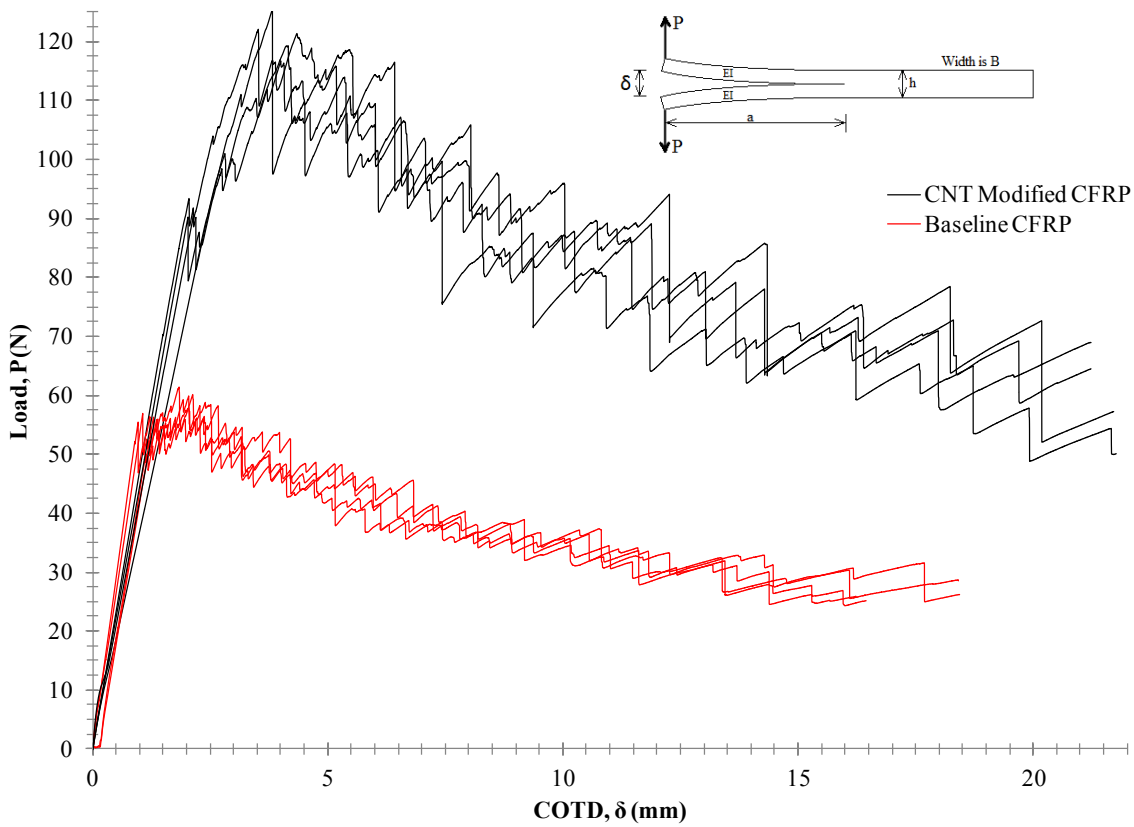

Figure 50 Comparison of load versus crack tip opening displacement response between baseline CFRP and CNT modified CFRP.

6.4.3 Crack Growth Behavior

Significant differences were observed in the crack growth behavior for the baseline CFRP versus the CNT enhanced system. These differences gave rise to the variation in the measured mechanical response. In addition, they posed significant challenges for the direct measurement of the in-situ crack growth measurements.

As can be seen in Figure 51, the baseline CFRP material is well behaved with a sharp crack tip. The fracture path remains coplanar with the intended, mid-thickness interface. Any vertical shift in the fracture path remained along the correct interface and was solely attributed to the architecture of the weave. To contrast this, the fracture behavior of the CNT enhanced system can be seen in Figure 52. For this modified material system, the crack front consisted of two competing advances. The intended fracture path, along the mid-thickness plane, in addition to a secondary fracture development and propagation, continued along the

entire length of the specimen. These two competing advances alternating their growth spurts and, when the COTD became large enough, began inducing flexure in the secondary ply. For both the baseline CFRP and the CNT enhanced systems, a large amount of fiber bridging was observed.

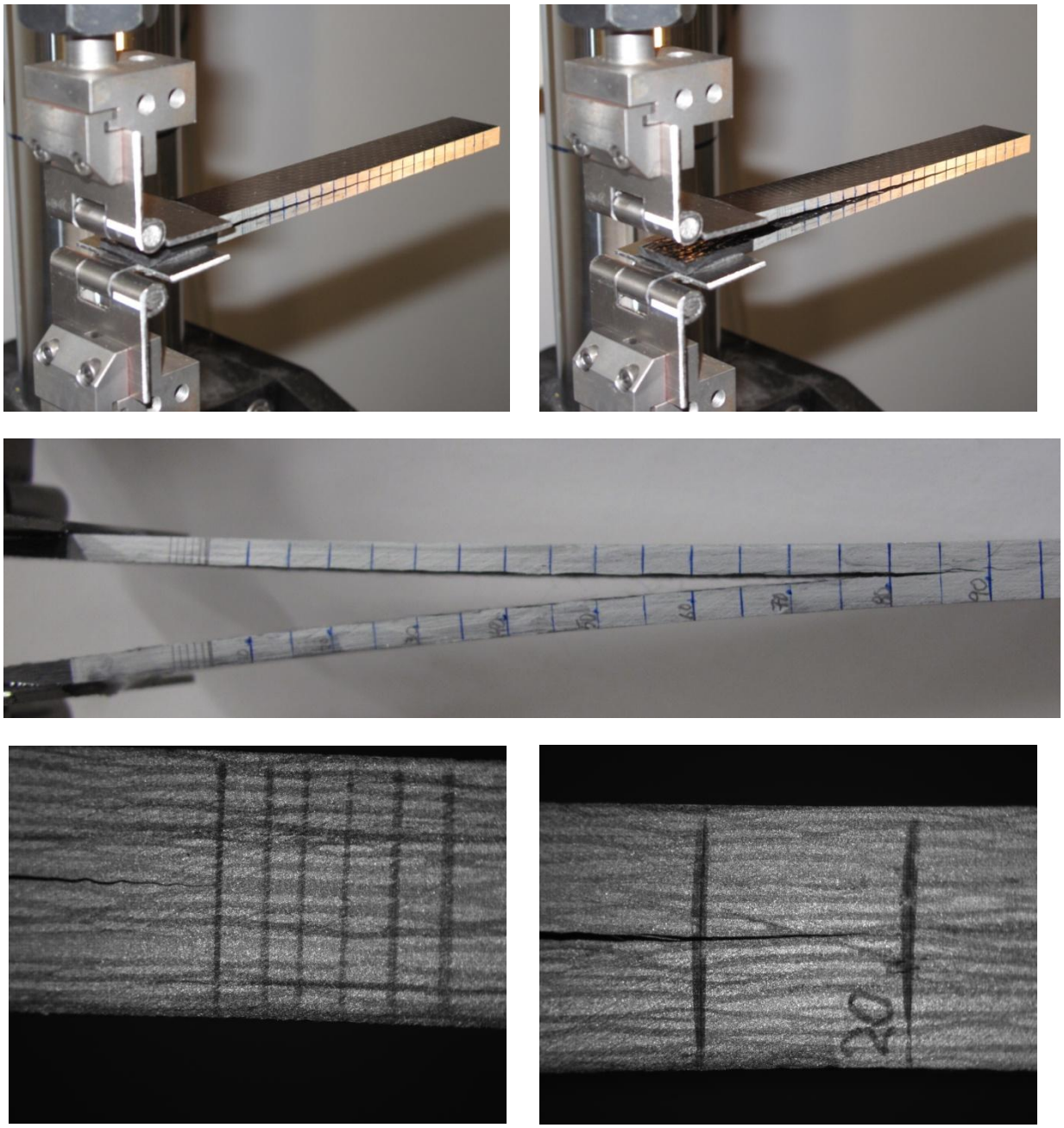

Figure 51 Mode I fracture behavior for baseline CFRP.

As a result of the complexities associated with the fracture growth behavior in the CNT modified CFRP, the crack lengths were not able to be in-situ measured as they were for the baseline CFRP. Instead, the load and deflection was continuously measured and used with the beam theory development to determine the strain energy release rate. This methodology for determining the critical *G* proved to be invaluable in this present investigation due to the multiple crack fronts. Whether the value obtained is relevant in terms of intrinsic material properties for fracture onset and growth is a topic of debate.

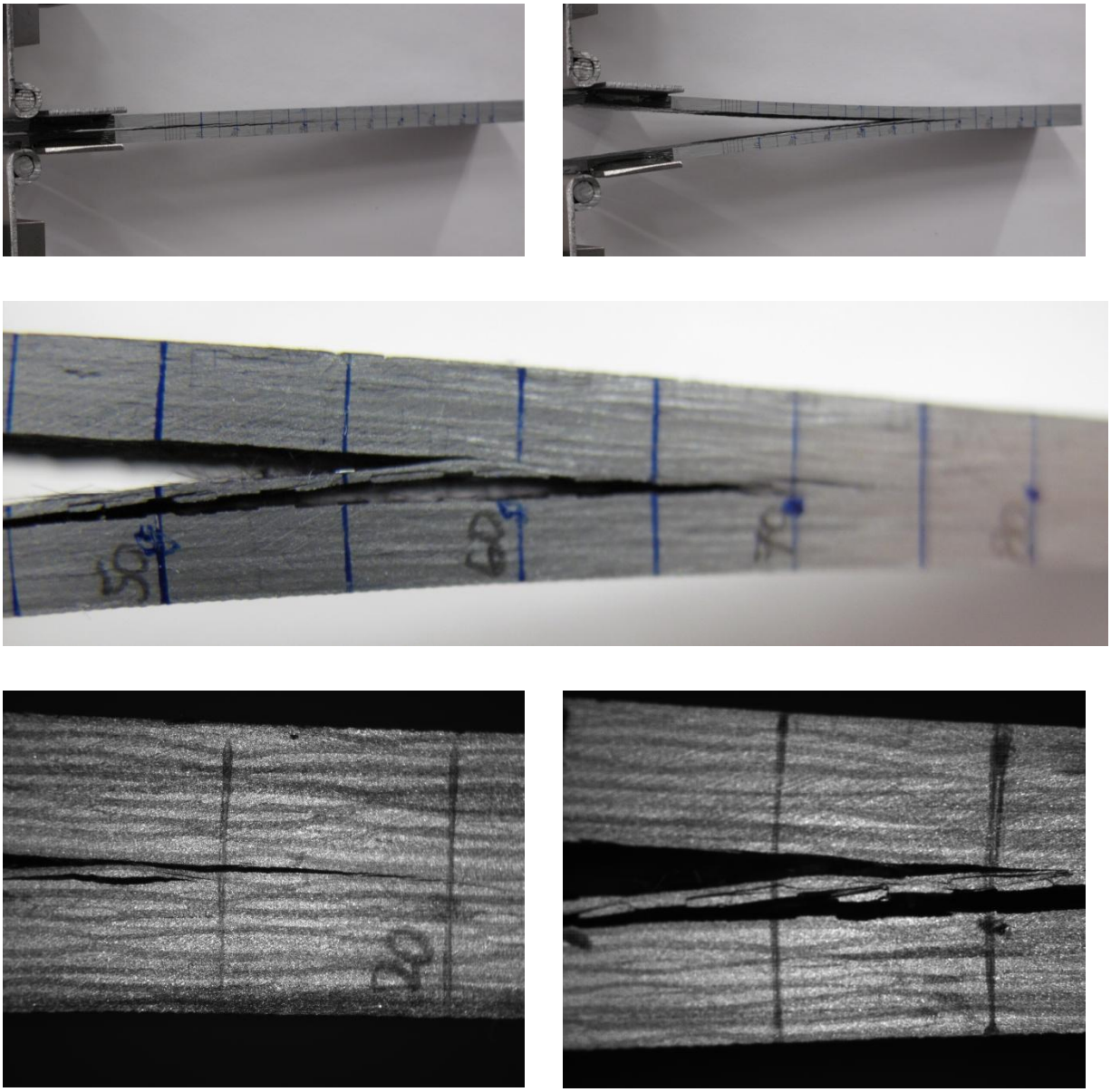

Figure 52 Mode I fracture behavior for CNT enhanced CFRP.

6.4.4 Energy Absorption

One method of visualizing the experimental data is to integrate the load versus deflection response in order to determine the work done on the specimen. This work done, with an elastic unloading, can be visualized as the shaded region in Figure 53. With the elastic unload, the shaded region represents the energy associated with the damage induced to the respective materials. This damage extent represents how much energy is absorbed during the process of creating new surfaces, fracturing fibers, etc.

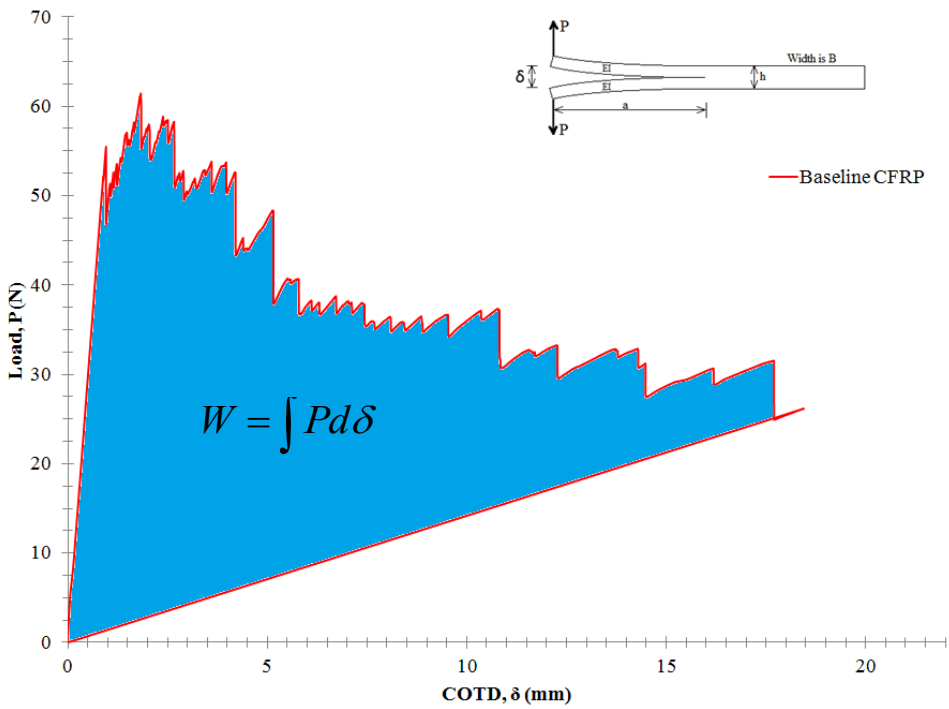

Figure 53 Illustration of total energy absorbed during fracture process.

When performing the integration for each respective double cantilever beam experiment, the plots of Figure 54 can be created. These plots illustrate that the energy absorption process is generally increasing at a decreasing rate, after the inflection associated with the peak load value. The plots do not take into account any elastic recovery, they only contain to total summation of the work done to open the specimens to their respective COTDs. After approximately 1.5 mm of total displacement, the energy absorption for the two sets of materials diverges considerably. For a given displacement of 15 mm of COTD, for instance, the total absorbed energy is more than double for the CNT modified samples versus the

baseline CFRP. Qualitatively, however, the responses are similar and quite repeatable amongst similar samples.

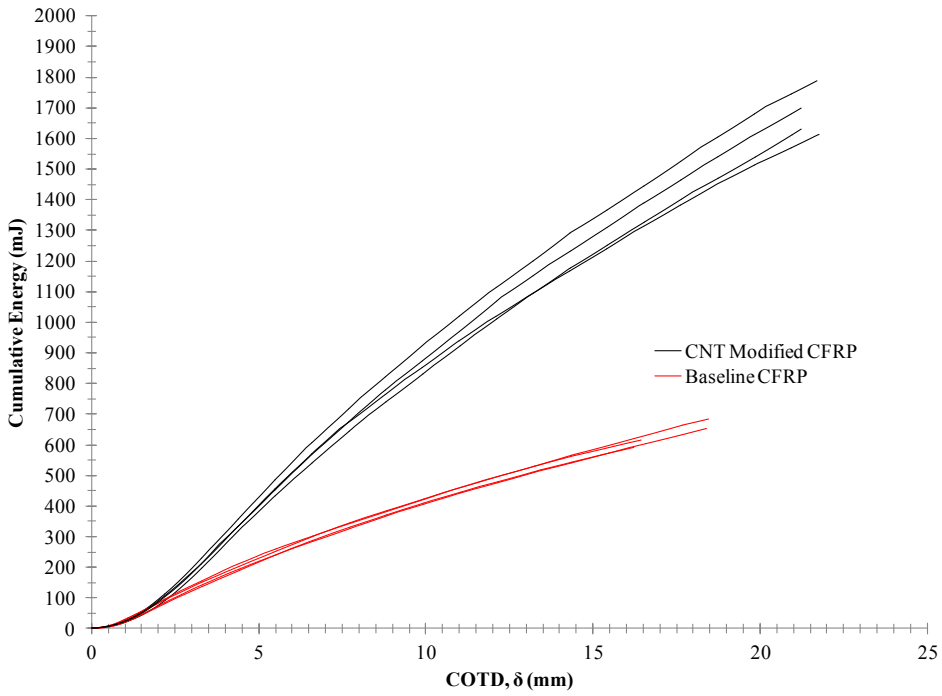

Figure 54 Cumulative energy absorption for the baseline and CNT enhanced CFRP.

6.4.5 Critical Mode I Strain Energy Release Rate

As can be seen in the methodologies developed in 6.2, all of the methods, with the exception of the Area Method, rely on the mechanical compliance of the system. They all are based on linear elastic fracture mechanics (LEFM) in their development. The strain energy release rate can be shown to be equal to the expression given in Equation (22) for either a load or displacement controlled experiment. To outline the procedure of analysis employed for the specimens, the compliance is first calculated and plotted with respect to the crack lengths determined in-situ. A typical relationship for the baseline CFRP can be seen in the plot of Figure 55. This plot is then fitted using the method of least squares with an appropriate curve. For this response, a third order polynomial expression was utilized. The order of the polynomial, and the family of curve employed, will have an effect on how the derivative behaves. A sensitivity analysis was first performed using several approaches and the polynomial family worked well within the domain of consideration.

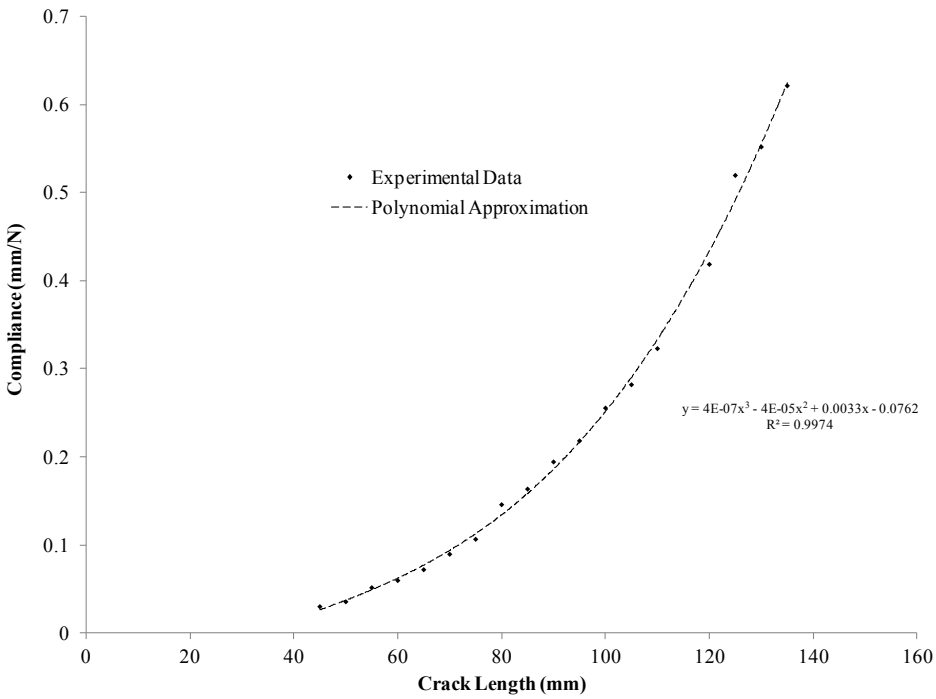

Figure 55 Typical compliance response with polynomial approximation curve fit.

The derivative with respect to the crack length can then be calculated for the baseline CFRP materials. The critical strain energy release rates, with the derivative determined at each location of interest, can be calculated using material properties, applied load, associated displacement, and geometry. Note the beam theory method is the one method that was developed in such a way as to eliminate the crack length from the expression. Hence, the beam theory method does not need the compliance curve for evaluation. It simply utilizes the respective load and displacement response along with geometry and material properties. The resulting plot shown in Figure 56 contrasts each of the methodologies outlined in 6.2 as a function of the fracture length. They all agree well with each other and, globally, increase at a decreasing rate to a converged value, as would be expected. The plot of Figure 57 characterizes the critical strain energy release rate as a function of the COTD.

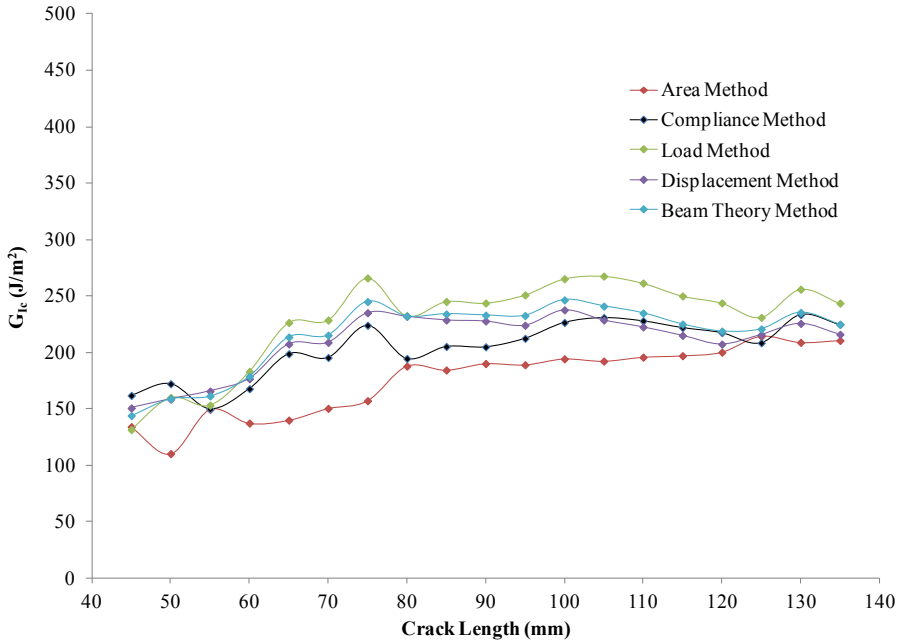

Figure 56 Resulting critical strain energy release rate versus the crack length using all of the various methodologies developed.

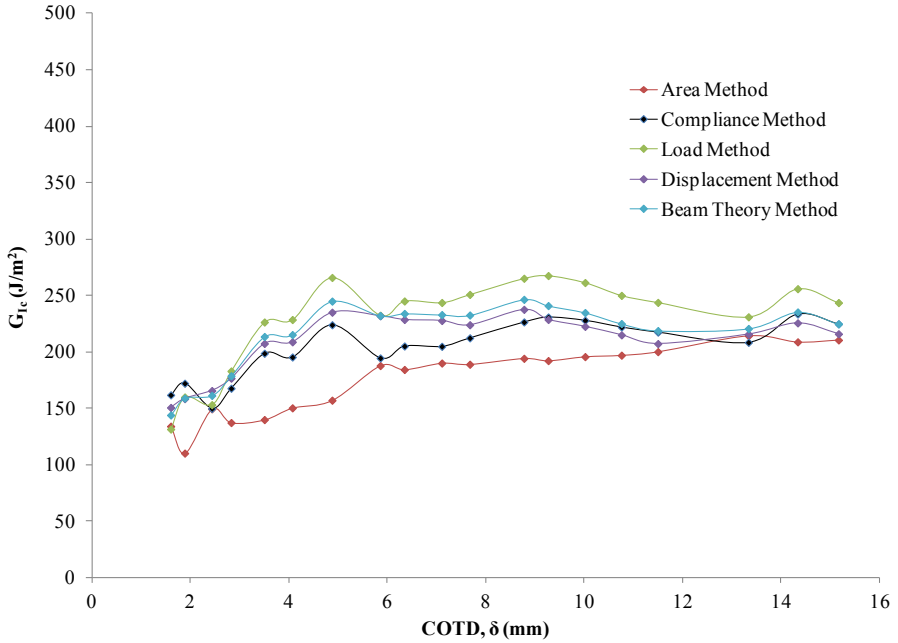

Figure 57 Resulting critical strain energy release rate versus the COTD using all of the various methodologies developed.

To relate the crack opening tip displacement to the crack length, the plot of Figure 58 was determined. This reveals a non-linear relationship between the two values which increases at a decreasing rate. More data for shorter crack lengths would have extrapolated this plot through the origin.

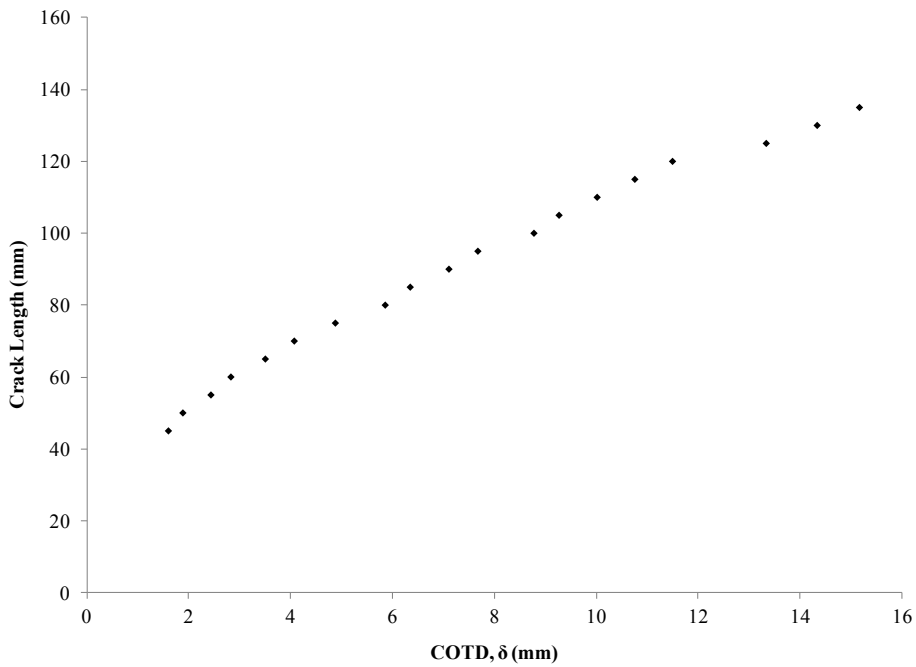

Figure 58 Relationship between the crack length and the associated COTD.

To have a consistent framework for comparison sake, the elasticity theory development shown in 6.2.5 has been employed for both the baseline and CNT enhanced material systems. This approach allowed the determination for the critical strain energy release rate to be plotted as a function of the COTD. The plots of Figure 59 and Figure 60 illustrate the approach for the baseline and CNT modified systems, respectively. These plots illustrate some of the difficulties associated with the determination of G_{Ic} for a material response with oscillatory load deflection behavior and growth spu8rt behavior. If the material had responded with a more consistent crack growth tearing behavior the response would be much flatter and smoothened out. To account for this, and for clarity in the visualization for comparison purposes, a logarithmic approximation was determined using a least squares method to replace the data curves. This was employed for each specimen.

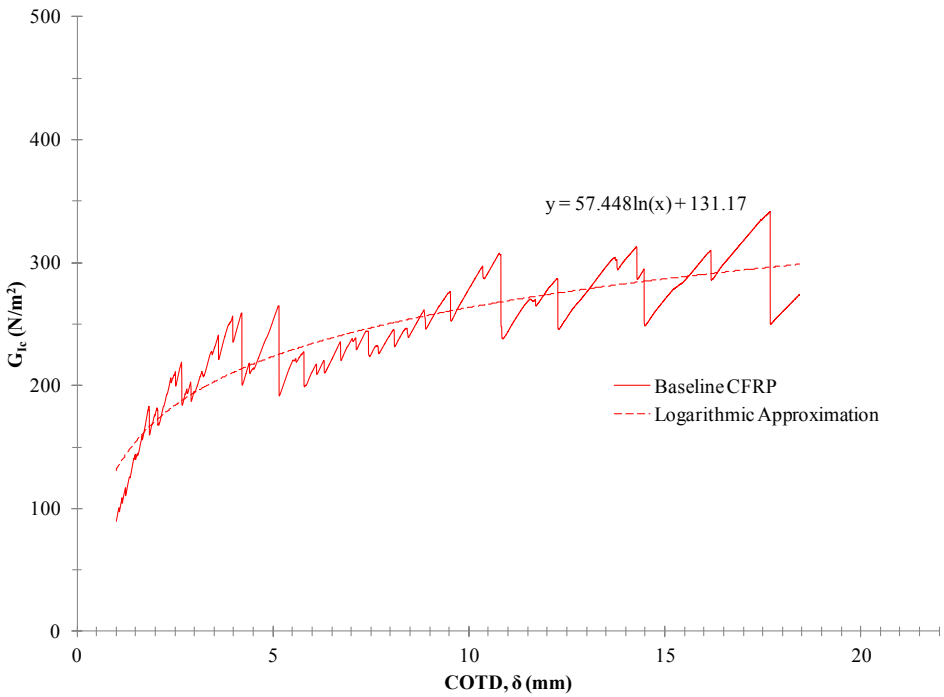

Figure 59 Elasticity theory approach to determining the critical strain energy release rate for the baseline CFRP material system with logarithmic approximation.

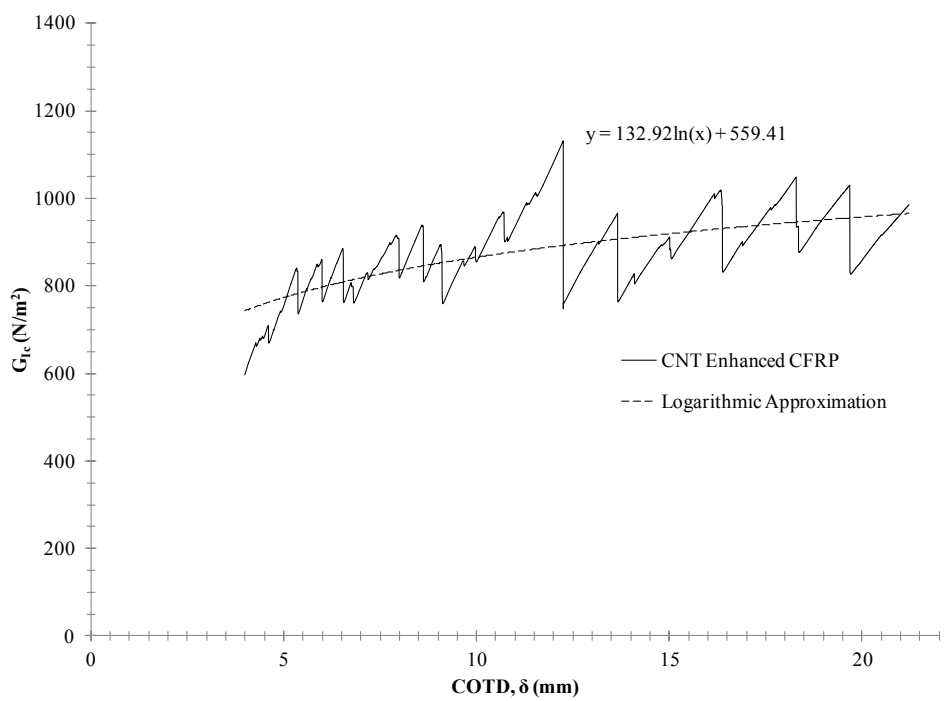

Figure 60 Elasticity theory approach to determining the critical strain energy release rate for the CNT enhanced CFRP material system with logarithmic approximation.

Using the elasticity approach, the baseline and CFRP material systems have all been calculated as a function of the COTD and plotted in Figure 61. These plots shown here are representative of an idealized single crack growing along the mid-thickness plane using the experimental data. The baseline material can be seen to have a critical strain energy release rate between approximately 225 N/m^2 to 275 N/m^2 from the initial growth to the final, converged value. The CNT modified material varies from the initial fracture growth at 750 N/m^2 to a converged value of approximately 900 N/m^2. The initial onset values for the CNT modified CFRP are approximately 233 % higher than the baseline CFRP material system. The converged value at larger COTDs for each system reveals an approximate 227% increase for the CNT modified system. This is a significant increase, but the multiple crack planes developed in the CNT modified specimen are a considerable source of energy absorption.

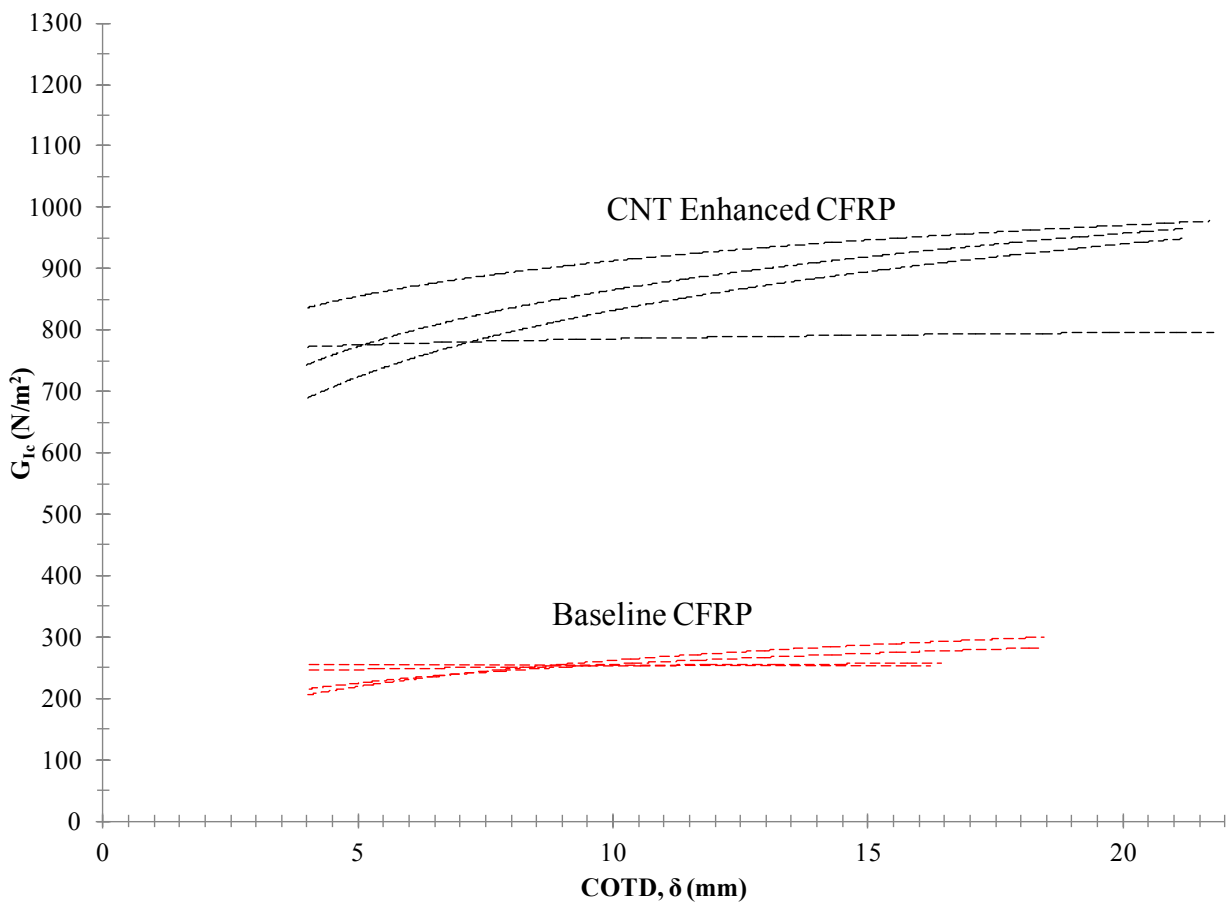

Figure 61 Resulting critical strain energy release rates for both the baseline CFRP and CNT enhanced CFRP material systems as a function of the COTD.

6.4.6 Fractography

To investigate the fracture surface morphology, a scanning electron microscope (SEM) was used on carefully sectioned samples after fracture testing. The variations in the critical strain energy release rate are fundamentally associated with the nature of the fracture behavior and the type and amount of atomistic bonds broken. From the fractography images shown in Figure 62, significant differences are apparent in the respective fracture behavior and topology.

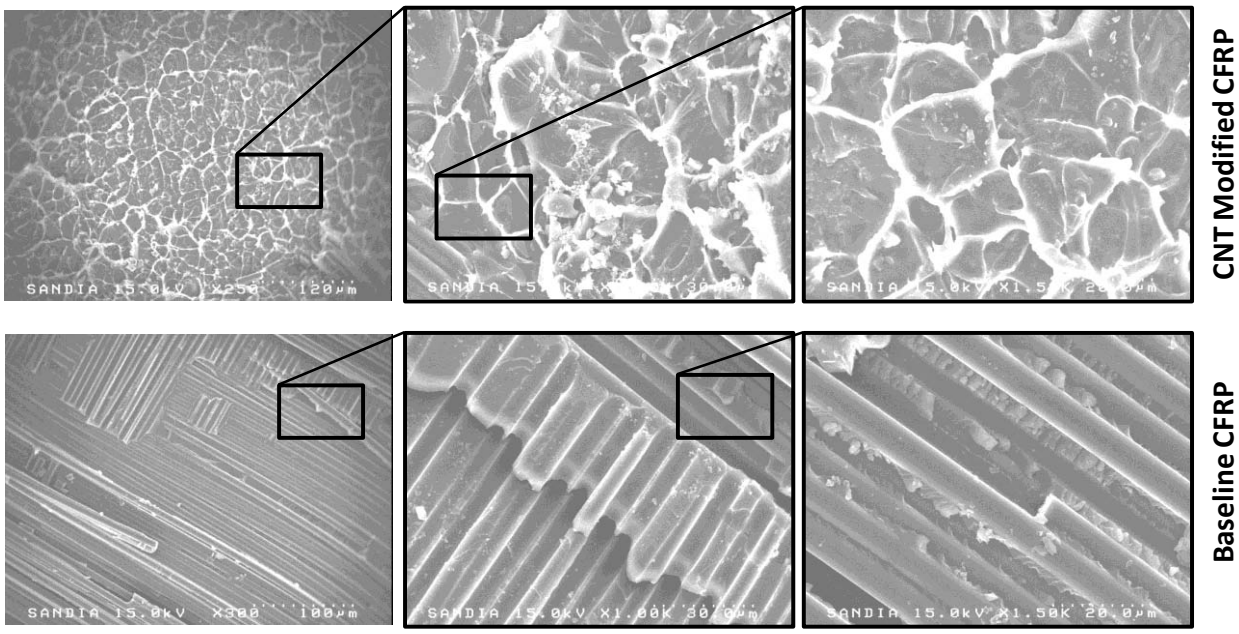

Figure 62 SEM fractography images showing the variation in crack behavior for CNT enhanced CFRP (above) and baseline CFRP specimens (below) under Mode I fracture.

The baseline CFRP fracture surfaces can be seen to be smooth with small amounts of cohesive fracture through the thermosetting epoxy resin. There are regions of hackly formation in between fibers that is evident, but the fracture is primarily governed by interfacial adhesion fracture between the fibers and the resin. Many regions were observed on the baseline CFRP fractured surfaces where the fibers were cleanly removed from the resin with no considerable crazing or shear yielding. Although the surface area created is large when considering the corrugated nature of the topology, as shown clearly in Figure 63, the bond energy associated with the fiber to resin interface is low in terms of energy absorption.

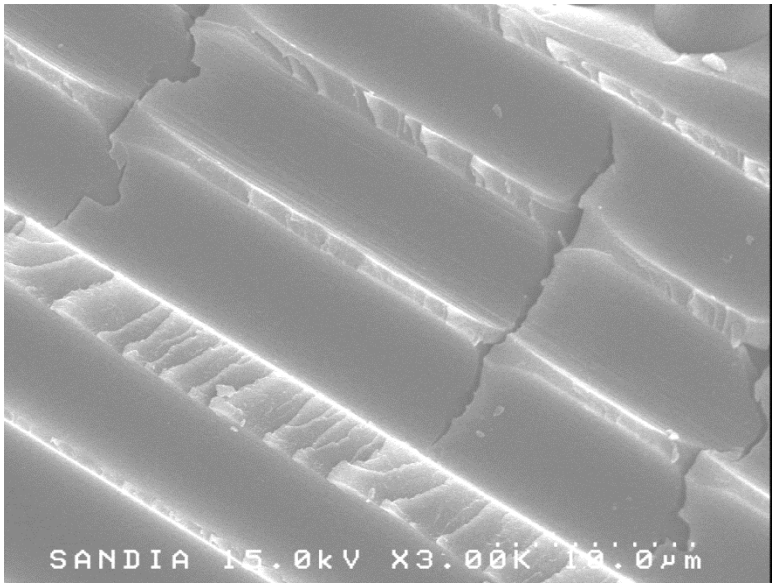

Figure 63 Baseline CFRP fracture surface showing corrugated topology with resin hackle formation between fiber locations.

The CNT modified CFRP fracture surfaces shown in Figure 62 are very unique and different from the baseline CFRP. The surfaces are highly three-dimensional in nature with many regions of both brittle and ductile fracture. The smooth surfaces are likely associated with brittle, cohesive fracture through the CNT doped polymer, somewhat conchoidal in nature. There are also regions that appear to have gone through significant permanent deformation, which would result in significant amounts of energy absorption during fracture. An SEM showing the complex fracture surface associated with the CNT enhanced CFRP material system can be seen in Figure 64. CNTs stemming from the surface are difficult to observe due to the lack of contrast, however a few regions have been identified with CNTs charging during SEM as shown in Figure 65. The CNTs likely absorb a considerable amount of energy through fracture and pullout processes.

The PVDF polymer was likely in its β phase after the elctrospinning due to the alignment of the beta crystallites. This phenomenon occurs when the material is mechanically drawn or when a strong electrostatic potential is applied, both of which occurred during the electrospinning deposition. As a result of t he material undergoing a high temperature and pressure autoclave cure cycle after this deposition, it is likely that the polymer went through a

polymorphic phase transformation during the melting into the more ductile α phase of PVDF. This alpha phase has increased toughness and mechanical energy absorbing ability.

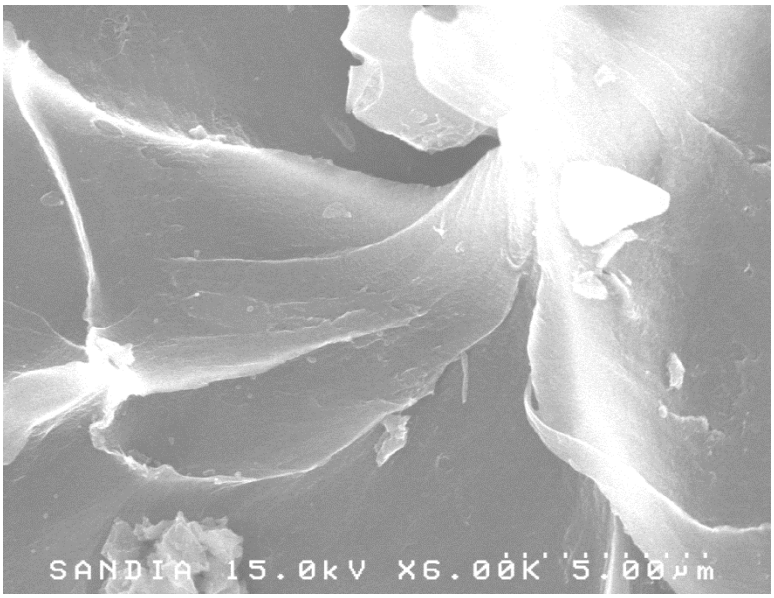

Figure 64 CNT modified CFRP fracture surface.

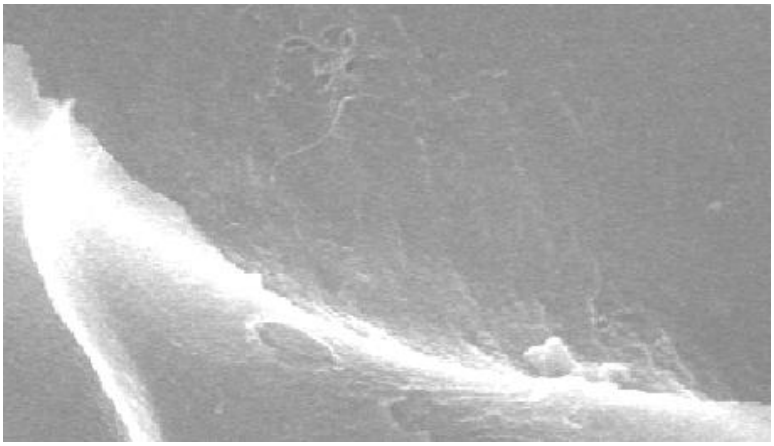

Figure 65 CNTs visible emerging from the fracture surface (image size is approximately 7 µm wide by 4 µm tall).

6.5 Conclusions

A series of double cantilever beam fracture experiments have been performed on the baseline CFRP and CNT modified CFRP material systems. The critical strain energy release rate

under Mode I loading conditions has been calculated, and resulting fracture morphology has been investigated for each material system. The following conclusions can be made:

- The load versus COTD behavior for the baseline CFRP material system is linear until the onset of fracture growth. The fracture precipitation and growth behavior is well behaved, propagating along the intended plane. The growth behavior exhibits successive load drops on the order of 25 % before arresting and elastically reloading.

- The CNT modified CFRP material system exhibits an initial pop-in phenomenon at approximately 65 % of the peak load. The fracture growth behavior is very complex and fractures along multiple crack planes in a somewhat competing effect. The propagation-arrest-elastically reload successive process resulted in approximately 30 % load drops.

- The critical Mode I strain energy release rate has been determined using a variety of methodologies. The CNT modified CFRP material system has been calculated as having an approximate 230 % increase in the G_{Ic} value, though the crack length could not be in-situ measured as a result of the multiple fronts. This value calculated assumes one crack plane and because of the multiple crack planes developed energy was imparted to their development as well.

- The resulting fractography for the baseline CFRP material revealed weak interfacial properties between the load bearing carbon fibers and the epoxy resin system. A corrugated fracture surface was observed with either smooth carbon fibers or the vacancy where they resided. Hackle-type fracture behavior was observed in the resin rich regions between fibers with no signs of permanent deformation.

- The CNT modified material system exhibited vastly different fracture morphology and topology compared with the baseline CFRP. The fracture surfaces for the CNT modified system were highly three-dimensional with undercutting cleaving and conchoidal fracture behavior. Permanent deformation before fracture is evident as well giving rise to large amounts of absorbed energy during fracture. CNTs emerging from the fracture surface have been detected, and energy absorption during fracture has been attributed to their fracture and pullout.

7 FINITE ELEMENT SIMULATIONS OF MODE I FRACTURE

7.1 Introduction

In order to gain additional insight into the crack growth behavior observed under Mode I loading conditions, linear elastic fracture mechanics based finite element simulations have been performed. The complexities associated with the fracture growth process, specifically for the CNT enhanced specimens, disallowed the experimental determination of the Mode I critical strain energy release rate, G_{Ic}, using any analytical methods involving the direct input of incremental crack lengths. Since the crack was observed to grow along multiple fronts, the in-situ experimental measurement was not possible. This modeling effort is an attempt to simulate the experimentally observed phenomenon in order to elucidate the mechanisms that gave rise to the response.

7.2 Model Setup

Three-dimensional simulations were performed using the Adagio code within Sierra. The adagio code is a non-linear implicit code for quasi-static mechanics problems, ideal for the modeling of orthotropic composite materials with a well defined stack sequence. The simulations used 8 noded hexahedral elements, which use one-point integration in addition to an hourglass control scheme to restrict any spurious displacement modes. Element size was chosen to be predominantly 0.5 mm. An elastic material model was developed with orthotropic properties used for the three-dimensional simulation. To review, Hooke‘s law for an orthotropic material model can be written as

$$\begin{Bmatrix} \varepsilon_{11} \\ \varepsilon_{22} \\ \varepsilon_{33} \\ \gamma_{23} \\ \gamma_{13} \\ \gamma_{12} \end{Bmatrix} = \begin{bmatrix} \frac{1}{E_{11}} & -\frac{\upsilon_{21}}{E_{22}} & -\frac{\upsilon_{31}}{E_{33}} & 0 & 0 & 0 \\ -\frac{\upsilon_{12}}{E_{11}} & \frac{1}{E_{22}} & -\frac{\upsilon_{32}}{E_{33}} & 0 & 0 & 0 \\ -\frac{\upsilon_{13}}{E_{11}} & -\frac{\upsilon_{23}}{E_{22}} & \frac{1}{E_{33}} & 0 & 0 & 0 \\ 0 & 0 & 0 & \frac{1}{G_{23}} & 0 & 0 \\ 0 & 0 & 0 & 0 & \frac{1}{G_{13}} & 0 \\ 0 & 0 & 0 & 0 & 0 & \frac{1}{G_{12}} \end{bmatrix} \begin{Bmatrix} \sigma_{11} \\ \sigma_{22} \\ \sigma_{33} \\ \tau_{23} \\ \tau_{13} \\ \tau_{12} \end{Bmatrix} \tag{39}$$

where the normal strains, ε_{ij}, are related to the normal stresses, σ_{ij}, through the elastic modulii, E_{ii}, and the Poisson's ratios, $\nu_{ij,}$ and the shear strains, γ_{ij}, are related to the shear stresses, τ_{ij}, through the shear modulii, G_{ij}. Rewriting Equation (39) in a more compact form gives

$$\{\varepsilon\} = [S]\{\sigma\} \tag{40}$$

The compliance matrix, [S], is symmetric based on a consideration of strain energy and, hence,

$$S_{ij} = S_{ji} \tag{41}$$

So, it can be seen that only nine material properties are needed to characterize an orthotropic material. Namely, they are

$$E_{11}, E_{22}, E_{33}, \nu_{12}, \nu_{13}, \nu_{23}, G_{12}, G_{13}, G_{23} \tag{42}$$

The values used for this CFRP material system are given as

$$
\begin{aligned}
E_{11} &= 58.9GPa \\
E_{22} &= 57.0GPa \\
E_{33} &= 9.8GPa \\
\nu_{12} &= 0.048 \\
\nu_{13} &= 0.303 \\
\nu_{23} &= 0.303 \\
G_{12} &= 4.6GPa \\
G_{13} &= 4.6GPa \\
G_{23} &= 4.6GPa
\end{aligned}
\tag{43}
$$

Note that the fabric employed is an 8-harness satin weave architecture. It has mutually orthogonal fiber directions and is modeled as two plies of uni-directional fabric. Since the 8-harness satin weave has low crimp, this is an acceptable first order approximation without complicating the model with the undulations associated with the warp and weft tows. A typical unit cell for an 8-harness satin weave architecture can be seen in Figure 66. A unit cell is defined as the smallest repeating unit of the textile that, when translated in-plane only, can replicate the textile pattern.

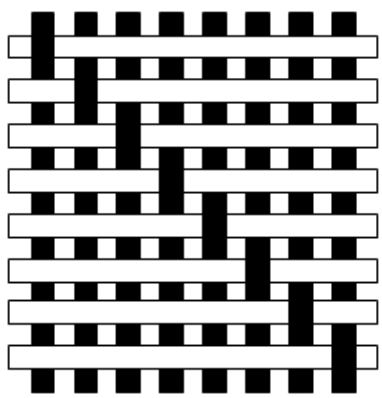

Figure 66 Unit cell for an 8-harness satin weave textile composite fabric.

Due to the asymmetry associated with the 8-harness satin weave, a balanced and symmetric laminate was constructed for the experiments, and replicated in the finite element analysis with the idealization of unidirectional plies. As can be seen in Figure 67, the stack sequence

can be idealized for input into the finite element model. The idealization would involve utilizing a stack sequence of $[0/90/0/90/0/90/0/90/90/0/90/0/90/0/90/0]_s$ which is the same as $[[(0/90)_4]_s]_s$. This results in a 32 ply stack sequence, resulting from the 16 plies of textile composite.

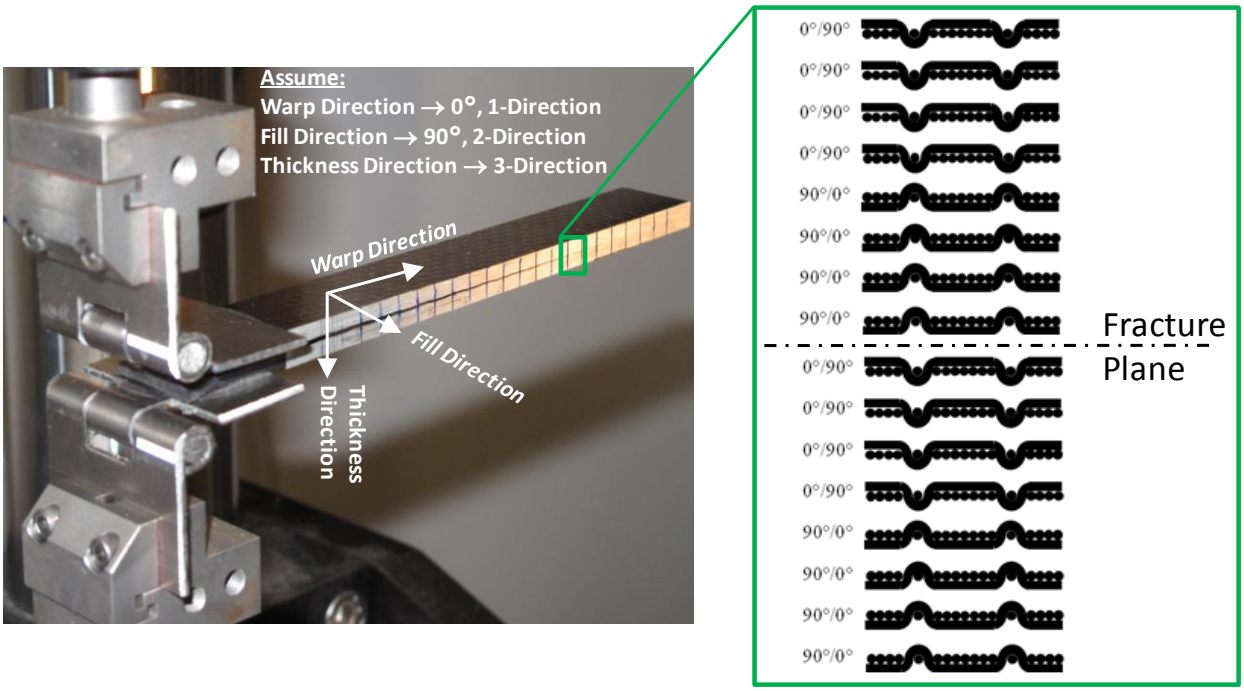

Figure 67 Experimental procedure showing the stack sequence for the DCB.

7.3 Results

7.3.1 Stress Based Analysis

Before going forward with a fracture based analysis, preliminary stress analysis models were simulated for the DCB geometry to ensure the model was converging and giving reasonable behavior and results with mesh density and element size chosen. Preliminary models were first run to verify the output in terms of stress magnitude. As can be seen in Figure 68, a DCB specimen with a wedge inserted between the two beams results in considerable tensile stress concentrations ahead of the wedge. The far field stress diminishes and the resulting stress state in the region of interest is satisfactory for model specifics.

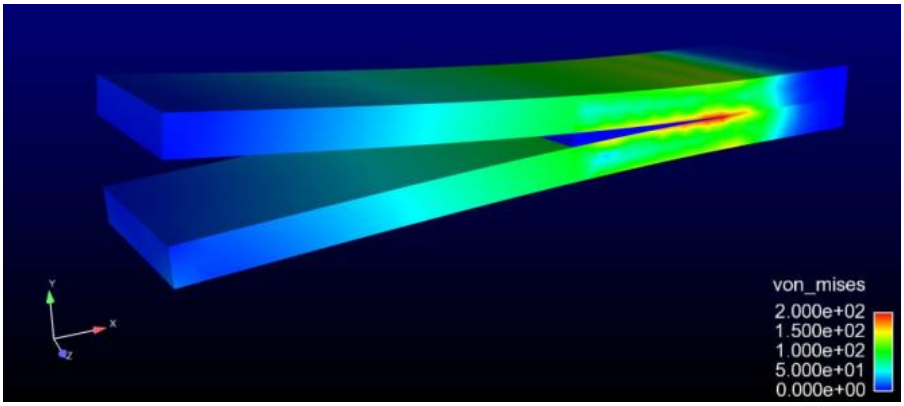

Figure 68 Three-dimensional stress state for a DCB specimen with a wedge.

7.3.2 Single Plane Fracture Based Analysis

With the geometry of the specimen defined and the model working robustly for elastic solutions, an initial analysis was performed using cohesive surface zone elements. These are 8 noded elements with zero volume to start. They are meshed along the fracture interface of interest and are defined by a traction-separation law. Once a critical separation distance is achieved for these elements, the bond breaks and the fracture advances. The critical parameters for these elements are the peak traction stress, the separation to peak traction, and the critical separation. The critical strain energy release rate is the integration of this response curve for the traction versus separation. Variations in the separation law can be applied in order to match experimentally observed micromechanics. Typically, the separation to peak traction is kept very small (1 % of critical separation was employed in this study) in order to generate an artificially stiff element that only degrades during separation. The intent of this element type is not to induce elasticity with a known stiffness, but to fracture when criteria is met.

An initial variation in fracture behavior has been performed by changing the critical Mode I strain energy release rate, as shown in Figure 69. As the GIc is increased, the stress states for σ_{xx}, σ_{yy}, and the effective stress are also increased. In addition, the COTD increases as a result, which can be visualized with the variation in the respective traction separation laws.

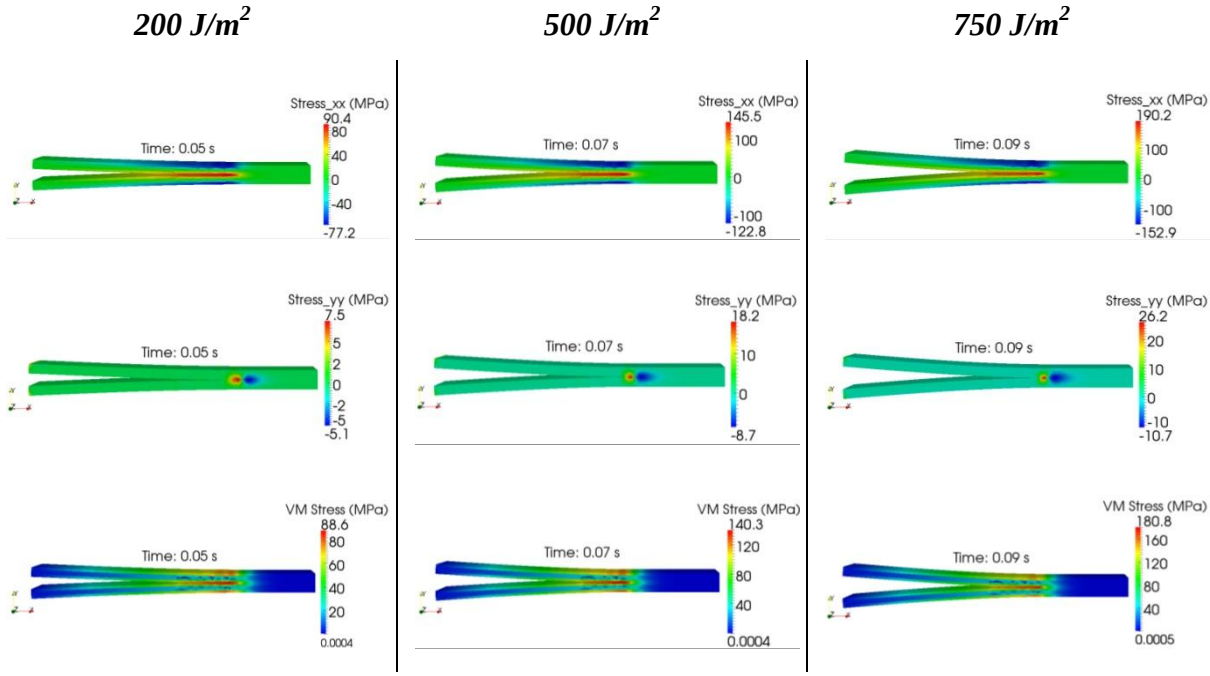

Figure 69 Resulting stress magnitudes for a variation in G_{Ic}.

The resulting load versus COTD response curves can be seen in Figure 70 for a short specimen. The run times for the analysis are significant and shortening the span of the specimen makes the computation much more time efficient. The vertical drops observed in this plot are only an artifact of this artificial shortening of the specimen length. Longer specimens can be extrapolated from the respective loading curves. The simulation predicts that all the specimens initially have the same stiffness but reduce accordingly as damage is induced.

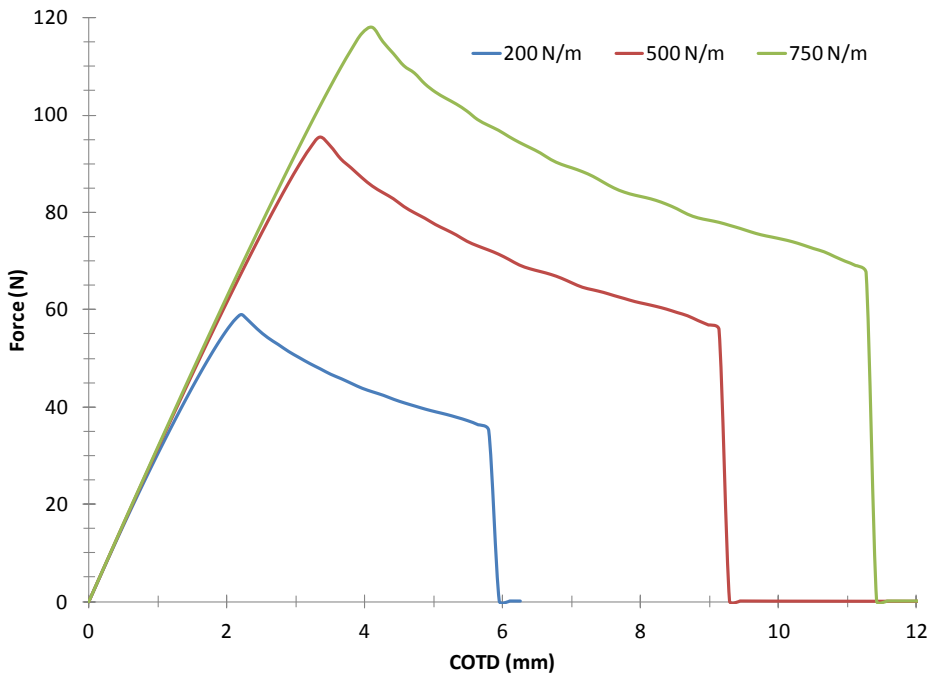

Figure 70 Resulting load versus COTD responses for a variation in G_{Ic}.

A comparison of the load and displacement response between the simulation and the experiment is promising, with good agreement in qualitative nature. An image showing the meshed model under load alongside the specimen during experiment can be seen in Figure 71. The hinges in the specimen have not been accounted for in the analysis. The hinges can be flipped in either direction during the experiment and the implications will be increasing the local rigidity of the DCBs or shortening the initial crack length.

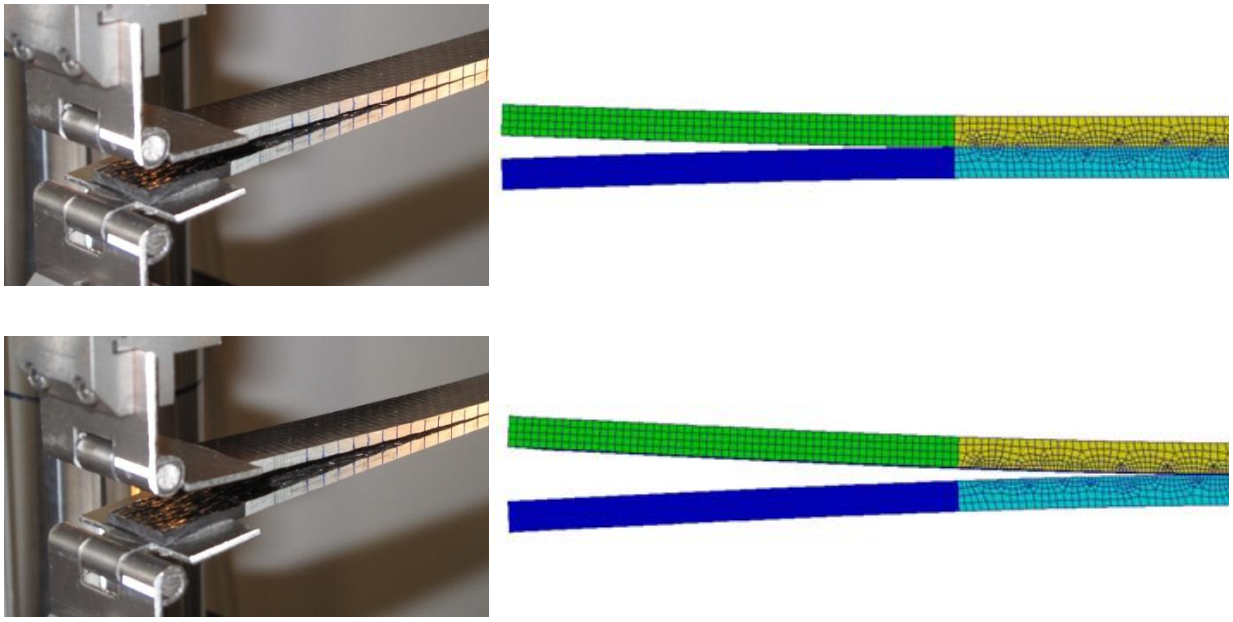

Figure 71 Cohesive surface element fracture simulation with experimental observations during testing.

Predictions with a single crack along the mid-thickness plane have been superposed with experimental results in Figure 72. As was previously reported in Chapter 0, the CNT modified specimens experienced a dual crack front between the main crack plane and the next adjacent plane one ply away. This simulation superposed in Figure 72 does not attempt or account for this complexity. Again, the drop offs in the simulation load bearing ability are a result of the artificial shortening of the specimens for time efficiency. Close inspection of these plots show that the simulations predict a smaller initial stiffness and roll off without enough load bearing ability during fracture. The initial stiffness variation is likely attributed to the steel hinges not modeled but used in experiments. Other important points to remember are that the fiber bridging and permanent deformation mechanisms are not captured in this LEFM model as well. These effects will result in increased load bearing ability during crack propagation, as the experiments are demonstrating. Also, the 200 J/m^2 predicted for the FEM simulation agrees well with the experimentally determined values.

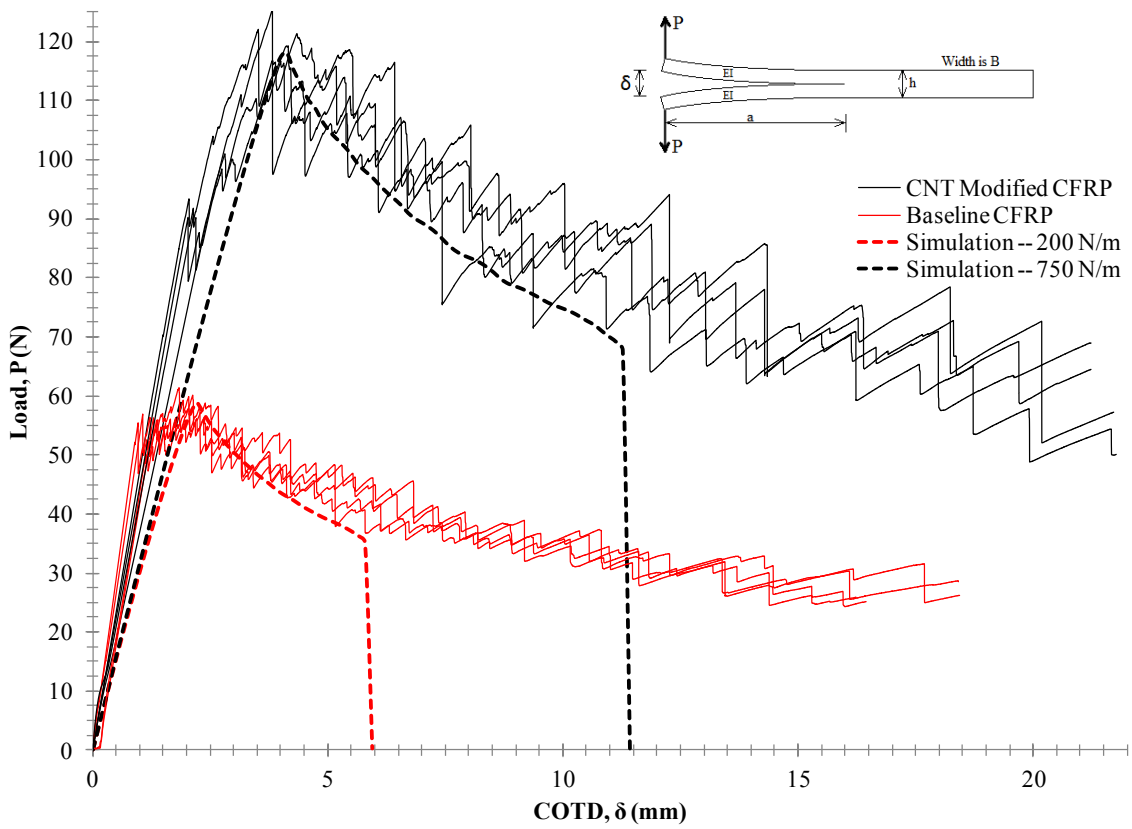

Figure 72 Resulting simulation plots superposed onto experimental data.

7.3.3 Dual Plane Fracture Based Analysis

As a result of the experimentally observed phenomenon demonstrating two crack fronts advancing along the specimen length for the CNT modified double cantilever beam specimens, a modeling effort was pursued to gain additional insight into the driving forces to cause this. Recall, the dual fracture planes that were reported in Chapter 0. A typical case for the CNT modified specimens can be seen in Figure 73.

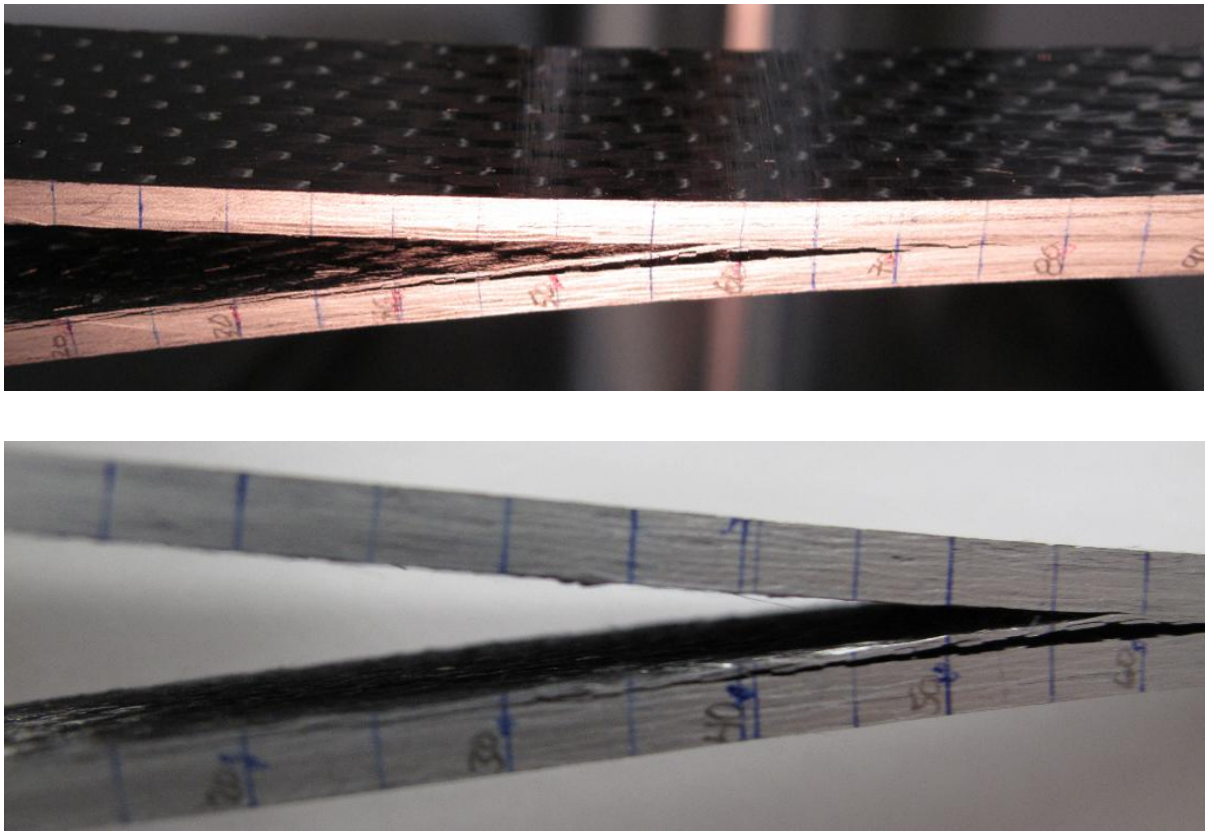

Figure 73 Dual crack planes visible during Mode I testing of CNT modified CFRP.

In order to model this effect, a series of sensitivity analysis were performed to understand how the variations in both the separation to failure and strain energy release rates affected the results from both qualitative fracture mechanisms to a quantitative load versus COTD response curve. It has been found that for a secondary crack to form at another interface, that second interface must have a lower critical strain energy release rate. This is consistent with the fact that the stress state at this secondary interface is lower in magnitude. The crack front along the mid-thickness plane arrests and then the strain energy builds up a bifurcating value causing the second crack to form and grow.

The area beneath the traction separation response curve is defined as the strain energy release rate. The peak traction, the distance to the peak traction, and the final separation to failure are input into the FEA code in order to define the fracture process, and maintain the respective strain energy release rate for the interfaces. This method of defining the behavior of the cohesive zone elements is phenomenological in order to capture complex micromechanics of

the fracture process such as void nucleation, coalescence, and final rupture without actually modeling them. They are all lumped into this separation to failure definition. An additional complexity arises, however, when the various fracture properties have their own unique laws based on variations in the micromechanics. The implications to the traction separation law parameters and the fracture properties will now be explored.

A sensitivity analysis on the separation to failure value has been employed for the CNT modified DCB specimens, as can be seen in Figure 74. The separation to failure values employed are given to both the baseline material interface and the CNT modified interface. The strain energy release rate has been held constant for each respective interface, with the baseline CFRP interface (of the CNT modified specimen) at 200 N/m while the CNT modified was held constant at 300 N/m or 300 J/m^2. Four simulations have been performed, as outlined in Table 7, in order to see the resulting response curves and respective fracture behavior.

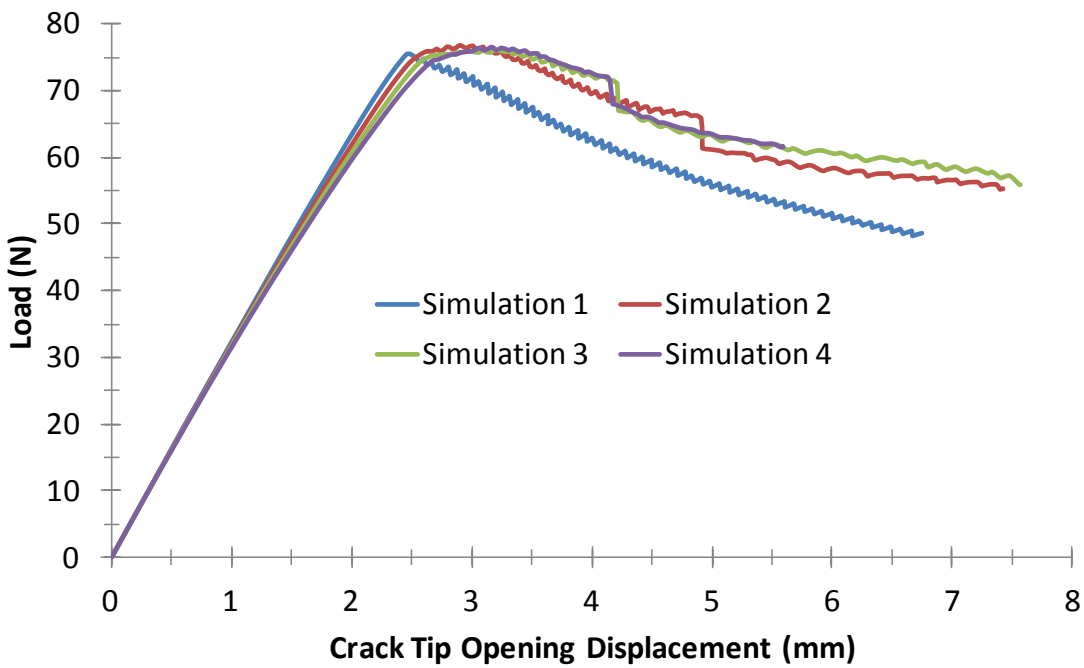

Figure 74 Load versus COTD response for a separation to failure variation in G_{Ic} for both the baseline CFRP and the CNT enhanced CFRP interfaces.

As can be seen in Figure 74, Simulation 2, 3, and 4 have sudden load drops associated with their responses when the separation to failure is increased from 0.03 to 0.05 mm, as depicted

in Table 7. These load drops represent the instability of a new crack front, indicative of rapid growth associated with a secondary crack. This type of secondary crack does not form in Simulation 1. In order for a secondary crack to form in simulations with lower separation to failure values, the fracture toughness at the CNT modified interface must be increased.

Table 7 Input properties for separation to failure sensitivity analysis in Figure 74

	Simulation Number			
	1	***2***	***3***	***4***
Separation to Failure (mm)	*0.02*	*0.03*	*0.04*	*0.05*
Baseline CFRP Critical G_{Ic} (J/m^2)	*200*	*200*	*200*	*200*
CNT Modified CFRP Critical G_{Ic} (J/m^2)	*300*	*300*	*300*	*300*

Investigating the initial case of secondary crack formation observed in Simulation 2 from Figure 74, a snapshot in time (or increasing COTD) has been illustrated in Figure 75. The formation and growth of the secondary crack can be seen to occur just prior to this local instability in the load versus COTD response curve. As the specimen is further displaced, the secondary crack continues to grow along this new interface. This is qualitatively similar to the behavior observed in the experiments, as can be seen in Figure 73 and Figure 52.

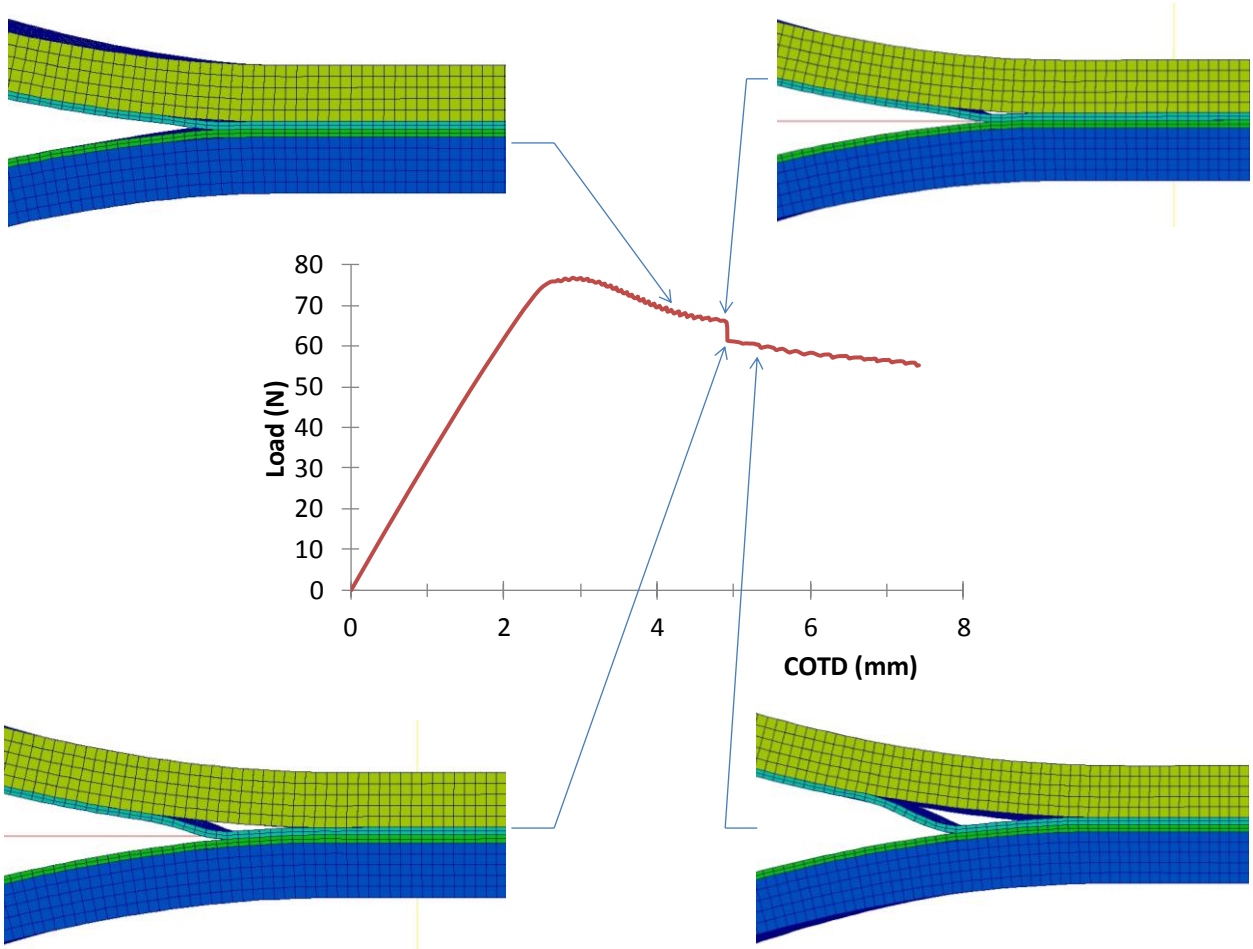

Figure 75 Mechanisms for dual-crack formation in CNT modified CFRP (main crack along CNT modified interface, secondary crack along baseline CFRP interface).

For this next analysis, a delineation has been made between the separation to failure values for the baseline CFRP interface and the CNT modified interface, both existing in the CNT modified material system. The baseline CFRP separation to failure values have been varied with the CNT modified interface held at 0.02 mm. In addition, the strain energy release rate has been increased for the CNT modified interface from 300 to 600 N/m. When the G_{Ic} is increased from 300 N/m to 600 N/m at the CNT modified interface, a crack at the plain interface will form in simulations with lower separation-to -failure values, as can be seen as the load drops in Figure 76. Increasing the separation to failure value at the baseline CFRP interface, as depicted in Table 8, results in several, smaller decreases in the load versus COTD curve rather than fewer larger ones.

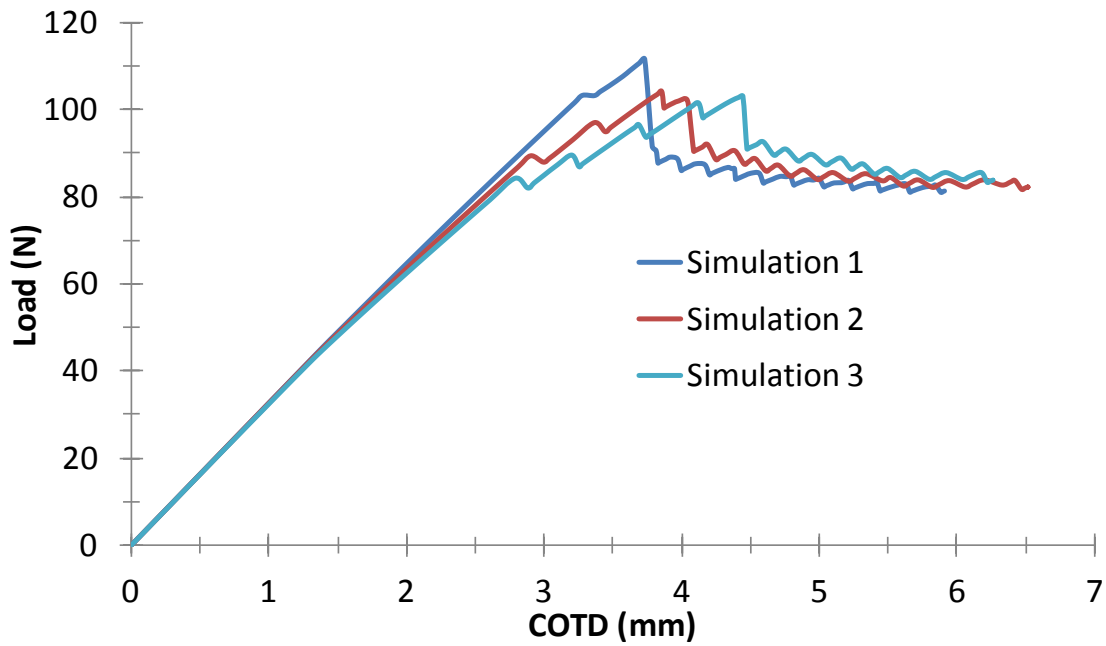

Figure 76 Load versus COTD response for a separation to failure variation in G_{Ic} for only the baseline CFRP material system interface.

Table 8 Input properties for separation to failure sensitivity analysis in Figure 76.

	Simulation 1	***Simulation 2***	***Simulation 3***
Baseline CFRP separation to failure (mm)	*0.02*	*0.05*	*0.08*
CNT Modified CFRP separation to failure (mm)	*0.02*	*0.02*	*0.02*
Baseline CFRP Critical G_{Ic} (J/m^2)	*200*	*200*	*200*
CNT Modified CFRP Critical G_{Ic} (J/m^2)	*600*	*600*	*600*

In order to now understand the effect of varying the G_{Ic} at the CNT modified CFRP interface, the simulation depicted in Figure 77 and Table 9 have been performed. As can be seen, G_{Ic} has been varied from 600 to 800 N/m. The baseline CFRP G_{Ic} has been held constant at 200 J/m^2, similar to the experimental results obtained in Chapter 0. The variation performed reveals that the qualitative nature of the response is essentially identical, but the peak load achieved changes. As the G_{Ic} is increased, the peak load also increases.

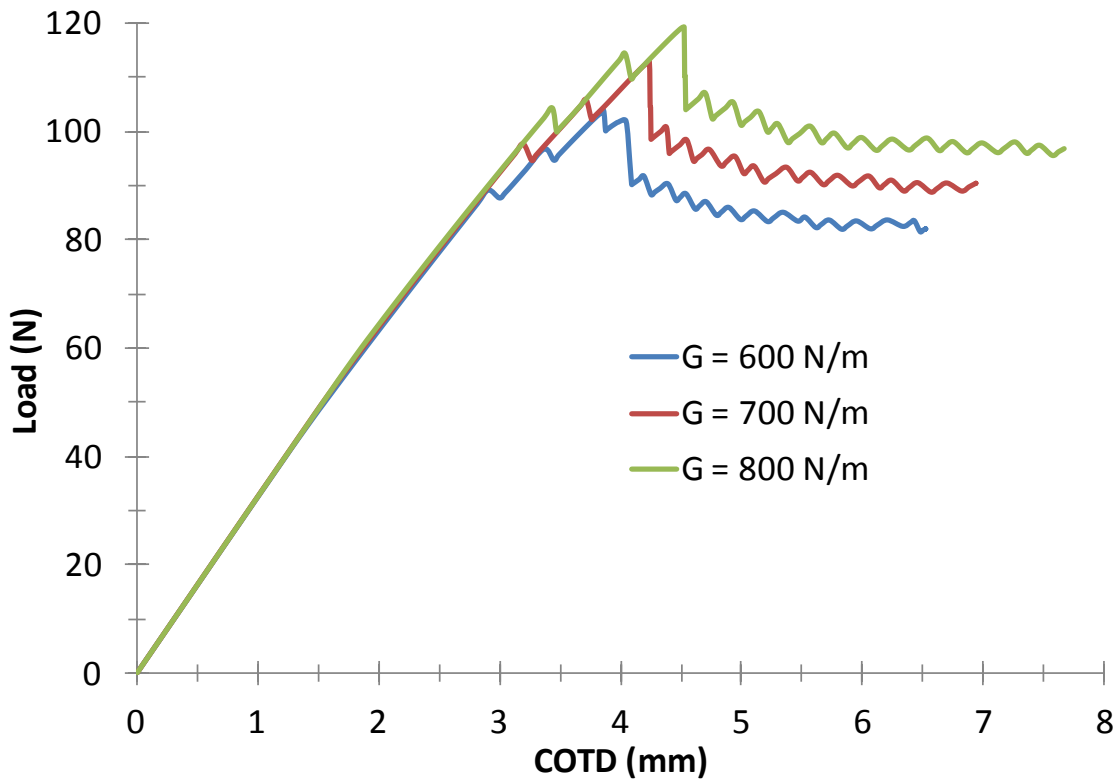

Figure 77 Load versus COTD response for a G_{Ic} variation for only the CNT enhanced CFRP interface.

Table 9 Input properties for GIc sensitivity analysis in Figure 77.

	Simulation 1	*Simulation 2*	*Simulation 3*
Baseline CFRP separation to failure (mm)	*0.05*	*0.05*	*0.05*
CNT Modified CFRP separation to failure (mm)	*0.02*	*0.02*	*0.02*
Baseline CFRP Critical G_{Ic} (J/m^2)	*200*	*200*	*200*
CNT Modified CFRP Critical G_{Ic} (J/m^2)	*600*	*700*	*800*

Comparing the peak loads achieved in the simulation of Figure 77 with experimental results, the plot of Figure 78 has been made. This plot illustrates that modeling the CNT modified interface at 800 J/m2 gives good agreement with the finite element model. Secondary fracture mechanisms are formed as a result of the respective strain energy release rates and separation to failure values. Also, the comparison of the strain energy release rates used in the FEM compare well with the experimentally measured values shown in Figure 60 or Figure 61. The initial stiffness variation between the model and the experiment is attributed

to the hinge stiffness contribution to the overall flexural rigidity of the specimen. This can be easily modified and accounted for in future analysis.

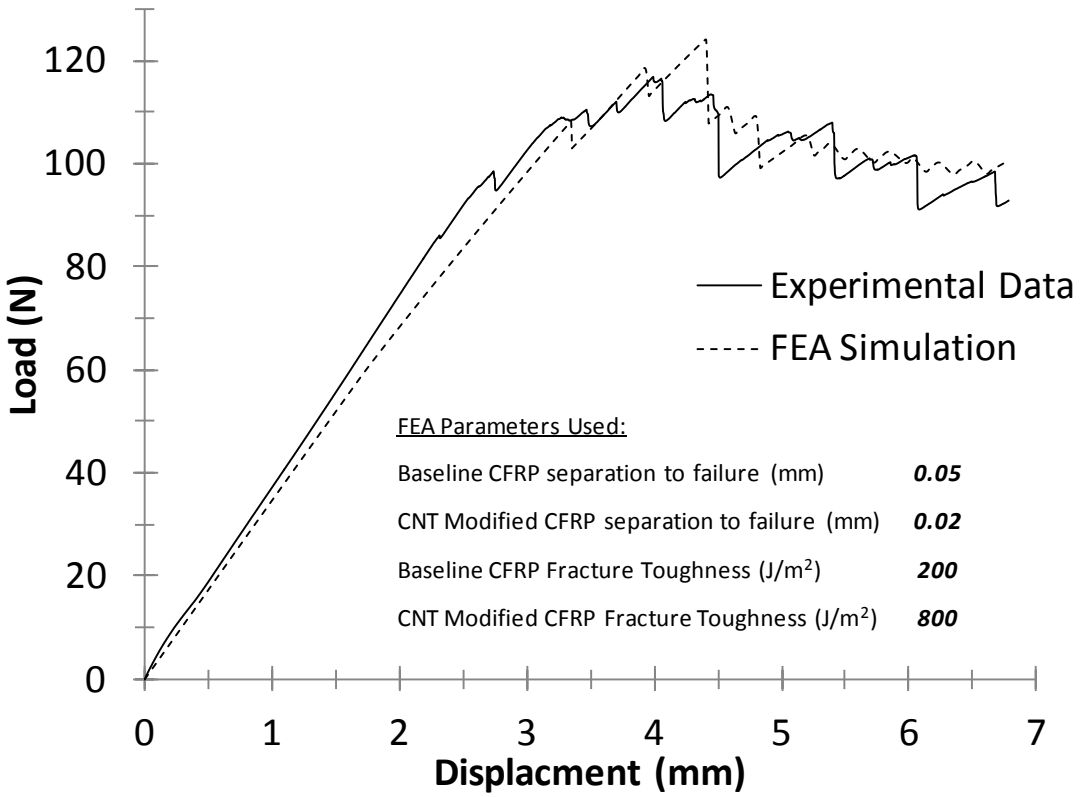

Figure 78 Experimental load versus COTD response along with the FEA simulation.

7.4 Conclusions

A series of finite element models has been performed to investigate the complexities associate with double cantilever beam experiments. Adagio code was utilized within the Sierra package for these quasi-static loading cases. An orthotropic material model was performed and the satin harness weave architecture was idealized as multiple uni-directional plies to form the stack sequence. A variation in material fracture properties and separation to failure values has been performed. A summary of the findings are as follows:

- The CNT modified interface must have a larger critical strain energy release rate than the baseline CFRP interface in order for a double crack to form.

- Small load drops prior to the peak load will take place if the separation to failure value at the baseline CFRP interfaces are increased to be larger than the value at the CNT modified interface. This is similar to what was experimentally observed.

- The ratio of the baseline CFRP interface separation to failure value compared with the CNT modified interface effects when the crack will jump. FEM results indicate that the best agreement with the experimental data occurs when the baseline CFRP interface separation to failure is at least twice that of the CNT interface.

- Good agreement was found between the simulations and the experimental results in terms of both the qualitative nature of the fracture process and the fracture properties measured from experiment. The resulting force versus COTD simulations, when superposed with the experiments, are very close to the experiments with deviations associated with the DCB hinge stiffness.

This page left intentionally blank.

8 MODE II FRACTURE CHARACTERIZATION

8.1 Introduction

The fracture toughness of composite materials for transverse loading is primarily governed by the ability for the material carry shear stress between adjoining lamina. When there is a mismatch in the fiber orientation of the adjoining lamina, the shearing stress can be considerable due to variations in the Poisson contraction. Microcracks are developed in this resin rich, interply zone, eventually coalescing to form what is known as a delamination crack. Several other factors control the ability for a material to exhibit toughness to mode II fracture. Some of these include constituent and interfacial properties of the fiber and matrix, type of loading and environmental conditions [60].

End notched flexure tests are primarily used to simulate the mode II delamination phenomenon in composite materials from transverse shearing stress which is frequently encountered in composite structures. The ENF test is based on a simple 3-point flexure experiment with a starter flaw, but has the disadvantage of stability concerns for the crack growth, which are overcome with appropriate aspect ratio between starter crack length and beam span. In addition, it is said to only give initiation values of the mode II strain energy release rate [61]. Also, there is the issue that, on the microscopic scale, the micro-crack formations have been shown [62]-[63] to actually be mode I opening cracks, caused from the normal stress present when the stress tensor is transformed, which have coalesced due to the brittle nature of the binding resin. For these reasons, in addition to the friction present at the interface, it is not widely accepted as a suitable test method and, hence, no common testing standard has been accepted.

The ENF tests were performed in order to identify the Mode II strain energy release rate characteristics for the baseline and CNT enhanced CFRP material investigated in this study. The loading rate for this three point flexure test was maintained constant, in addition to the boundary conditions and specimen geometry.

8.2 Analytical Methods

The ENF experimental setup can be idealized as the schematic in Figure 79. A central load, *P*, is applied at a distance $x = L$ from the simply supported ends. The beam, of width B, has a Teflon insert starter crack along the neutral axis for a distance, *a*, from the end support toward the mid span of the beam. The split ends have a reduced second area moment of inertia as a result, which gives rise to a flexural rigidity of $1/8^{th}$ of the value it has at the other, intact end. With a transverse deflection, v, the moment curvature relation for a linear elastic beam of isotropic material with a rate dependent modulus, E, can be expressed as

$$M = -EI\frac{\partial^2 v}{\partial x^2} \tag{44}$$

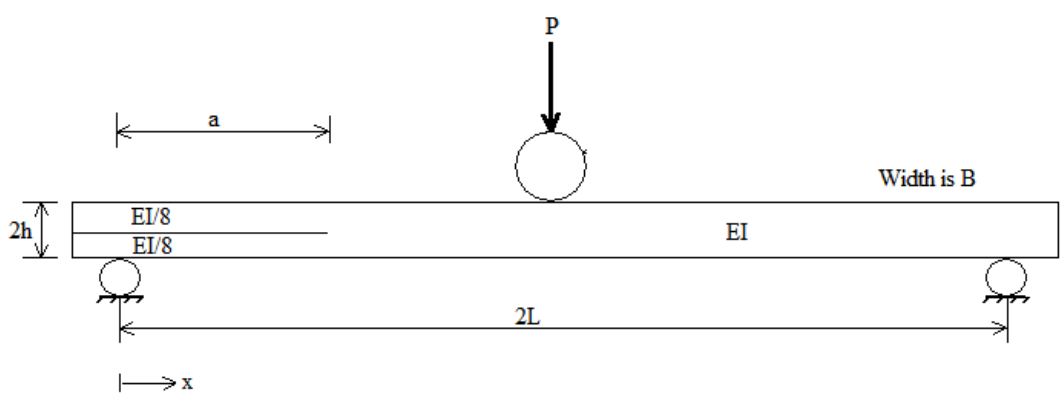

Figure 79 ENF schematic showing relation between geometry and crack length.

For the region $0 \le x \le a$, Equation (44) can be shown to be

$$\frac{Px}{4} = -E\frac{I}{8}\frac{\partial^2 v}{\partial x^2} \tag{45}$$

For the region $a \le x \le L$, Equation (44) can be shown to be

$$\frac{Px}{2} = -EI\frac{\partial^2 v}{\partial x^2} \tag{46}$$

and, lastly for the region $L \le x \le 2L$, Equation (44) can be shown to be

$$PL - \frac{Px}{2} = -EI\frac{\partial^2 v}{\partial x^2} \tag{47}$$

These differential equations in Equations (45) - (47) can be simultaneously solved with the appropriate boundary conditions of slope and displacement to ensure compatibility and determination of the integration constants. The total deflection, assuming only bending deformation, can then be expressed in terms of the delamination growth and the elastic modulus as

$$v = \frac{P(2L^3 + 3(a + \Delta a)^3)}{12EI} \tag{48}$$

Energy Release Rate, *G*, is the rate of change in potential energy with respect to a change in crack area, *A*, and is expressed as

$$G = -\frac{\partial \Pi}{\partial A} \tag{49}$$

where Π is the total of the potential energy from internal strain energy, *U*, and external forces. Now, balance of total energy, *E*, for a solid body gives

$$\begin{aligned} \frac{\partial E}{\partial A} &= \frac{\partial \Pi}{\partial A} + \frac{\partial W_s}{\partial A} = 0 \\ \frac{\partial \Pi}{\partial A} &= -\frac{\partial W_s}{\partial A} \end{aligned} \tag{50}$$

where W_s is the decrease of work required to create new surfaces, which can be expressed in terms of the surface energy, γ_s, the crack length, *2a*, and the width, *B*, as

$$W_s = 4aB\gamma_s \tag{51}$$

Therefore, from Equations (49) and (50), we can say the critical strain energy release rate, G_c, is given as

$$G_c = \frac{\partial W_s}{\partial A} \tag{52}$$

The potential energy of a body, Π ,can be expressed in terms of the work done, F, from the external forces and the internal strain energy as

$$\Pi = U - F \tag{53}$$

With a dead load, P, applied to the solid body, the internal strain energy caused from a displacement out to Δ can be expressed as

$$U = \int_0^{\Delta} P d\Delta = \frac{P\Delta}{2} \tag{54}$$

and the work done by the load, P, acting through a displacement Δ can be expressed as

$$F = P\Delta \tag{55}$$

so, substitution of Equations (54) and (55) into Equation (53) gives

$$\Pi = -\frac{P\Delta}{2} = -U \tag{56}$$

From Equation (49), we have

$$G_c = -\frac{\partial \Pi}{\partial A} = \frac{\partial (U)}{\partial A} \tag{57}$$

and the infinitesimal crack area, ∂A, can be expressed in terms of the width, B, and infinitesimal crack length, ∂a, as

$$\partial A = B \partial a \tag{58}$$

So, the strain energy for a dead load, P, can be written as

$$G_c = \frac{1}{B}\left(\frac{\partial U}{\partial a}\right)_P \tag{59}$$

From Equation (54), Equation (59) can be written as

$$G_c = \frac{1}{B}\left(\frac{\partial\left[\frac{P\Delta}{2}\right]}{\partial a}\right)_P = \frac{P}{2B}\left(\frac{\partial \Delta}{\partial a}\right)_P \tag{60}$$

The displacement Δ can be expressed in terms of the load and the compliance, C, as

$$\Delta = CP \tag{61}$$

so, the strain energy release rate is

$$G_c = \frac{P}{2B}\left(\frac{\partial[CP]}{\partial a}\right)_P \tag{62}$$

which reduces to

$$G_c = \frac{P^2}{2B}\left(\frac{\partial C}{\partial a}\right)_P \tag{63}$$

since the load is constant. Now, considering the transverse displacement given in Equation (48) the compliance of the beam can be defined as

$$C = \frac{v}{P} = \frac{(2L^3 + 3(a+\Delta a)^3)}{12EI} \tag{64}$$

and the partial derivative of Equation (64) with respect to the crack length, a, gives

$$\frac{\partial C}{\partial a} = \frac{\partial}{\partial a}\left[\frac{(2L^3 + 3(a+\Delta a)^3)}{12EI}\right] = \frac{3(a+\Delta a)^2}{4EI} \tag{65}$$

With the beam thickness, $2h$, the second area moment of inertia can be expressed as

$$I = \frac{2Bh^3}{3} \tag{66}$$

So, the critical strain energy release rate can then be expressed as

$$G_c = \frac{9P^2(a+\Delta a)^2}{16B^2h^3E} \tag{67}$$

Stability of the crack growth requires

$$\frac{\partial G_{IIc}}{\partial a} \leq 0 \tag{68}$$

With the compliance, C, given before fracture as

$$C = \frac{2L^3 + 3a^3}{8EBh^3} \tag{69}$$

using Equation (66) for the inertial term. Recall from Equation (57) that

$$G_c = -\frac{\partial \Pi}{\partial A} \tag{70}$$

and,

$$U = \Pi = \frac{P\Delta}{2} \tag{71}$$

for displacement control, resulting in an increase in strain energy as potential energy is increased. This is in contrast to the load controlled case when the potential energy is decreased by the amount of increase in strain energy, as described in Equation (56). Rewriting Equation (60) in terms of the displacement and load for the displacement control case gives

$$G_c = -\frac{1}{B}\left(\frac{\partial\left[\frac{P\Delta}{2}\right]}{\partial a}\right) = -\frac{\delta^2}{2B}\left(\frac{\partial\left[\frac{1}{C}\right]}{\partial a}\right)_\delta \tag{72}$$

Evaluation of the derivative in Equation (62) results in

$$\frac{\partial\left[\frac{1}{C}\right]}{\partial a} = -\frac{72EBh^3a^2}{(2L^3+3a^3)^2} \tag{73}$$

So, the critical strain energy release rate can be written as

$$G_c = \frac{36\delta^2 Eh^3a^2}{(2L^3+3a^3)^2} \tag{74}$$

To satisfy the stability condition set forth in Equation (68), the derivative of G_c must now be determined. This can be shown to be

$$\frac{\partial G_c}{\partial a} = \frac{9\delta^2 a}{8C^2EB^2h^3}\left[1-\frac{9a^3}{2L^3+3a^3}\right] \tag{75}$$

with the compliance, *C*, defined in Equation (69). Rewriting Equation (68) results in

$$\frac{9\delta^2 a}{8C^2EB^2h^3}\left[1-\frac{9a^3}{2L^3+3a^3}\right] \le 0 \tag{76}$$

which results in the inequality

$$1-\frac{9a^3}{2L^3+3a^3}\leq 0 \tag{77}$$

This implies that the aspect ratio between the initial crack length, a, and the half span of the beam, L, must satisfy

$$L\leq \sqrt[3]{3}a \tag{78}$$

or

$$a\geq 0.69L \tag{79}$$

to ensure stability in the crack growth.

8.3 Experimental Methods

8.3.1 Materials

The CFRP material as well as the Polymer-based CNT formulation to enhance the baseline CFRP are the same as those listed in Section 3.2.1. This information is not repeated here for succinctness.

8.3.2 Specimen Preparation

The specimen preparation for both the baseline CFRP and the CNT enhanced system are identical to that described in 6.3.2. The only difference is the stack sequence, Teflon starter crack length, and lack of hinges for the ENF specimens. The stack sequence for the ENF specimens is composed of 8 total plies. Again, these specimens have been layed up to be both balanced and symmetric to eliminate any potential for warping during the cure. In addition, the crack front was to grow along the warp fibers which were oriented colinear with the specimen length. The stack sequence and geometry is listed in Table 10.

Table 10 End notched flexure specimen geometry and stack sequence.

Material	*Baseline CFRP*	*CNT Enhanced CFRP*
Number of Plies	*8*	*8*
Stack Sequence	$[[(0/90)_2]_s]_s$	$[[(0/90)_2]_s]_s$
Thickness (mm)	*2.7*	*2.7*
Width (mm)	*19*	*19*
Length (mm)	*145*	*145*

The starter crack is the same thin 12.7 μm Teflon film used for the DCBs. The Teflon was inserted at the mid-thickness plane protruding approximately 45 mm into the specimen length. This enabled the stability requirements after trimming to final specimen dimensions. A schematic of the final specimen can be seen in Figure 80.

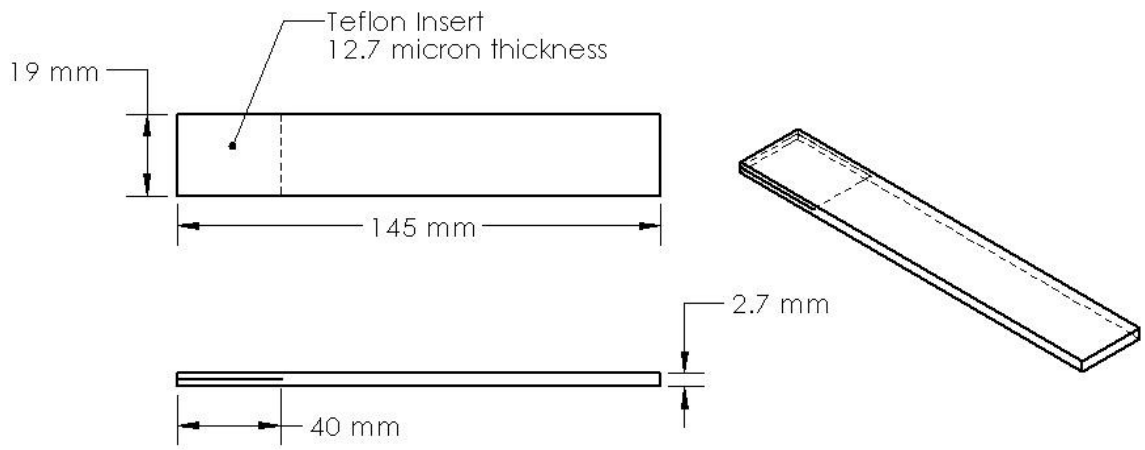

Figure 80 Schematic of approximate ENF specimen geometry.

8.3.3 Testing Procedure

Specimens were tested in three-point flexure under displacement control at 3 mm/min. The state of shear present along the mid-thickness plane drives the crack growth from the Teflon insert. The specimen was loaded until a load drop of 10 % or 20 % was achieved for the CNT enhanced CFRP material or the baseline CFRP material, respectively. This load value was determined through preliminary experiments as the on setting criteria without additional fracture growth.

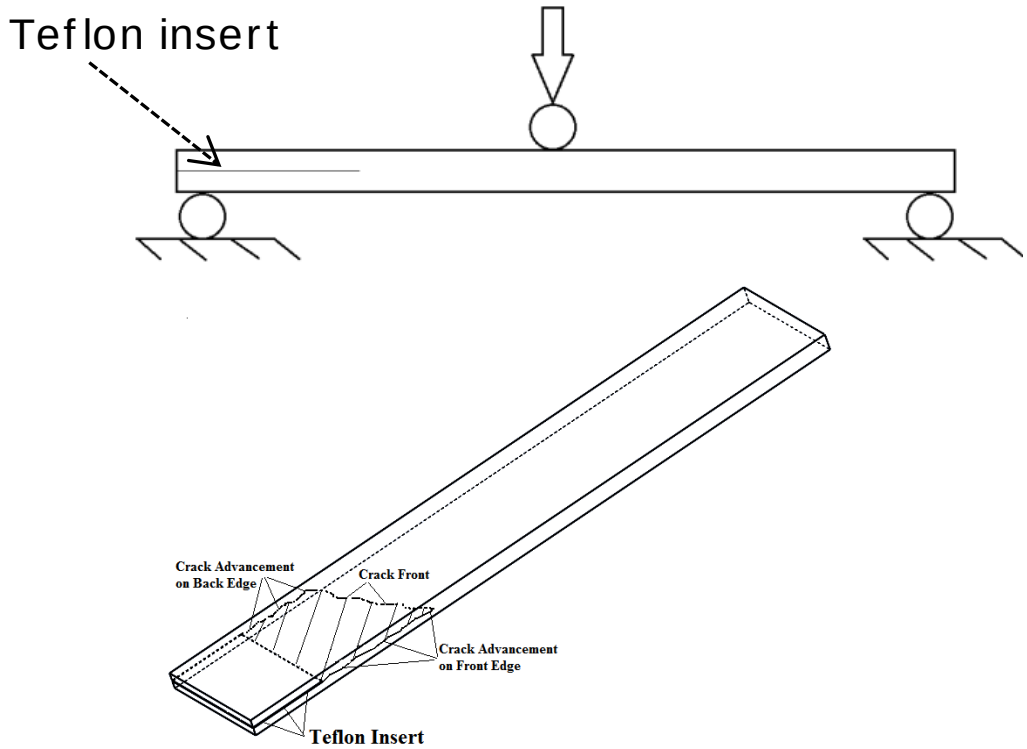

Figure 81 Schematic of 3-point end notched flexure experiment and specimen details.

The load span was set to be 114.3 mm (4.5 inches) which allowed for sufficient specimen overhang from the ends. This load span allowed for a length-to-thickness ratio of approximately 40:1. The supports are hardened steel cylinders of 12.7 mm diameter held in vee-grooves with springs to allow rotation. The load is applied through the same stainless steel cylinder, directly coupled with the crosshead of the universal test machine. A typical loading sequence can be seen in Figure 82 along with the test set-up and description in Figure 83.

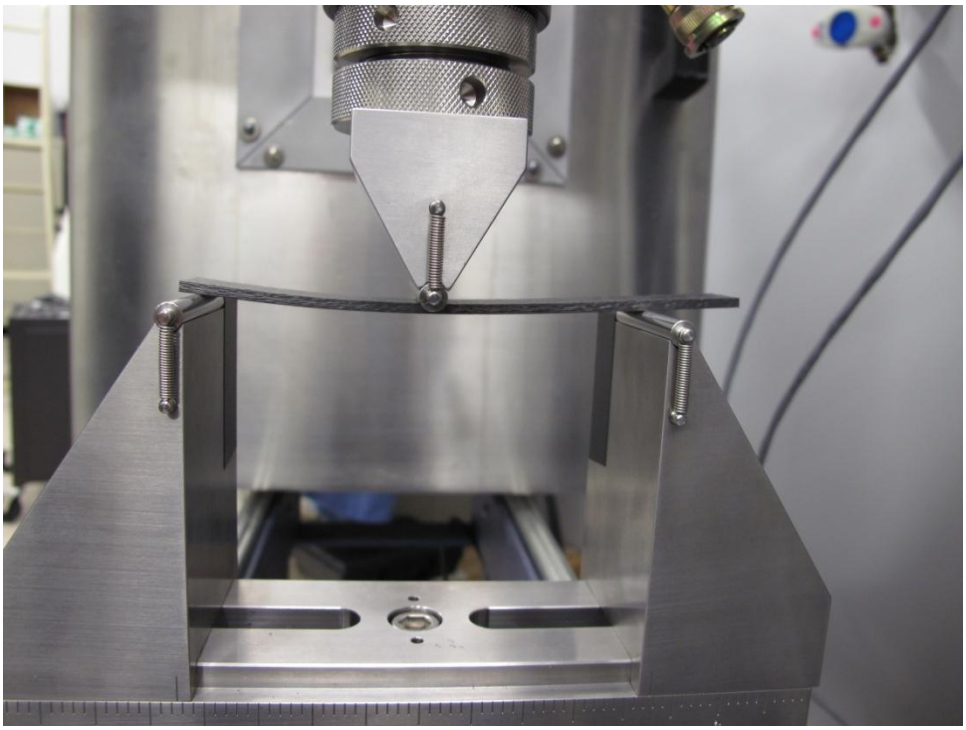

Specimen initially loaded

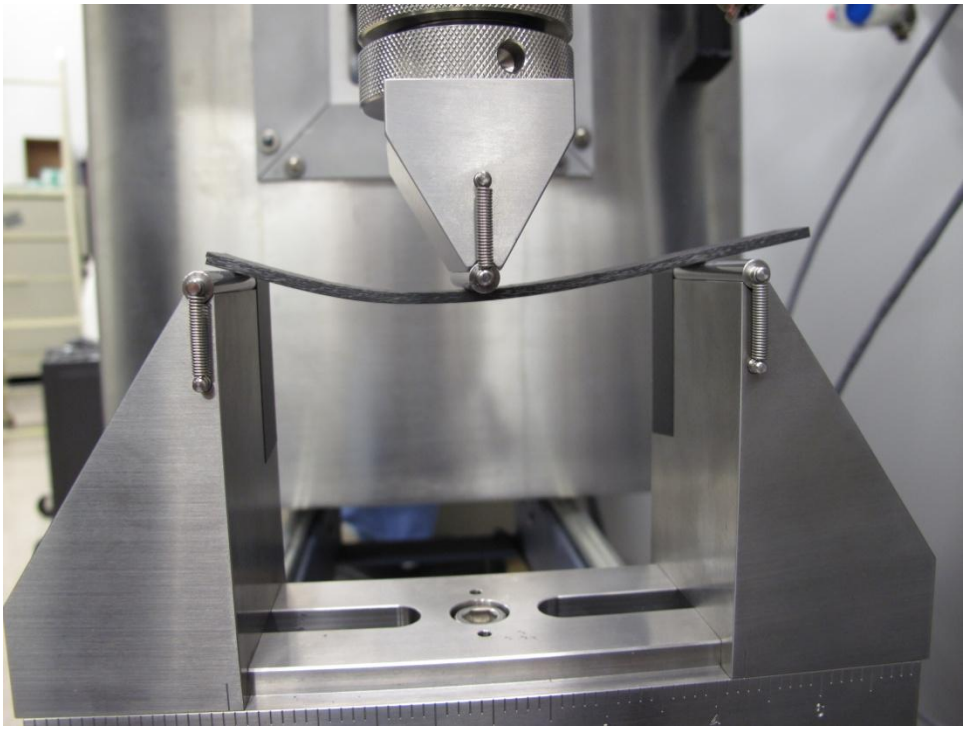

Asymmetric bending due to reduced flexural rigidity from fracture growth

Figure 82 Three-point end notched flexure experiment in-progress.

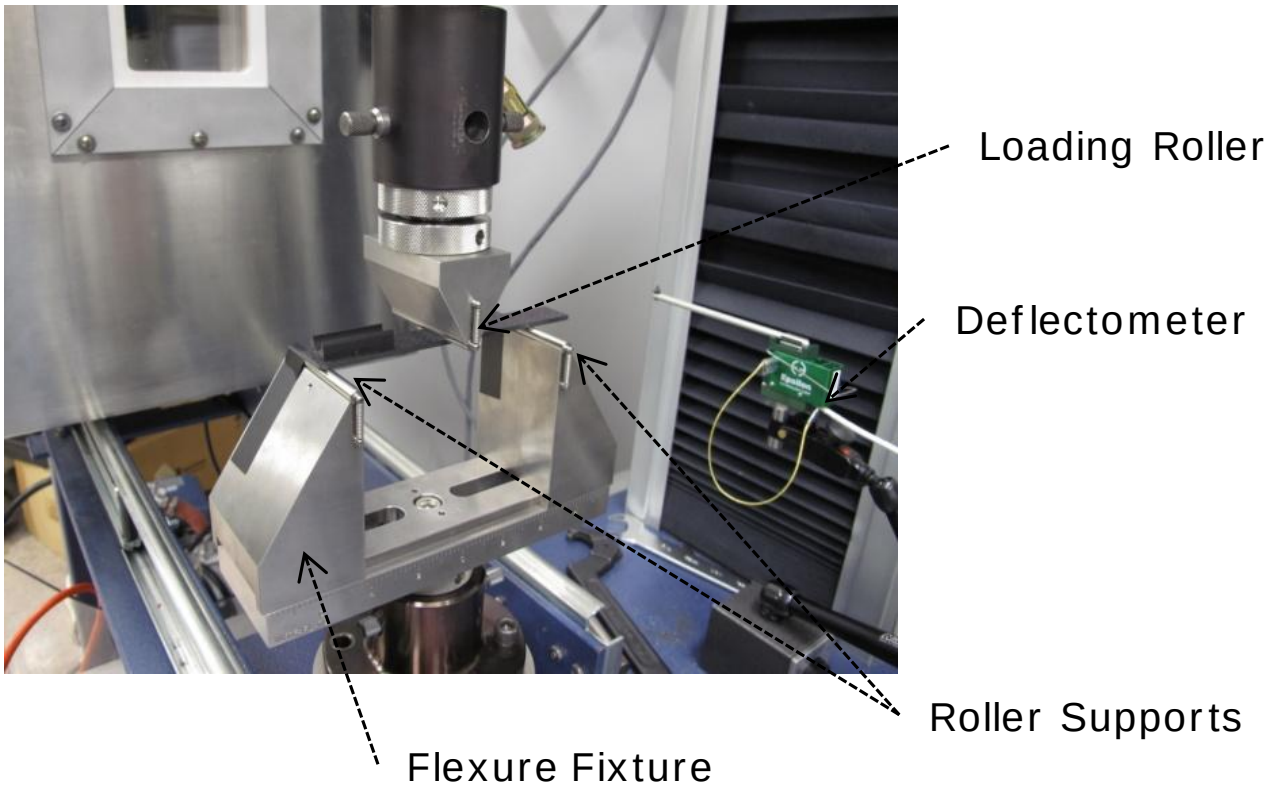

Figure 83 Experimental setup for three-point end notched flexure experiments.

After the crack growth occurred, the specimens were unloaded to a state of zero load. This allowed the determination of any residual deflection for more accurate energy calculations based on the load-deflection integration scheme employed. The specimens were then microscopically inspected for the fracture growth extent. The measurements were recorded for both the front and back of the crack plane observed from the edges. The specimens were then ultrasonically imaged using a focused 5 MHz transducer in a water immersion tank, as shown in Figure 84. The system was set up for pulse-echo detection, and calibrated for quantifiable thickness data based on material thickness and time of flight signal response.

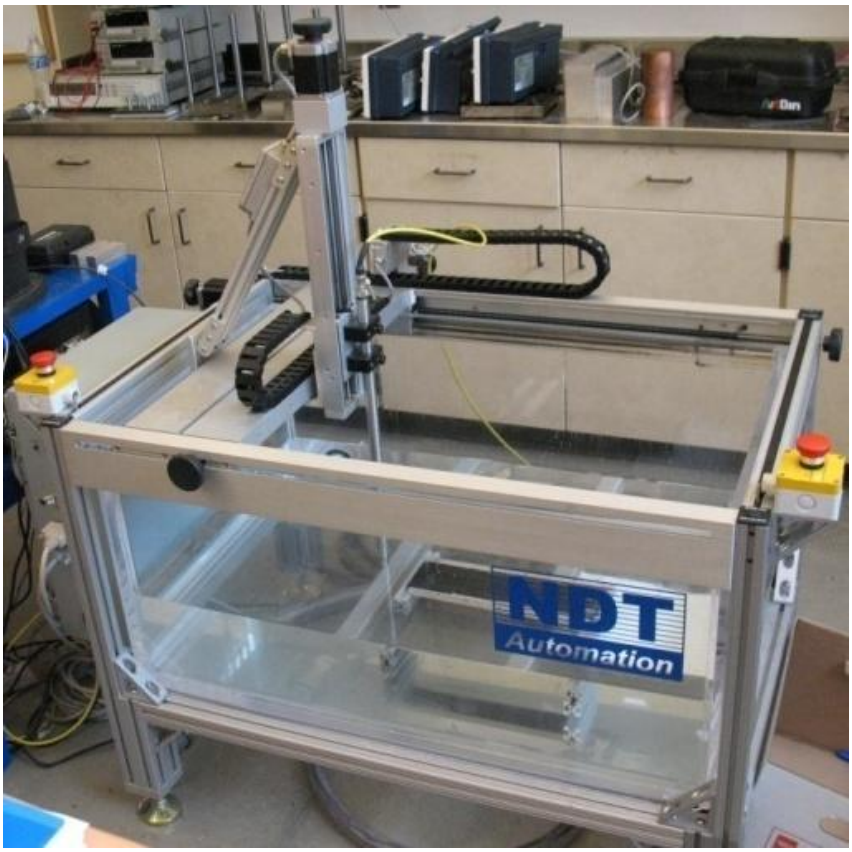

Figure 84 Ultrasonic immersion tank for detecting subsurface fracture growth.

The immersion tank system was set to scan with an approximately 200 μm resolution. The scanning gates for the a-scan were set to both the mid-thickness plane and the back face. However, the near field of the transducer was optimized for signal strength at the crack plane. The specimens were then evaluated using the analytical techniques described in 8.2, in addition to simply normalizing the energy by the new surface area generated, as in Equation (19).

8.4 Results and Discussion

8.4.1 Load versus Deflection Response

The load and deflection are directly measured during testing at a data capture frequency of 10 Hz. The response of all the specimens was consistent between the baseline CFRP and CNT modified CFRP material systems, up until the fracture growth of the baseline materials. As can be seen in Figure 85, the response is linear in nature until fracture for the baseline CFRP.

The load drops catastrophically once a bifurcating load value is attained. The load drops until redistribution occurs and the crack growth arrests. The CNT modified system is similarly linear until approximately 6 mm of central span deflection is achieved. Beyond this, the load increases at a reduced rate with indications of stable crack growth and permanent deformation. The CNT modified system withstood an approximately 88 % higher load bearing ability before significant crack growth, with a 114 % larger deflection at the peak load.

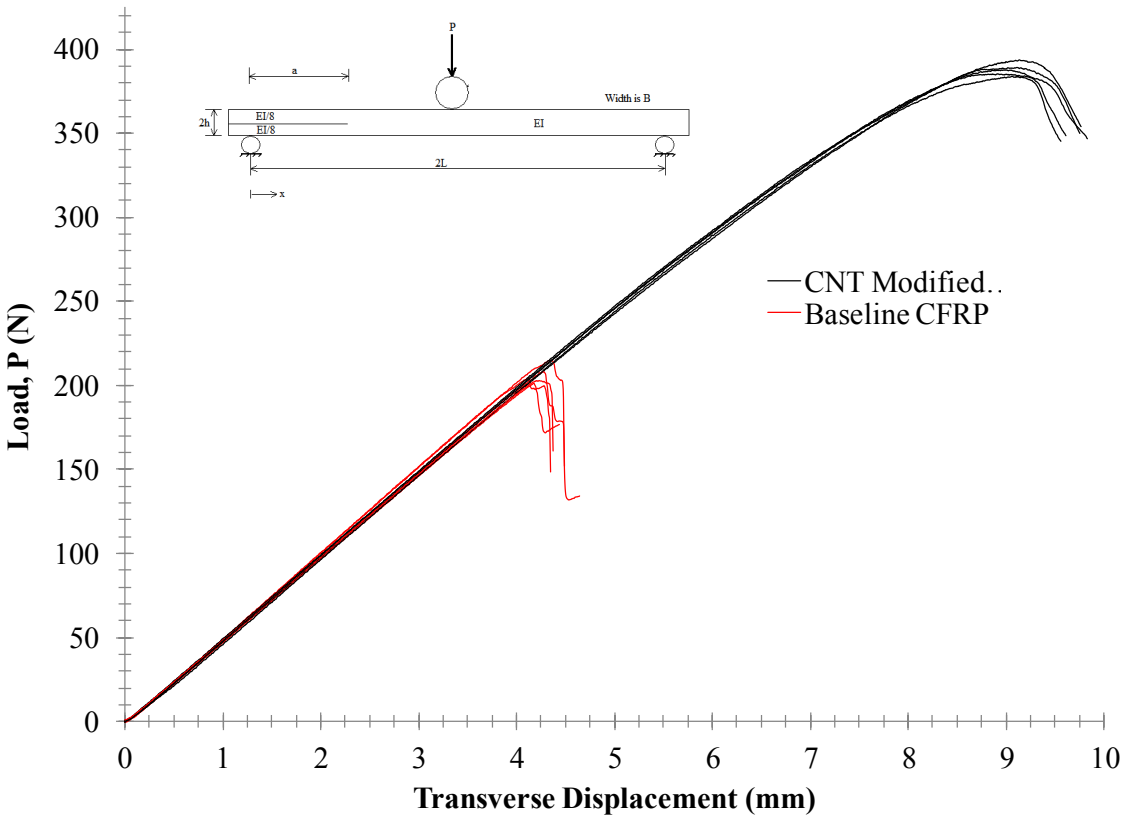

Figure 85 Applied flexural load versus central span deflection for the baseline CFRP and CNT enhanced CFRP for ENF experiments before elastic unloading.

In order to visualize the nature of the response for each of these material systems with more insight, the plot of Figure 86 has been developed to consider the resulting stiffness at each coordinate point from the load-deflection data. This allows the instantaneous stiffness to be closely examined for deviations from linearity. The data was plotted for all deflections beyond 1 mm of deflection, without considering the noisy settling-in phase of the specimen and loading fixture from 0 to 1 mm. The baseline material can be seen to drop off suddenly at

approximately 4.2 mm of deflection, indicative of the catastrophic growth. The CNT enhanced system gradually decayed and rolled off from approximately 7 to 10 mm of central span deflection.

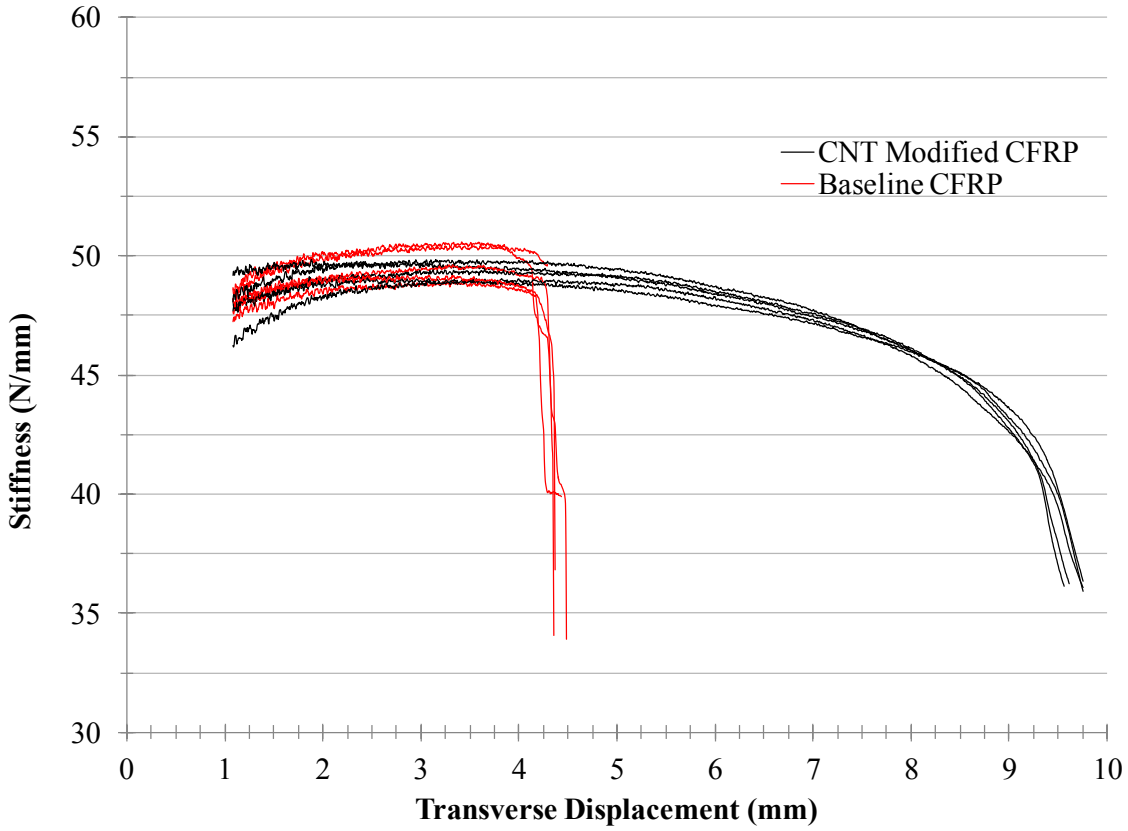

Figure 86 Resulting stiffness versus central span deflection for the baseline CFRP and CNT enhanced CFRP for ENF experiments up through peak load.

A comparison between the analytic prediction for the central span deflection given by Equation (48) and the experimental values obtained can be seen in Figure 87. The predictive relation is first order in the load, P, and results in a linear behavior. The inability to predict the central span deflection will result in inaccuracies in the prediction of G_{IIc} as a result. A correction factor could possibly be applied in order to get the deflection function to match up closer with the experimental results.

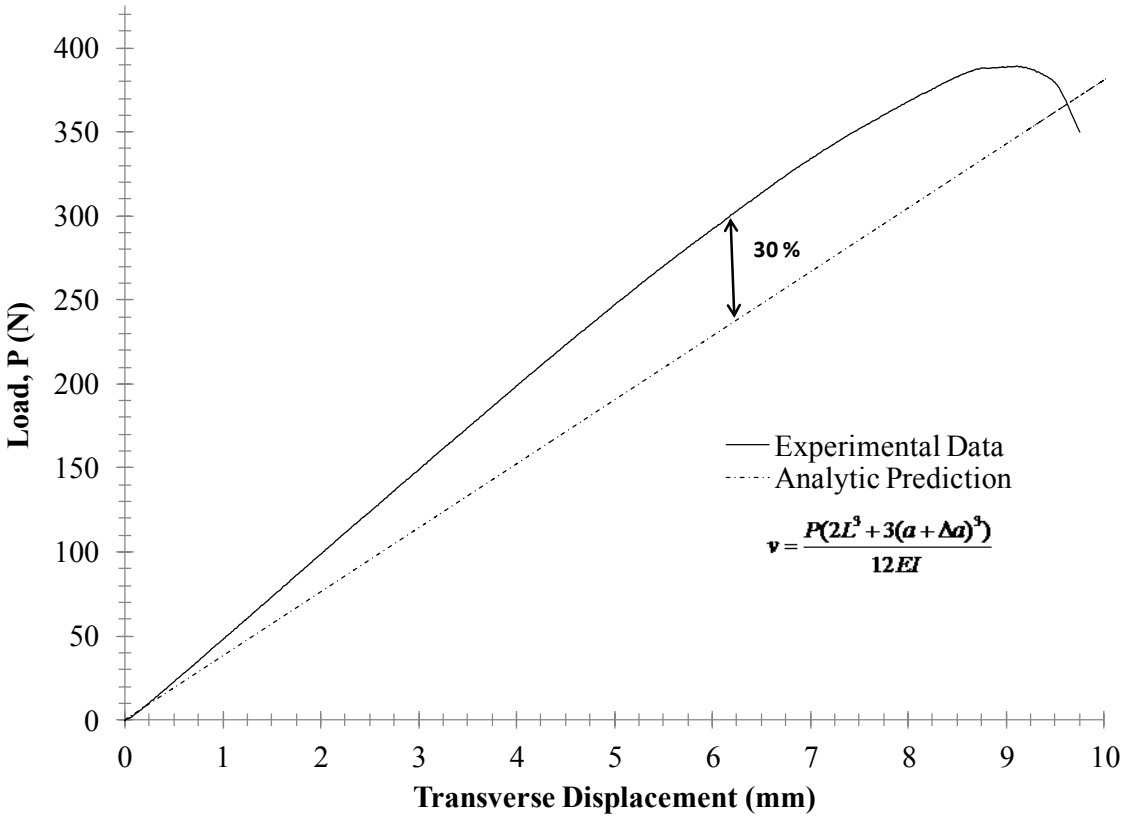

Figure 87 Comparison of analytic prediction with experimental data.

8.4.2 Crack Growth Behavior

The fracture growth is driven by the constant state of shear stress located along the mid-thickness plane. As a result of this loading scenario, there is also friction present at this interface. The relative sliding of the two halves composing the flexural specimen can be seen in Figure 88, and is the driving force for the crack growth.

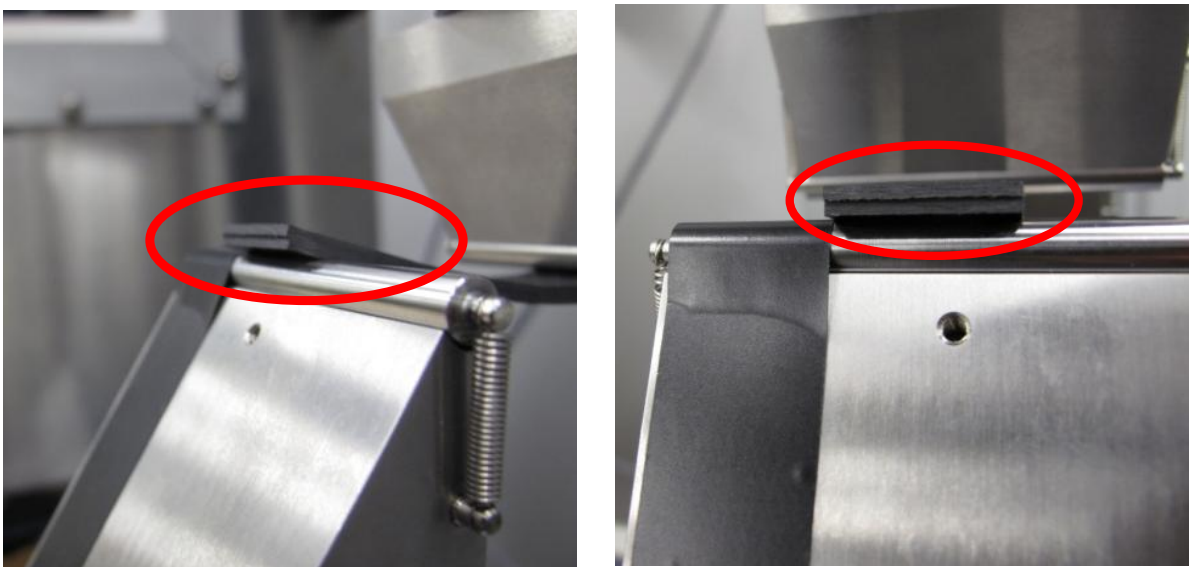

Figure 88 End notched flexure experiments in-progress showing relative sliding along beam's neutral axis.

The Teflon starter crack was identified with a microscope for each specimen and marked before testing. The fractured specimen, after testing is complete, was then optically imaged at low power to identify the extent and nature of growth. A typical starter crack and crack arrest mechanism can be seen in Figure 89. Recall, the textile used was a 8-harness satin weave which has alternating tows from the warp and weft directions causing the interface along the mid-thickness plane to appear non-planar. The fracture path was well behaved for both material types and did not jump plies or create any secondary crack front, as was observed in the DCB specimens.

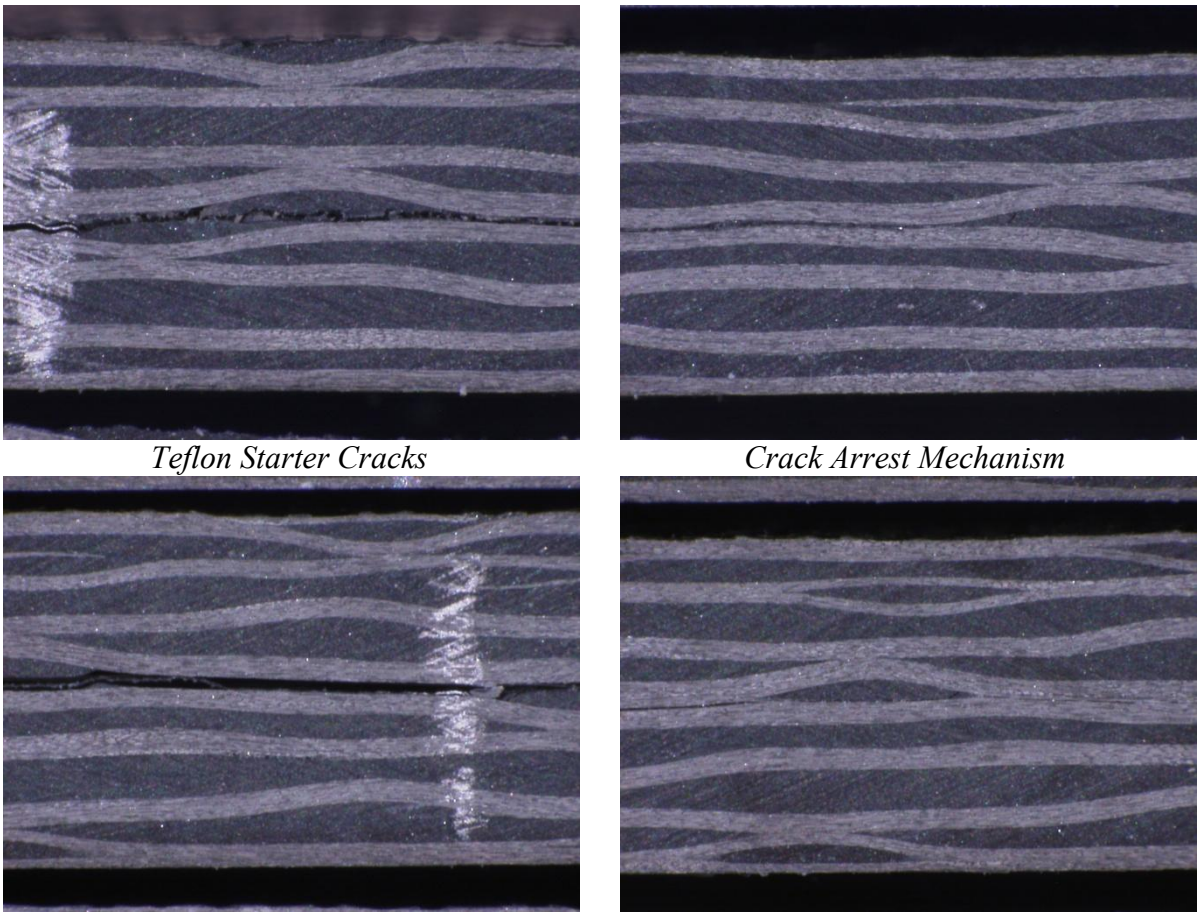

Figure 89 Teflon starter crack (left) shown for select specimens along with crack front growth and arrest behavior (right) for 2.7 mm thick specimen.

The arresting mechanism for many of the specimens was to stop at the intersection of the weft tow along the path, as shown in Figure 90. Some instances, the crack path went through the weft tow as a result of the transverse reinforcing fibers. Locating the extent of the fracture was very challenging with the fracture completely closed. Unlike the DCB experiments, where the crack growth is stable and measured in-situ with an opening specimen, the ENF experiments rely solely on microscopy on the surface for visual detection. In addition, the crack front shape is unknown and an assumption must be made to determine the area generated as a result of the crack growth.

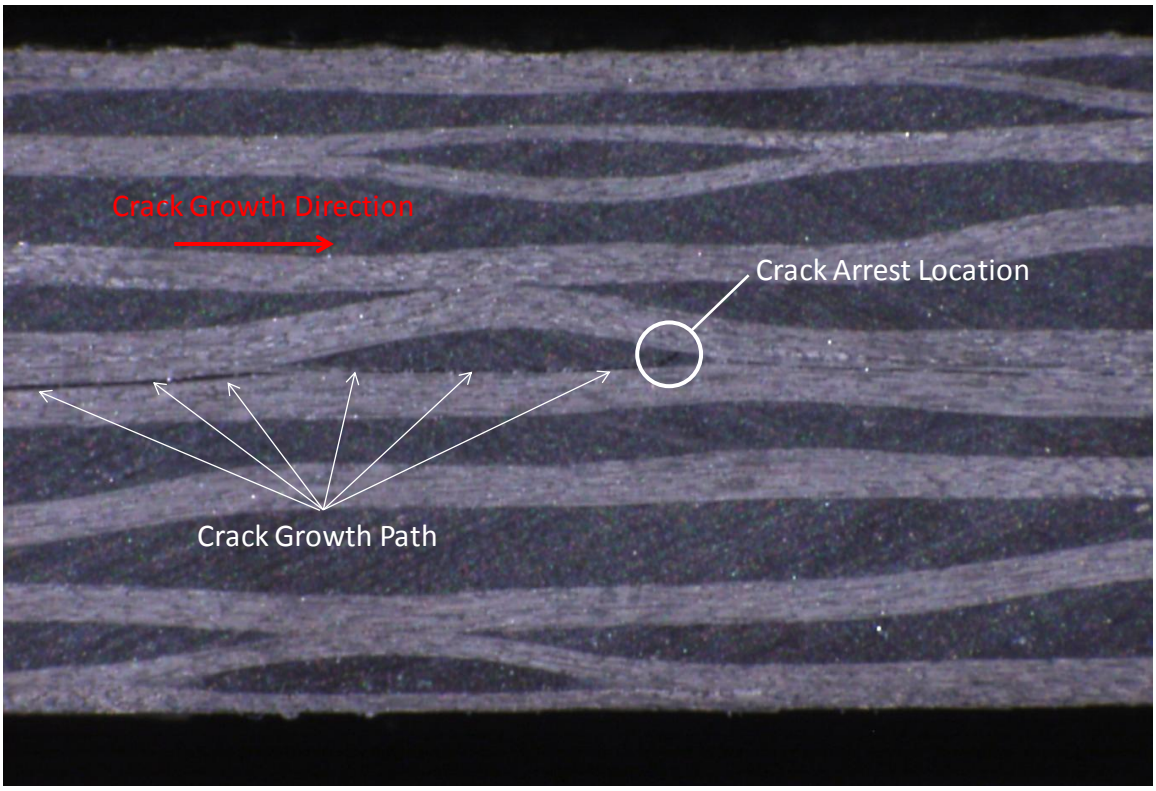

Figure 90 Micrograph showing details of crack growth behavior and arrest location for 2.7 mm thick specimen.

In order to compliment the visual measurements of the crack growth extent from the edge of the specimens, a series of ultrasonic images were obtained with a 5 MHz focused transducer. The transducer was focused on the immersed parts and maximized in terms of its return signal amplitude with gates set at both the mid-thickness plane and the back face. A typical C-scan produced from the A-scan data can be seen in Figure 91. The first echo returning from the part can be seen with the two respective gates set for the mid-thickness plane and the back face. The amplitude of the return signal is plotted with a color coding based on the signal strength. Mismatches in local impedance within the material causes the pulse wave to be reflected and transmitted. When gated at the neutral axis, the gain is set on the system to ensure the optimized signal for this plane will return approximately 80 % of the reflected wave amplitude. This is interpreted as colors on the C-scan, with the reddish regions indicative of a strong return signal amplitude. This implies that there is a discontinuity there, as expected, and the signal reflects back with minimal losses. Regions of the bluish color are indicative of weak returned signals, indicative of signal attenuation, something expected for polymeric based fiber reinforced composites. This is observed for the mid-thickness gate

where there are no cracking, and for the cracked region in the back face gate image. When gating the back face, most of the signal is reflected from the complete disbond and not much gets through to the back face. Therefore, the signal returning must pass through the disbond again, losing much, if not all, of its amplitude.

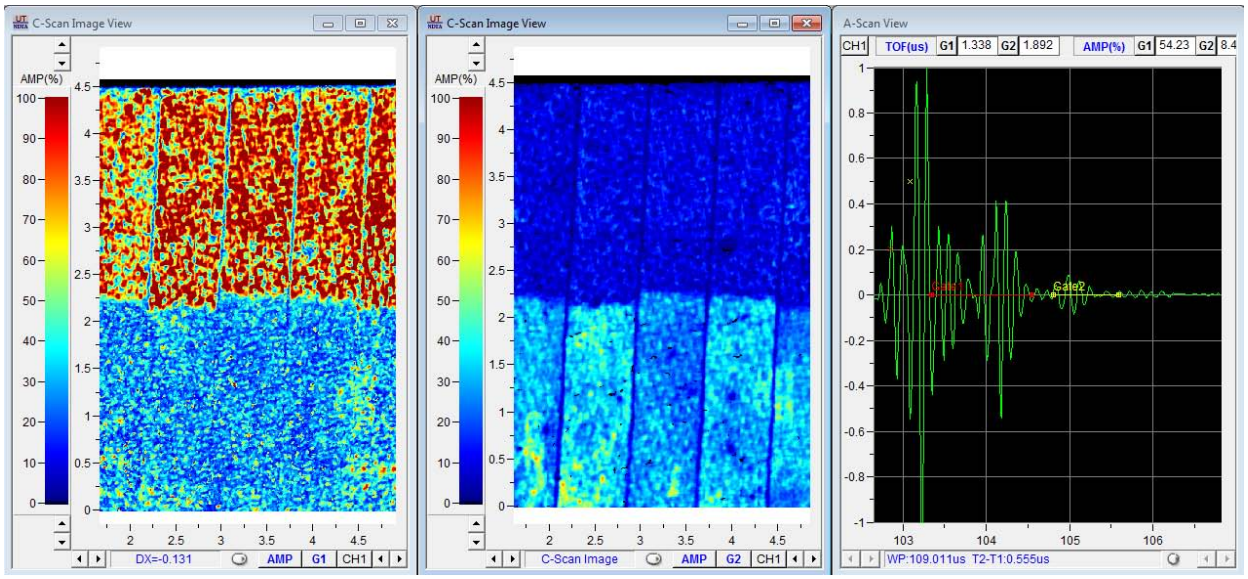

C-scan – gated at neutral axis *C-scan – gated at back face* *A-scan – first echo*

Figure 91 Resulting C-scan images based on gate location using first echo response from 10 MHz fixed focus transducer.

The resulting C-scan for all of the specimens can be seen in Figure 92. Using the U-Twin system software, the crack lengths were measured from the calibrated pixels using a double-crosshair tool. The crack fronts are relatively straight and the newly generated surface area is easily determined. In addition to the two-dimensional representation of the crack growth behavior, a three-dimensional image based on the signal amplitude to the mid-thickness plane gate has been developed, as can be seen in Figure 93. This plot serves as a useful tool to gain insight and, more specifically, spatial information with respect to flaw location through the thickness. With a fixed focus transducer, the signal is optimized using the near field transmission and knowing where the flaws are is important to get the correct standoff distance between the transducer and the work piece.

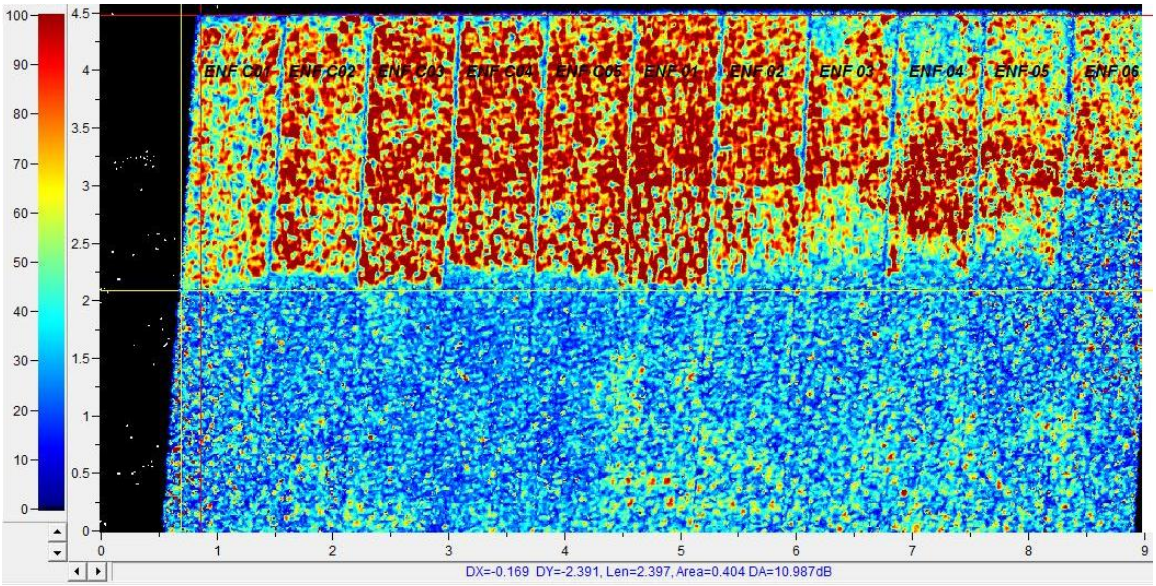

Figure 92 C-scan image of all ENF specimens after testing showing the extent and shape of fractured surface.

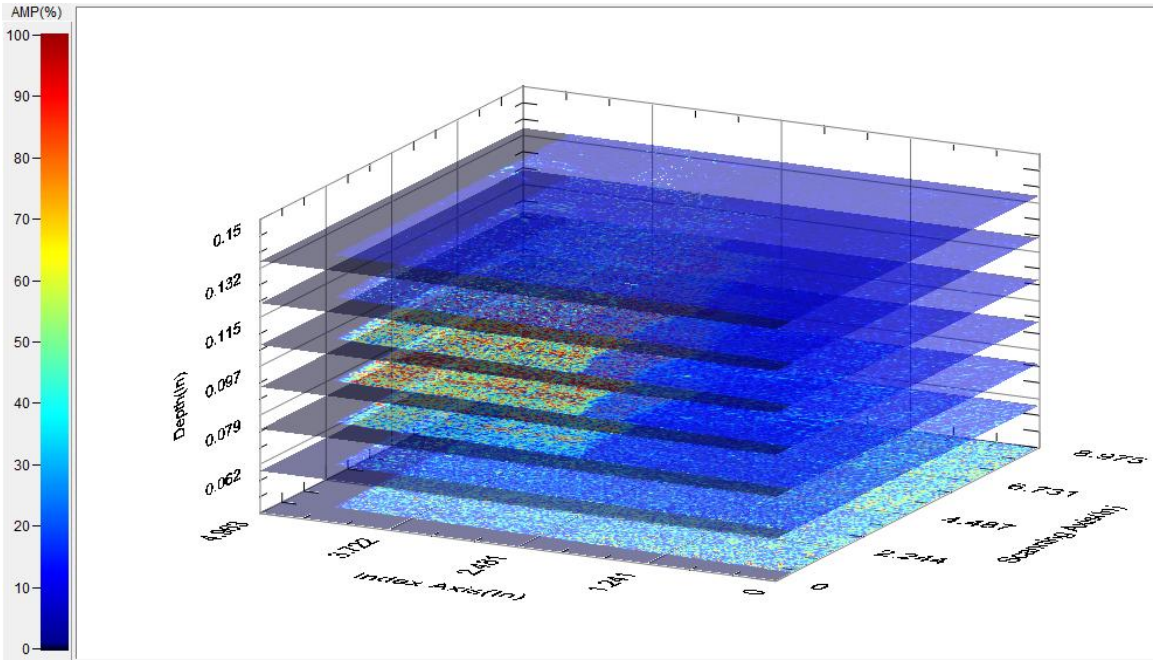

Figure 93 Three-dimensional image showing the amplitude of 10 MHz fixed focus transducer response gated on the mid-thickness interface.

Comparing the crack lengths obtained using the edge inspection technique under a microscope with the ultrasonically generated values produced variations on the order of 20 to 70 %. In each case, as might be expected, the crack lengths determined from the microscopy

was lower than the ultrasonic image generation. The specimens were immersed in water for the ultrasonic imaging, but not for more than 1 hr in room temperature water. Polymers typically absorb water and swell as a result, possibly causing some residual stress to be induced. The analysis methodology employed, therefore, will take into account each method of crack growth determination, possibly to get a lower and upper bound. It is unlikely that the moisture drove the cracks to significantly grow with such a short exposure. The more likely explanation is the inability to discern the final arrest of the fracture path under a microscope.

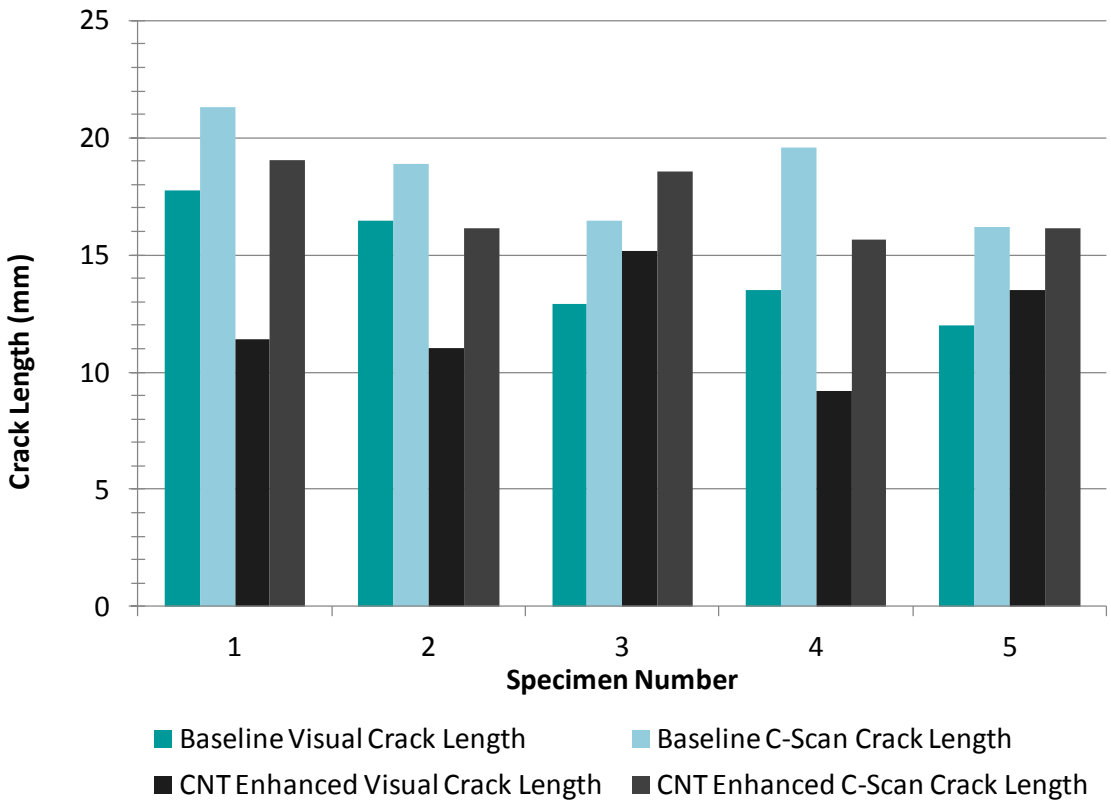

Figure 94 Comparison between visual edge measured crack lengths and ultrasonic C-scan measured crack lengths.

8.4.3 Energy Absorption

In order to effectively use the load-deflection response curves, the specimens were unloaded after the fracture growth event occurred. This elastic recovery unload event allows the delineation between the work done to create new fracture surfaces and that of purely elastic deformation. The unload also shows if any residual deformation is present. By unloading

until the force is non-existent, allows the deflection to settle in to a final resting location. This is the residual deflection amount, and only the CNT modified specimens appear to have non-zero values, which average at about 250 µm.

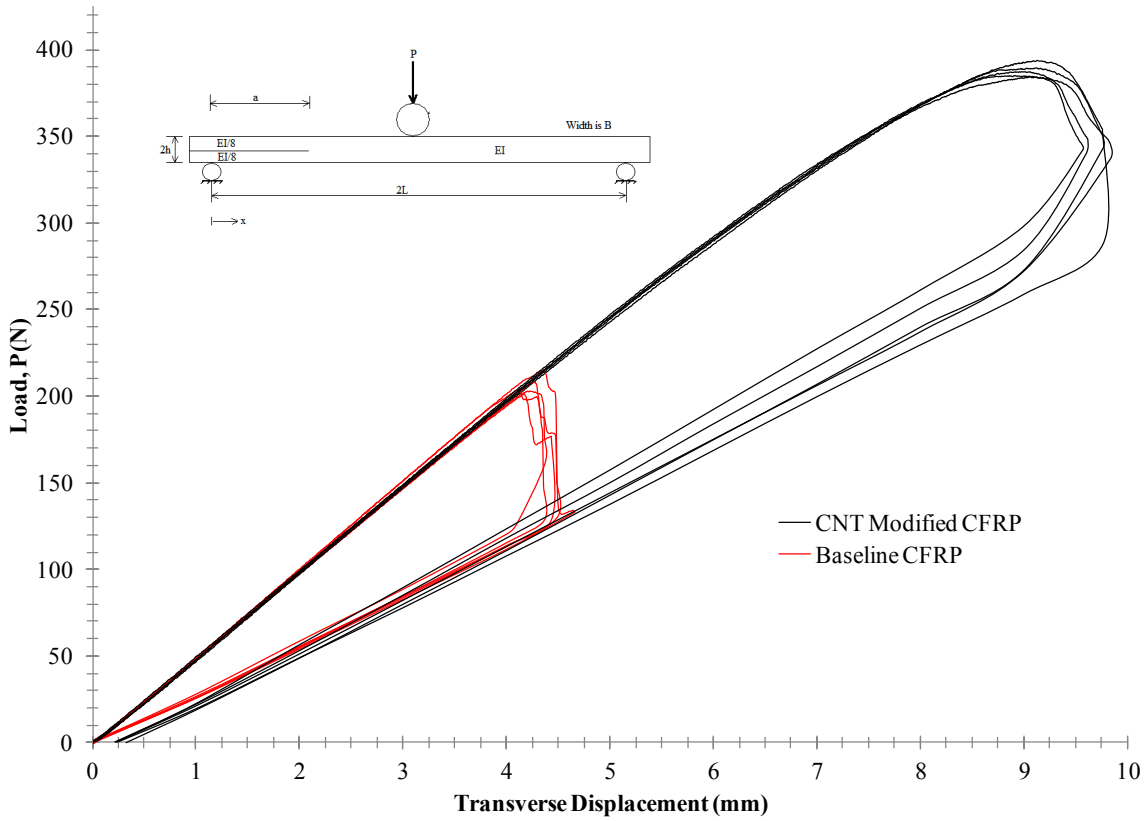

Figure 95 Applied flexural load versus central span deflection for the baseline CFRP and CNT enhanced CFRP for ENF experiments including the elastic unloading.

Integrating the force-deflection response, similar to that shown in Figure 53, all the way through the elastic unload allows the determination of the energy associated with the generation of new surface area. This energy can then be used with the crack length measurements to calculate G_{IIc}. The shaded regions of Figure 96 represent the work done in order to load, grow the crack, and then unload the specimen.

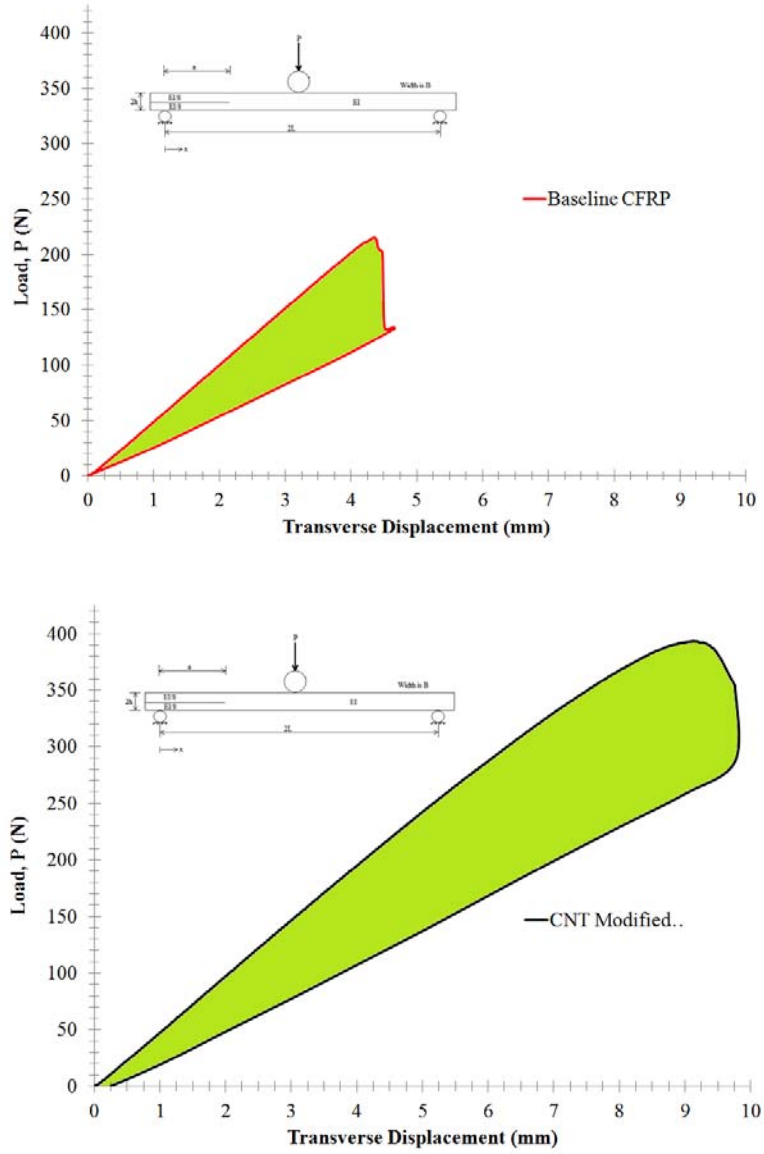

Figure 96 Integrated area representing energy absorbed to create new fracture surface for baseline CFRP (above) and CNT enhanced CFRP specimen (below).

The energy absorbed, calculated through a mid-point rule numerical integration scheme, increases at an increasing rate until the maximum load is achieved. The unloading then removes the elastically stored energy from the cumulative summation. This is illustrated in the plots of Figure 97 for both material systems of interest. The final values at the vertical intercepts have been tabulated for each specimen and the CNT modified specimens have absorbed roughly 267 % more energy for the fracture growth process. This calculated energy will be used for the Area Method to determine the Mode II strain energy release rates.

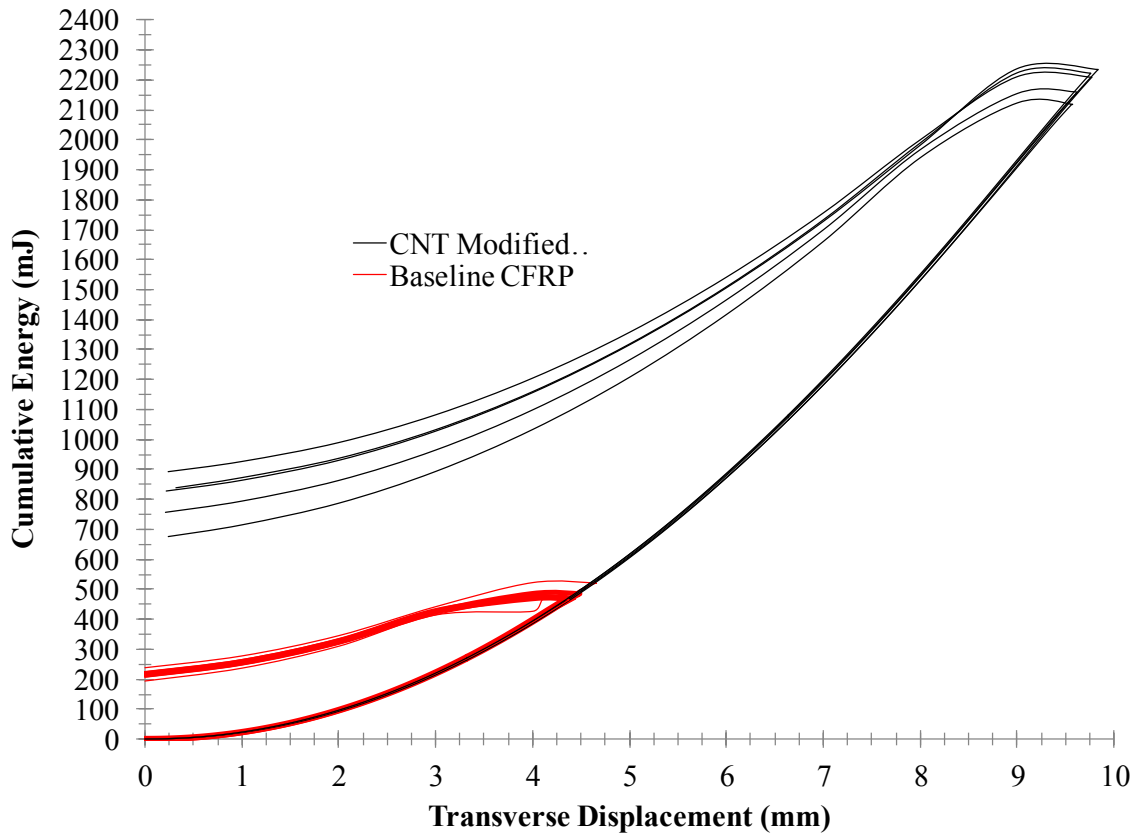

Figure 97 Cumulative energy absorbed versus central span deflection for the baseline CFRP and CNT enhanced CFRP for ENF experiments including the elastic unloading.

8.4.4 Critical Mode II Strain Energy Release Rate

Calculation of the critical strain energy release rate using the energy method is straightforward. Using the relation

$$G_{IIc} = \frac{\Delta U}{B\Delta a} \tag{80}$$

The work done, ΔU, is determined from the numerical integration and the crack length, Δa, is measured. The results can be seen in Figure 98 for both the CNT modified CFRP and the baseline CFRP material for both cases of the visual measured crack lengths using a microscope and for the C-scan ultrasonic determination.

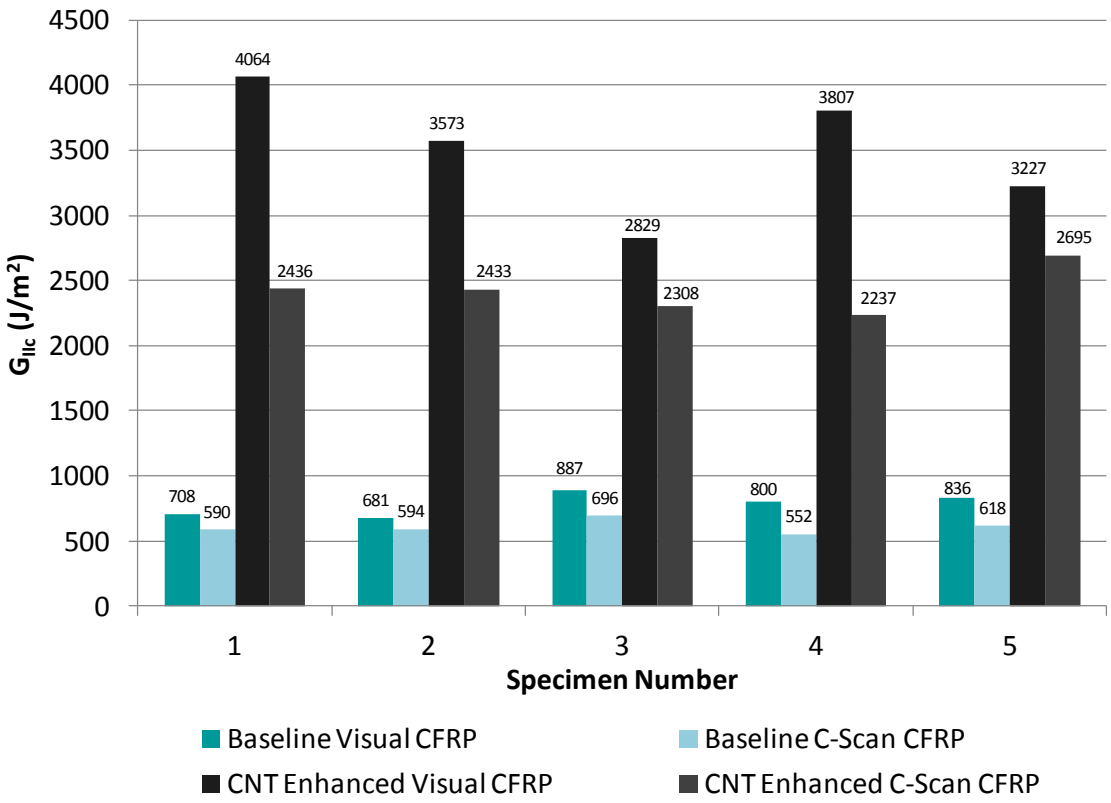

Figure 98 Resulting Mode II strain energy release rates as a function of crack length measuring method.

With the strain energy release rates under Mode II loading determined by both approaches using the integrated energy, the microscopic determination of crack area method can be seen to overestimate the critical release rate for both material types. This is to be expected as a result of the shorter crack lengths obtained since the energy was the same for each individual case by using Equation (80). The overestimate is on the order of 52 % for the CNT enhanced material system and 28 % for the baseline CFRP. The average values for the baseline CFRP using the microscopy and C-scan measurement techniques are 782 J/m^2 and 610 J/m^2, respectively. The standard deviation for the baseline material system was approximately 11 % and 9 % with respect to the average G_{IIc} values, respectively, for the microscopy and ultrasonic crack length determination. The average values for the CNT modified CFRP using the microscopy and C-scan measurement techniques are 3568 J/m^2 and 2354 J/m^2, respectively. For the CNT modified material system, the deviation was approximately 15 % and 4 % for the microscopy and C-scan measurement methods, respectively.

To compare the experimentally measured results using the integrated energy with the analytic development above in 8.2, the plot in Figure 99 and Figure 100 have been created. Using the result of Equation (67), and the on setting instability loads from the load-deflection response from Figure 85, the predictions can be calculated. For all, the modulus was taken as 58 GPa which is the experimentally measured extensional modulus in the warp direction. For the baseline CFRP, the analytic predictions are on average 59 % and 137 % higher than the area method of integration for the microscopy versus ultrasonic determined crack lengths, respectively.

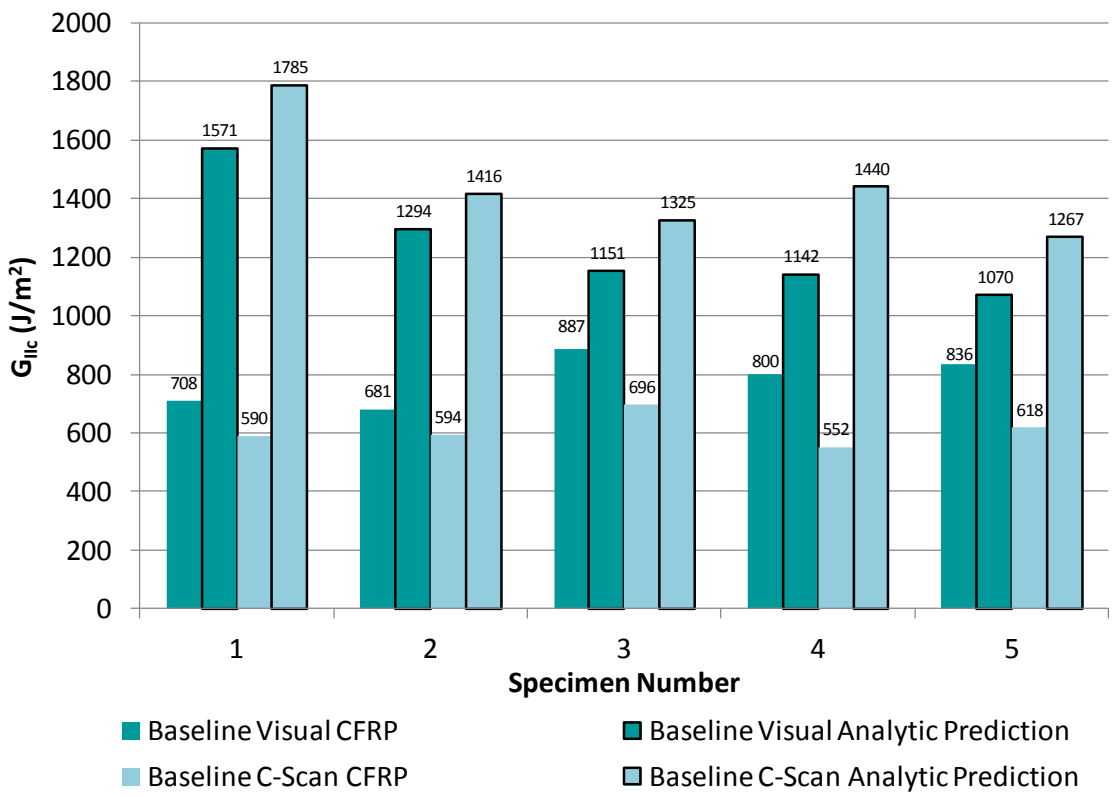

Figure 99 Mode II strain energy release rate experimental values for baseline CFRP material compared with analytic predictions using Equation (67).

Considering the CNT modified CFRP, the analytic prediction for the microscopy measured crack lengths was on average within 2 % of the experimentally determined value using the area method of integration with the maximum peak load for the instability condition. Using a lower bound load level found from the reduction in stiffness, as shown in Figure 86, and defining the instability load to have occurred when the stiffness drops below 50 N/mm, the

prediction then becomes 24 % lower for the microscopy determined crack lengths. The analytic prediction for the C-scan determined crack lengths was found to be on average 94 % higher than the area integration method for the CNT enhanced CFRP specimens. Using the reduced load tangent method, when the stiffness reduces below 50 N/mm, the analytic prediction then over predicts by 44 %.

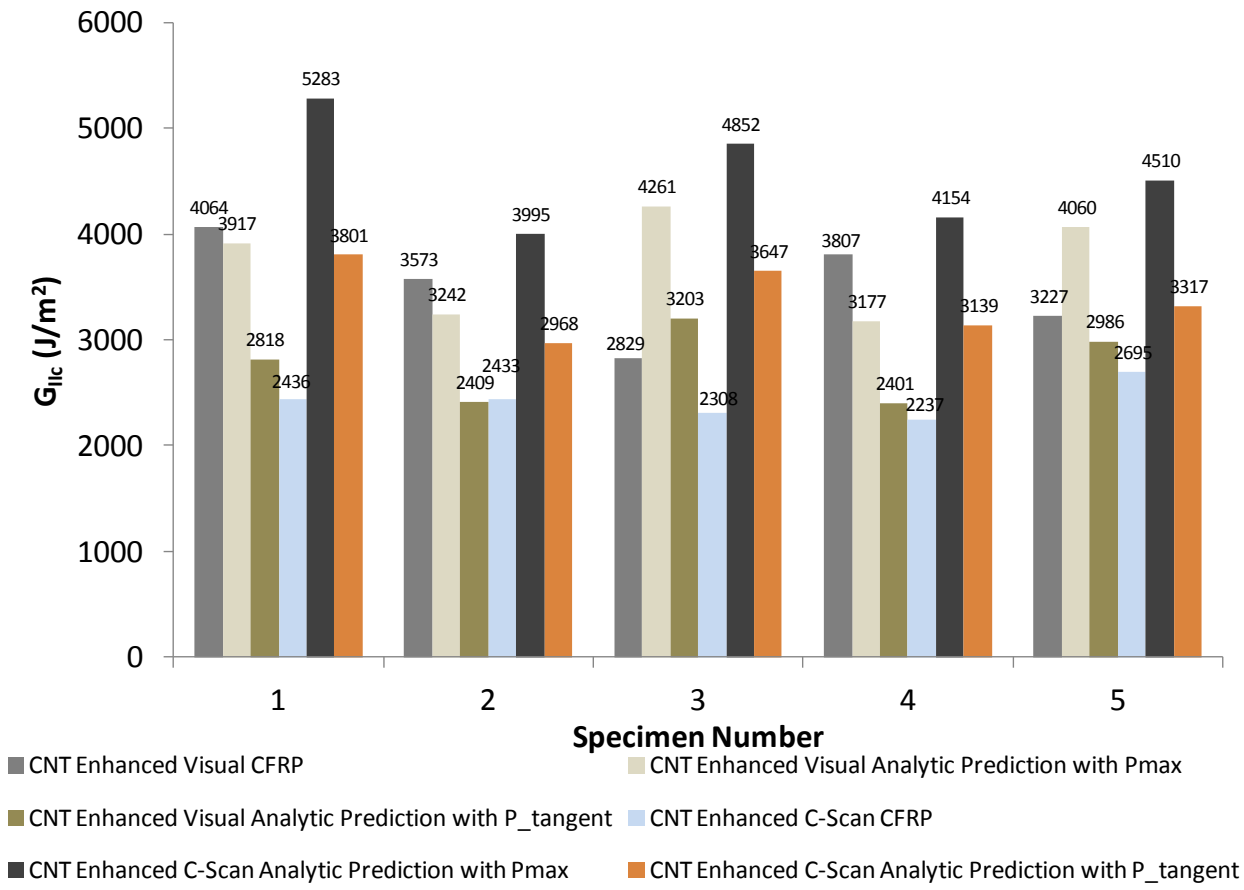

Figure 100 Mode II strain energy release rate experimental values for CNT enhanced CFRP material compared with analytic predictions using Equation (67).

8.5 Conclusions

An investigation into the Mode II fracture behavior for a baseline CFRP and CNT modified CFRP material system has been conducted in order to determine the critical strain energy release rate. The findings of this study are as follows:

- The maximum load achieved prior to significant crack growth was found to be 88 % higher for the CNT modified CFRP. In addition, approximately 267 % more energy was imparted to the crack growth process for the CNT modified CFRP.

- The baseline CFRP material underwent a catastrophic load drop while the CNT modified CFRP exhibited a roll off behavior in terms of the instantaneous stiffness reduction.

- The measured crack lengths using edge microscopy were upwards of 70 % different than that determined from ultrasonics. The microscopic determined crack lengths were consistently lower in value than the C-scans, resulting in higher G_{IIc} values compared with that from the C-scan crack lengths.

- The crack lengths measured with the C-scan for the CNT modified specimens correlated well with only a 4 % standard deviation.

- Analytic predictions did not agree well with experimental values measured. This is predominantly associated with the inability to predict the displacement within an acceptable range. A correction factor may be applied to get better correlation.

This page left intentionally blank.

9 SUMMARY, CONCLUSIONS AND RECOMMENDATIONS

9.1 Summary and Conclusions

An extensive experimental investigation into the characterization of a CNT enhanced carbon fiber reinforced polymer composite material has been performed. Experimental characterization has included thermal analytical analysis, dynamic mechanical analysis, Mode I fracture testing, Mode II fracture testing, finite element simulations, and the development of a new depositional technique for the homogeneous dispersion of CNTs onto a composite material. In addition, analytical models have been derived and utilized for additional insight in order to delineate the material properties that govern the response from the extrinsic boundary values that influence it.

Based on this comprehensive investigation, the following significant conclusions have been made:

1. CNTs can be adequately dispersed onto an uncured polymeric composite substrate through an electrospinning technique with adequate process parameters chosen.
2. The exothermic reaction during the cure is affected by the presence of a secondary polymer substrate acting as the transport medium for the CNTs.
3. The glass transition temperature, storage modulus, and Tan Delta are all measurably different from the baseline CFRP and the CNT enhanced system.
4. The Mode I fracture strain energy release rate for the CNT enhanced system is far superior over the baseline CFRP material system. The fracture morphology shows considerable differences associated with the energy absorbing mechanisms.
5. The Mode II fracture strain energy release rate for the CNT enhanced system is far superior over the baseline CFRP material system. The crack length determinations were found to be more reliable using ultrasonics rather than optical edge inspection.
6. Finite element simulations proved useful for gaining insight and explaining the mechanisms associated with the complex fracture process observed during double cantilever beam experiments.

9.2 Future Recommendations

On the basis of this present investigation, the following studies are recommended for future work:

1. Investigation of the state of phase for the PVDF-HFP polymer at respective points in time during processing and testing. Correlating this phase to the measured response.

2. Perform a study in order to elucidate the effects of doping a traditional composite with a thermoplastic toughening polymer versus the improvement by adding CNT enhancement.

3. Perform a study isolating the CNTs with a variety of different polymeric substrate transport mediums to optimize the load transmission and interfacial adhesion.

4. Investigate the effects for a variation in CNT weight percent versus mechanical performance improvements.

5. Expand this study to understand the implications of CNT doping on composite materials under adverse loading conditions involving temperature and strain rate variation.

6. Develop a technique for in-situ observation of the fracture process at an appropriate length scale to define the mechanisms of energy absorption arising from the CNTs.

7. Expand this concept for the development of a nano-enhanced resin formulation that can either prepreg a structural composite fabric or be used for resin infusion systems.

10 REFERENCES

[1] Garcia, E. J., Wardle, B. L., Hart, A. J., Yamamoto, N., *Fabrication and multifunctional properties of a hybrid laminate with aligned carbon nanotubes grown in situ*, Composite Science and Technology, 68 (2008) 2034-2041.

[2] Zhu, J., Imam, A., Crane, R., Lozano, K., Khabashesku, V. N., Barrera, E. V., *Processing a glass fiber reinforced vinyl ester composite with nanotube enhancement of interlaminar shear strength*, Composites Science and Technology, 67 (2007) 1509-1517.

[3] Kelkar, A. D., Mohan, R., Bolick, R., Shendokar, S., Effect of nanopaticles and nanofibers on Mode I fracture toughness of fiber glass reinforced polymeric matrix composites, Materials Science and Engineering B, 168 (2010) 85-89.

[4] Kim, G. M., Michler, G. H., Potschke, P., Deformation processes of ultrahigh porous multiwalled carbon nanotubes/polycarbonate composite fibers prepared by electrospinning, Polymer, 46 (2005) 7346-7351.

[5] Kelkar, A. D., Mohan, Bolick, R., Shendokar, S., *Effect of electrospun fibers on the interlaminar properties of woven composites*, Advanced Materials Research Vols., 47-50 (2008) 1031-1034.

[6] Qian, D., Dickey, E. C., Andrews, R., Rantell, T., *Load transfer and deformation mechanisms in carbon nanotube-polstyrene composites*, Applied Physics Letters, 76/20 (2000) 2868-2870.

[7] Grimmer, C. S., Dharan, C. K. H., Enhancement of delamination fatigue resistance in carbon nanotube reinforced glass fiber/polymer composites, Composite Science and Technology, 70 (2010) 901-908.

[8] Faulkner, S. D., Kwon, Y. W., Bartlett, S., Rasmussen, E. A., *Study of composite joint strength with carbon nanotube reinforcement*, Journal of Material Science, 44 (2009) 2858-2864.

[9] Garcia, E. J., Wardle, B. L., Hart, A. J., *Joining prepreg composite interfaces with aligned carbon nanotubes*, Composites: Part A, 39 (2008) 1065-1070.

[10] Han, J. T., Cho, K., Nanoparticle-induced enhancement in fracture toughness of highly loaded epoxy composites over a wide temperature range, Journal of Material Science, 41 (2006) 4239-4245.

[11] Zheng-Ming Huang, Y.-Z. Zhang, M. Kotaki, S. Ramakrishna, ―A review on polymer nanofibers by electrospinning and their applications in nanocomposites*”*, *Composites Science and Technology*, Volume 63, Issue 15, 2003, 2223-2253.

[12] Ioannis S. Chronakis, ―Novel nanocomposites and nano-ceramics based on polymer nanofibers using electrospinning process—A review*”*, *Journal of Materials Processing Technology*, Volume 167, Issues 2–3, 30 August 2005, 283-293.

[13] Jayesh Doshi, Darrell H. Reneker, ―Electrospinning process and applications of electrospun fibers*", Journal of Electrostatics*, Volume 35, Issues 2–3, 1995, 151-160.

[14] D. Aussawasathien, C. Teerawattananon, A. Vongachariya, ―Separation of micron to sub-micron particles from water: Electrospun nylon-6 nanofibrous membranes as pre-filters*"*, *Journal of Membrane Science*, Volume 315, Issues 1–2, 2008, 11-19.

[15] Renuga Gopal, Satinderpal Kaur, Chao Yang Feng, Casey Chan, Seeram Ramakrishna, Shahram Tabe, Takeshi Matsuura, ―Electrospun nanofibrous polysulfone membranes as pre-filters: Particulate removal*"*, *Journal of Membrane Science*, Volume 289, 2007, 210-219.

[16] Ki Myoung Yun, Christopher J. Hogan Jr., Yasuko Matsubayashi, Masaaki Kawabe, Ferry Iskandar, Kikuo Okuyama, ―Nanoparticle filtration by electrospun polymer fibers*"*, *Chemical Engineering Science*, Volume 62, 2007, 4751-4759.

[17] Xiao-Hong Qin,Shan-Yuan Wang, ―Filtration properties of electrospinning nanofibers*"*, *Journal of Applied Polymer Science*, Volume 102, Issue 2, 2006, 1285–1290.

[18] Dehai Liang, Benjamin S. Hsiao, Benjamin Chu, ―Functional electrospun nanofibrous scaffolds for biomedical applications*"*, *Advanced Drug Delivery Reviews*, Volume 59, Issue 14, 2007, 1392-1412.

[19] Kwangsok Kim, Meiki Yu, Xinhua Zong, Jonathan Chiu, Dufei Fang, Young-Soo Seo, Benjamin S. Hsiao, Benjamin Chu, Michael Hadjiargyrou, ―Control of degradation rate and hydrophilicity in electrospun non-woven poly(d,l-lactide) nanofiber scaffolds for biomedical applications*"*, *Biomaterials*, Volume 24, Issue 27, 2003, 4977-4985.

[20] Zhu, J., Imam, A., Crane, R., Lozano, K., Khabashesku, V. N., Barrera, E. V., ―Processing a glass fiber reinforced vinyl ester composite with nanotube enhancement of interlaminar shear strength*"*, *Composites Science and Technology*, 67 (2007) 1509-1517.

[21] Kelkar, A. D., Mohan, R., Bolick, R., Shendokar, S., ―Effect of nanopaticles and nanofibers on Mode I fracture toughness of fiber glass reinforced polymeric matrix composites*"*, *Materials Science and Engineering B*, 168 (2010) 85-89.

[22] Kim, G. M., Michler, G. H., Potschke, P., ―Deformation processes of ultrahigh porous multiwalled carbon nanotubes/polycarbonate composite fibers prepared by electrospinning*"*, *Polymer*, 46 (2005) 7346-7351.

[23] Kelkar, A. D., Mohan, Bolick, R., Shendokar, S., ―Effect of electrospun fibers on the interlaminar properties of woven composites*"*, *Advanced Materials Research* Vols., 47-50 (2008) 1031-1034.

[24] Qian, D., Dickey, E. C., Andrews, R., Rantell, T., ―Load transfer and deformation mechanisms in carbon nanotube-polystyrene composites*”*, *Applied Physics Letters*, 76/20 (2000) 2868-2870.

[25] Grimmer, C. S., Dharan, C. K. H., ―Enhancement of delamination fatigue resistance in carbon nanotube reinforced glass fiber/polymer composites*”*, *Composite Science and Technology*, 70 (2010) 901-908.

[26] Z. F. Ren, Z. P. Huang, J. W. Xu, J. H. Wang, P. Bush, M. P. Siegal and P. N. Provencio, ―Synthesis of Large Arrays of Well-Aligned Carbon Nanotubes on Glass*”*, *Science 6*, 1998, Vol. 282,1105-1107.

[27] De-Chang Li, Liming Dai, Shaoming Huang, Albert W.H. Mau, Zhong L. Wang, ―Structure and growth of aligned carbon nanotube films by pyrolysis*”*, *Chemical Physics Letters*, Volume 316, Issues 5–6, 2000, 349-355.

[28] C.A. Martin, J.K.W. Sandler, A.H. Windle, M.-K. Schwarz, W. Bauhofer, K. Schulte, M.S.P. Shaffer, ―Electric field-induced aligned multi-wall carbon nanotube networks in epoxy composites*”*, *Polymer,* Volume 46, Issue 3, 2005, 877-886.

[29] Park, C., Wilkinson, J., Banda, S., Ounaies, Z., Wise, K. E., Sauti, G., Lillehei, P. T. and Harrison, J. S. (2006), ―Aligned single-wall carbon nanotube polymer composites using an electric field*”, J. Polym. Sci. B Polym. Phys.*, 44: 1751–1762.

[30] M. Senthil Kumar, S.H. Lee, T.Y. Kim, T.H. Kim, S.M. Song, J.W. Yang, K.S. Nahm, E.-K. Suh, ―DC electric field assisted alignment of carbon nanotubes on metal electrodes*”*, *Solid-State Electronics*, Volume 47, Issue 11, 2003, 2075-2080.

[31] Gang Li, Peng Li, Yunhua Yu, Xiaolong Jia, Shen Zhang, Xiaoping Yang, Seungkon Ryu, ―Novel carbon fiber/epoxy composite toughened by electrospun polysulfone nanofibers*”*, *Materials Letters*, Volume 62, Issue 3, 2008, 511-514.

[32] Garcia, E. J., Wardle, B. L., Hart, A. J., Yamamoto, N., ―Fabrication and multifunctional properties of a hybrid laminate with aligned carbon nanotubes grown in situ*”*, *Composite Science and Technology*, 68 (2008) 2034-2041.

[33] Deitzel, J. M., Kleinmeyer, J. D., Hirvonen, J. K., Tan, N. C., ―Controlled deposition of electrospun poly(ethelyne oxide) fibers*”*, *Polymer* 42 (2001) 8163-8170.

[34] Seoul, C., Kim, Y.-T. and Baek, C.-K., ―Electrospinning of poly(vinylidene fluoride)/dimethylformamide solutions with carbon nanotubes*”, J. Polym. Sci. B Polym. Phys.*, 41: 2003, 1572–1577.

[35] Leslie Y. Yeo, James R. Friend, ―Electrospinning carbon nanotube polymer composite nanofibers*”*, *Journal of Experimental Nanoscience*, Vol. 1, 2006, 177-209.

[36] Tsu-Wei Chou, Limin Gao, Erik T. Thostenson, Zuoguang Zhang, Joon-Hyung Byun, ―An assessment of the science and technology of carbon nanotube-based fibers and composites*”*, *Composites Science and Technology*, Volume 70, Issue 1, 2010, 1-19.

[37] Crane, L. W., Dynes, P. J. and Kaelble, D. H. (1973), Analysis of curing kinetics in polymer composites. J. Polym. Sci. B Polym. Lett. Ed., 11: 533–540, 1973.

[38] Maria Inez G. de Miranda, Cassia Tomedi, Clara I.D. Bica, Dimitrios Samios, A d.s.c. kinetic study on the effect of filler concentration on crosslinking of diglycidylether of bisphenol-A with 4,4′-diaminodiphenylmethane, Polymer, Volume 38, Issue 5, March 1997, Pages 1017-1020.

[39] Hai-Ping Xu, Zhi-Min Dang, Electrical property and microstructure analysis of poly(vinylidene fluoride)-based composites with different conducting fillers, Chemical Physics Letters, Volume 438, Issues 4–6, 20 April 2007, Pages 196-202.

[40] A. Salimi, A.A. Yousefi, Analysis Method: FTIR studies of β-phase crystal formation in stretched PVDF films, Polymer Testing, Volume 22, Issue 6, September 2003, Pages 699-704.

[41] V. Sencadas, S. Lanceros-Méndez, J.F. Mano, Characterization of poled and non-poled β-PVDF films using thermal analysis techniques, Thermochimica Acta, Volume 424, Issues 1–2, 15 December 2004, Pages 201-207.

[42] Gernot M. Wallner, Zoltan Major, Günther A. Maier, Reinhold W. Lang, Fracture analysis of annealed PVDF films, Polymer Testing, Volume 27, Issue 3, May 2008, Pages 392-402.

[43] Menard, K. P. 2004. Dynamic Mechanical Analysis. Encyclopedia Of Polymer Science and Technology.

[44] Dong, S. and Gauvin, R. (1993), Application of dynamic mechanical analysis for the study of the interfacial region in carbon fiber/epoxy composite materials. Polym Compos, 14: 414–420.

[45] Thomason, J. L. (1990), Investigation of composite interphase using dynamic mechanical analysis: Artifacts and reality. Polym Compos, 11: 105–113.

[46] N. Klein, G. Marom, A. Pegoretti, C. Migliaresi, Determining the role of interfacial transcrystallinity in composite materials by dynamic mechanical thermal analysis, Composites, Volume 26, Issue 10, 1995, Pages 707-712.

[47] Zhaoxia Jin, K.P. Pramoda, Guoqin Xu, Suat Hong Goh, Dynamic mechanical behavior of melt-processed multi-walled carbon nanotube/poly(methyl methacrylate) composites, Chemical Physics Letters, Volume 337, Issues 1–3, 30 March 2001, Pages 43-47.

[48] H.W Goh, S.H Goh, G.Q Xu, K.P Pramoda, W.D Zhang, Dynamic mechanical behavior of in situ functionalized multi-walled carbon nanotube/phenoxy resin

composite, Chemical Physics Letters, Volume 373, Issues 3–4, 20 May 2003, Pages 277-283.

[49] Shuying Yang, Jaime Taha-Tijerina, Verónica Serrato-Diaz, Krystal Hernandez, Karen Lozano, Dynamic mechanical and thermal analysis of aligned vapor grown carbon nanofiber reinforced polyethylene, Composites Part B: Engineering, Volume 38, Issue 2, March 2007, Pages 228-235.

[50] Anderson, T. L., Fracture Mechanics, Fundamentals and Applications, Second Edition, CRC Press, New York, 1995.

[51] P. Zhang, H. Jiang, Y. Huang, P.H. Geubelle, K.C. Hwang, An atomistic-based continuum theory for carbon nanotubes: analysis of fracture nucleation, Journal of the Mechanics and Physics of Solids, Volume 52, Issue 5, May 2004, Pages 977-998.

[52] A. Tugrul Seyhan, Metin Tanoglu, Karl Schulte, Mode I and mode II fracture toughness of E-glass non-crimp fabric/carbon nanotube (CNT) modified polymer based composites, Engineering Fracture Mechanics, Volume 75, Issue 18, December 2008, Pages 5151-5162.

[53] F.H. Gojny, M.H.G. Wichmann, U. Köpke, B. Fiedler, K. Schulte, Carbon nanotube-reinforced epoxy-composites: enhanced stiffness and fracture toughness at low nanotube content, Composites Science and Technology, Volume 64, Issue 15, November 2004, Pages 2363-2371.

[54] Martin Ganß, Bhabani K. Satapathy, Mahendra Thunga, Roland Weidisch, Petra Pötschke, Dieter Jehnichen, Structural interpretations of deformation and fracture behavior of polypropylene/multi-walled carbon nanotube composites, Acta Materialia, Volume 56, Issue 10, June 2008, Pages 2247-2261.

[55] Barber, A. H., Cohen, S. R., Eitan, A., Schadler, L. S. and Wagner, H. D. (2006), Fracture Transitions at a Carbon-Nanotube/Polymer Interface. Adv. Mater., 18: 83–87.

[56] Florian H Gojny, Jacek Nastalczyk, Zbigniew Roslaniec, Karl Schulte, Surface modified multi-walled carbon nanotubes in CNT/epoxy-composites, Chemical Physics Letters, Volume 370, Issues 5–6, 21 March 2003, Pages 820-824.

[57] Lourie, O.; Wagner, H. D.; , "Transmission electron microscopy observations of fracture of single-wall carbon nanotubes under axial tension," Applied Physics Letters , vol.73, no.24, pp.3527-3529, Dec 1998.

[58] O. Lourie, H.D. Wagner, Evidence of stress transfer and formation of fracture clusters in carbon nanotube-based composites, Composites Science and Technology, Volume 59, Issue 6, May 1999, Pages 975-977.

[59] Bower, C.; Rosen, R.; Jin, L.; Han, J.; Zhou, O.; , "Deformation of carbon nanotubes in nanotube–polymer composites," Applied Physics Letters , vol.74, no.22, pp.3317-3319, May 1999.

[60] Smiley, A. J., Pipes, R. B., ―Rate Sensitivity of Mode II Interlaminar Fracture Toughness in Graphite/Epoxy and Graphite/PEEK Composite Materials.", *Composite Science and Technology*, Vol. 29, pp 1-15, 1987.

[61] Blackman, B. R. K., Brunner, A. J., Williams, J. G., ―Mode II fracture testing of composites: a new look at an old problem." *Engineering Fracture Mechanics,* Vol. 73 (2006), pp. 2443-2455.

[62] Lee, S. M., ―Mode II delamination failure mechanisms of polymer matrix composites." *Journal of Materials Science,* Vol. 32 (1997), pp. 1287-1295.

[63] Benyahia, A. A., Laksimi, A., Benmedakhene, S., Gong, X. L., ―Fracture process in ±θ laminates subjected to mode II loading." *Strength of Materials,* Vol. 34, No. 4 (2002), pp. 390-401.

11 DISTRIBUTION

Lawrence Livermore National Laboratory
Attn: N. Dunipace (1)
P.O. Box 808, MS L-795
Livermore, CA 94551-0808

1	MS9106	Timothy M. Briggs	08226
1	MS9106	Douglas L. Gehmlich	08226
1	MS9153	Timothy J. Shepodd	08220
1	MS9404	Neville R. Moody	08651
1	MS0899	Technical Library	9536 (electronic copy)
1	MS0123	D. Chavez, LDRD Office	1011

Sandia National Laboratories